DEVELOPMENT OF HIGH PERFORMANCE COMPOSITE LITHIUM ION BATTERY CATHODE SYSTEMS WITH CARBON NANOTUBES FUNCTIONALISED WITH BIMETALLIC INORGANIC NANOCRYSTAL ALLOYS

By

Chinwe Oluchi Ikpo

A thesis submitted in fulfilment of the requirements for the degree of

Doctor Philosophiae in the Department of Chemistry

Faculty of Science

University of the Western Cape

Supervisors:

Professor Emmanuel I. Iwuoha

Professor Kenneth I. Ozoemena

November 2011

Keywords

Lithium ion diffusion

Quasi-reversible electron transfer process

Coulometric capacity

Standard rate constant

Warburg coefficient

Reductive precipitation

Charge – discharge reversibility

Electrochemical impedance spectroscopy

Cyclic voltammetry

Lithium iron phosphate composite cathode systems

Klingler and Kochi equation

LIR 2032 coin cell

Abstract

Lithium ion cathode systems based on composites of lithium iron phosphate ($LiFePO_4$), iron-cobalt-derivatised carbon nanotubes (FeCo-CNT) and polyaniline (PA) nanomaterials were developed. The FeCo-functionalised CNTs were obtained through *in-situ* reductive precipitation of iron (II) sulfate heptahydrate ($FeSO_4.7H_2O$) and cobalt (II) chloride hexahydrate ($CoCl_2.6H_2O$) within a CNT suspension via sodium borohydride ($NaBH_4$) reduction protocol. Results from High Resolution Transmission Electron Microscopy (HRTEM) and Scanning Electron Microscopy (SEM) showed the successful attachment of FeCo nanoclusters at the ends and walls of the CNTs. The nanoclusters provided viable routes for the facile transfer of electrons during lithium ion deinsertion/insertion in the 3-D nanonetwork formed between the CNTs and adjacent $LiFePO_4$ particles. The voltammetric and impedimetric analyses of the composite cathodes ($LiFePO_4$/10% FeCoCNT-PA and $LiFePO_4$/50% FeCoCNT-PA assembled in lithium ion rechargeable (LIR) 2032 coin cells) gave higher electrochemical performance for the composite prepared with $LiFePO_4$/10%. The performance parameters (for $LiFePO_4$/10% FeCoCNT-PA and $LiFePO_4$/50% FeCoCNT-PA) were: charge capacity (148 and 86 mAh/g), time constant (τ, 6.43×10^{-5} and 2.13×10^{-4} s rad^{-1}), charge transfer resistance (R_{ct}, 24.57 and 115.7 Ω) exchange current (I_0, 1.045×10^{-3} and 2.219×10^{-4} A) rate constant of electron transfer (k_{et}, 2.36×10^{-7} and 5.0×10^{-8} cm s^{-1}), the Warburg coefficient (σ, 38.41 and 63.62 Ω s$^{-1/2}$) and the apparent lithium ion diffusion coefficients (D_{app}, 4.57×10^{-14} and 1.67×10^{-14} cm^2 s^{-1}). Results from charge/discharge studies showed that the high performance $LiFePO_4$/10% FeCoCNT-PA composite cathode gave higher Coulombic efficiency (90%), higher retention capacity (99.72%) and lower capacity loss (10%) compared to pristine $LiFePO_4$ which had values of 80.36%, 89.61% and 19.64% for Coulombic efficiency, retention capacity and capacity loss, respectively.

Declaration

I declare that *Development of high performance composite lithium ion battery cathode systems with carbon nanotubes functionalised with bimetallic inorganic nanocrystal alloys* is my own work, that it has not been submitted for any degree or examination in any other university, and that all sources I have used or quoted have been indicated and acknowledged by means of complete references.

Chinwe Oluchi Ikpo   November, 2011.

Signature…………………………

Acknowledgements

Dedication

This thesis is dedicated to Professor Kehinde O. Okonjo and to the memory of my father Mr

Julius Chukwudozie Ikpo who went to be with the Lord just before I was born.

Contents

List of figures

List of tables

List of schemes

List of abbreviations

$LiFePO_4$	Lithium iron phosphate
FeCo	Iron-cobalt
CNTs	Carbon nanotubes
PA	Polyaniline
CV	Cyclic voltammetry
EIS	Electrochemical impedance spectroscopy
D_{app}	Apparent diffusion coefficient
K_{et}	Rate constant of electron transfer
I_o	Exchange current
R_{ct}	Charge transfer resistance
τ	Time constant
HRTEM	High resolution transmission electron microscopy
SEM	Scanning electron microscopy
EVs	Electric vehicles
ICE	Internal combustion engine
HEVs	Hybrid electric vehicles
PEs	Polymer electrolytes
SPEs	Solid polymer electrolytes
GPEs	Gel polymer electrolytes

<center>**Chapter 1**</center>

<center>**Introduction**</center>

1.1 Sustainable energy and the urgent need for efficient electrochemical storage systems

Sustainable energy, as defined from the concepts of sustainable development[1], is the provision of energy that meets the needs of the present without compromising the ability of future generations to meet their own needs (Figure 1). The present energy supply and use, mostly based on non-renewable and limited resources of fossil fuels (coal, oil and natural gas), is deemed to be environmentally unsustainable [2]. This is due to the fact that the combustion of fossil fuels to produce electricity releases carbon dioxide (CO_2) which is the major greenhouse gas contributing to global warming and climate change. As the world's population grows towards nine billion people over the next fifty years[3], the global energy demand is anticipated to increase proportionately. This projection in energy consumption, coupled with the growing demand for low or zero-emission sources of energy, has brought increasing awareness of the need for clean and renewable energy sources. The two principal renewable energy sources are solar and windmills. Solar and wind power systems convert natural sources of energy (sunlight and wind kinetic energy) into electricity. They are regarded as major future sources of electrical energy. However, intermittent supply of energy from these renewable sources as a result of seasonal and tidal variations makes the development of efficient energy storage systems inevitable. The transport sector is not left out of the energy crisis. Currently, the internal combustion engine (ICE), which dominates as a power source for most automobile systems, is a major user of fossil fuels and consumes about 1/3 of the annual total demand for energy[4]. As the world's population grows, there will be need for more automobiles. It is estimated that there will be 1.5 billion vehicles in the year

2020 and the total emission of CO_2 from transportation will be about 65% higher [5]. In view of the above environmental concerns, a sustainable mitigation measure involves the replacement of ICE powered vehicles with zero-emission vehicles, that is, electric vehicles (EVs) or at least with controlled emission vehicles, that is hybrid electric vehicles (HEVs). A recent study revealed that petroleum consumption in the United States will shrink by six million barrels per day if half the vehicles on the road in 2030 are electric powered [6]. Again, the successful achievement of this objective lies in the development of suitable storage systems.
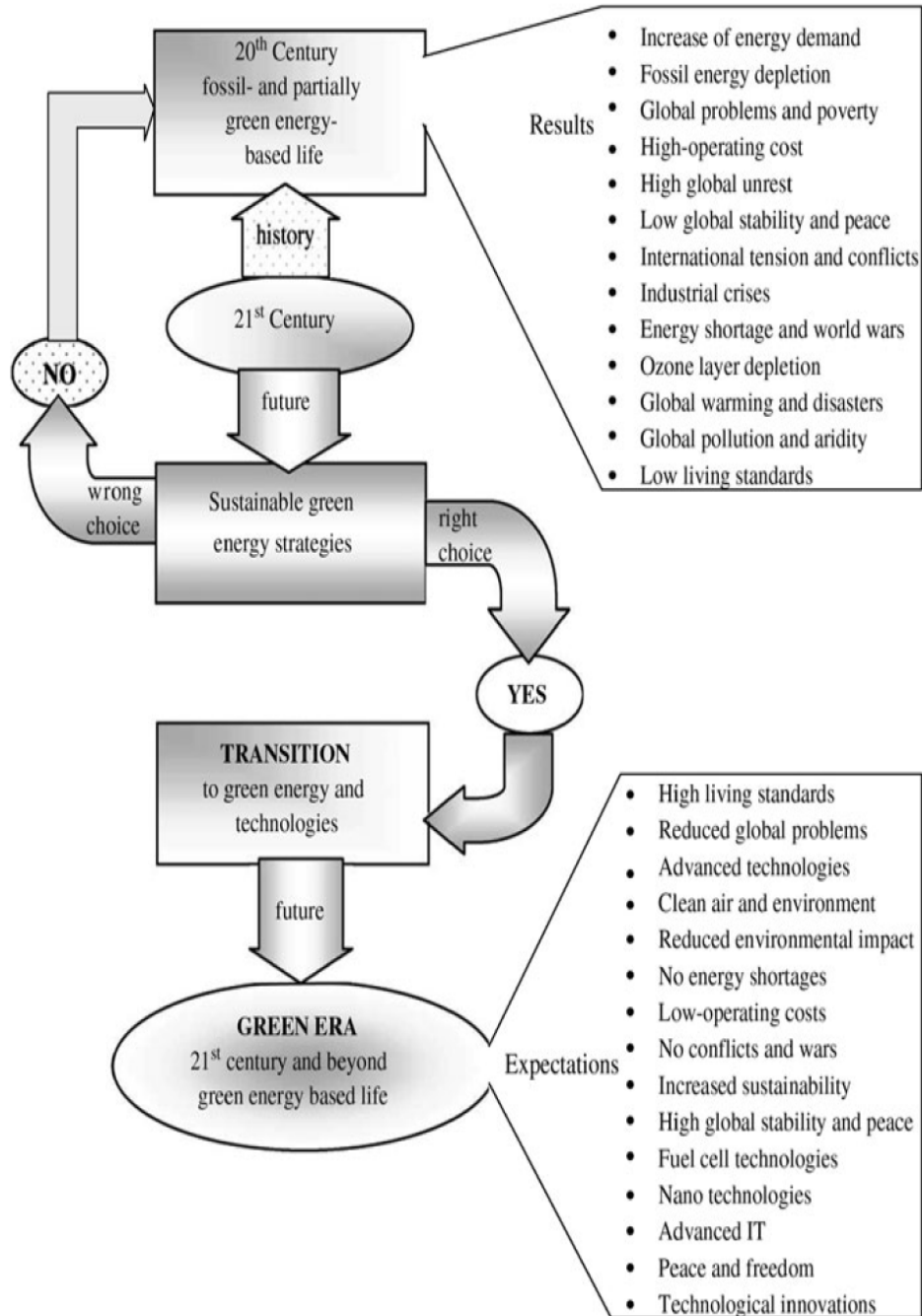
Figure 1: Key expectations from implementation of green energy strategies and policies [7].

The development of reliable storage technologies is also important for the myriads of portable electronic devices such as mobile phones, digital cameras and high performance computing systems that are constantly released to the consumer world, since limited amount

of electrical energy can be stored in magnetic fields (superconductive coils) or electric fields (capacitors). Electrical energy storage unarguably, is the key technology for an efficient and sustainable use of energy. The storage of electrical energy requires its conversion into another form of energy [8]. The most versatile and convenient way is conversion to chemical energy through the use of rechargeable batteries [9-10]. Batteries are electrochemical devices that convert chemical energy into electrical energy and vice versa, via redox reactions which occur at the electrodes [11]. A Battery has more energy density than a supercapacitor [12], another electrochemical energy storage device. Since the invention of the first battery in 1800 by Alessandro Volta, battery technology has been undergoing series of revolutions as shown in Table 1.

Table 1: History of electrochemical cell development [6].

Type	Year	Inventor	Battery
Primary batteries	1800	Alessandro Volta	Voltaic pile
	1836	John Frederic Daniel	Daniel cell
	1844	William Robert Grove	Grove cell
	1860	Callaud	Gravity cell
	1866	Georges-Lionel Leclanché	Leclanché wet cell
	1888	Carl Gassner	Zinc–carbon dry cell
	1955	Lewis Urry	Alkaline battery
	1970	No information	Zinc-air battery
	1975	Sanyo Electric Co	Lithium–manganese cell
	2004	Panasonic Corporation	Oxyride battery
Secondary batteries	1859	Raymond Gaston Planté	Planté lead-acid cell
	1881	Camille Alphonse Faure	Improved lead-acid cell
	1899	Waldmar Jungner	Nickel–cadmium cell
	1899	Waldmar Jungner	Nickel–iron cell
	1946	Union Carbide Company	Alkaline manganese secondary cell
	1970	Exxon laboratory	Lithium–titanium disulfide
	1980	Moli Energy	Lithium–molybdenum disulfide
	1990	Samsung	Nickel–metal hydride
	1991	Sony	Lithium-ion
	1999	Sony	Lithium polymer

Table 2: Some typical properties of secondary batteries [6].

System	Nominal cell voltage (V)	Specific energy (Wh/kg)	Cycle life (up to 80% initial capacity)	Charge time (h)	Self-discharge per month (%)
Lead–acid	2	30–50	200–350	8–16	5
Ni–Cd	1.25	45–80	1500	1	20
Ni–MH	1.25	60–120	300–500	2–4	30
Li ion	3.6	110–180	500–1000	2–4	10
Li polymer	3.6	100–130	300–500	2–4	10

The lithium ion battery with its outstanding features as shown in Table 2 and Figure 2 is designed to spearhead the modern revolution in batteries.
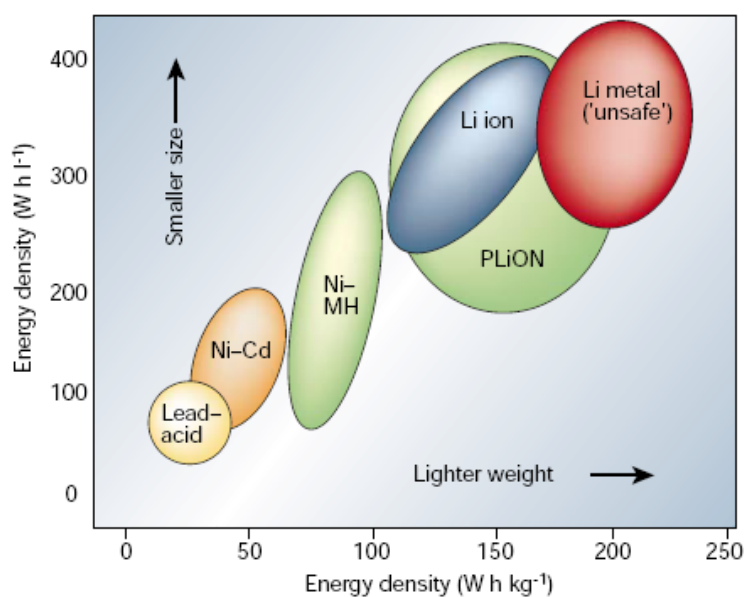
Figure 2: Comparison of the different battery technologies in terms of volumetric and gravimetric energy density [13].

Worldwide battery demand is projected to rise at a 4.8% annual rate to $109 billion (USD) in 2014 [14]. In order to effectively meet the increasing market demands which are in tandem with technological advancements, there is need for further improvements in battery technology. This will mostly depend on the development of new materials as well as

enhancement of the properties of the existing ones, for the various battery components [15-18]. The global anticipation of a green and sustainable energy use can therefore be realized through the development of improved battery technology in general and lithium ion technology in particular. In fact, it is impossible to think of a world without batteries [19].

The remainder of this chapter provides a general introduction to batteries with emphasis on lithium ion battery technology as well as the electrochemical techniques studied in this thesis. The chapter concludes with the rationale, aim and objectives of the research.

1.2 Elementary battery concepts

The basic unit in a battery is the electrochemical cell which consists of three main components; the electrodes: cathode and anode; and the electrolyte. The cathode is characterised as the electrode where a reduction-reaction occurs (*i.e.* electrons are accepted from an outer circuit); while an oxidation-reaction occurs at the anode (*i.e.* electrons are donated to an outer circuit). The voltage and capacity of a cell are functions of the electrode materials used. The anode material should be efficient as a reducing agent, have high Coulombic output, good conductivity, stability, ease of fabrication and low cost. Practically, metals are mainly used as the anode material. The cathode must be an efficient oxidizing agent, have a useful working voltage and show good stability when in contact with the electrolyte. As reactions at the anode usually take place at lower electrode potentials than at the cathode, the terms negative and positive electrode (indicated as minus and plus poles) are used. The more negative electrode is designated the anode, whereas the cathode is the more positive one. The electrolyte, a solution of a salt and a solvent, is an electronic insulator, but a good ionic conductor. Its main function is to provide a transport-medium for ions to travel from one electrode to the other. It must also prevent short-circuiting by acting as a physical

barrier between the electrodes. Conceptually, the electrolyte should undergo no net chemical changes during the operation of the battery, and all Faradaic processes are expected to occur within the electrodes [20]. Most electrolytes are aqueous solutions except in thermal and lithium anode batteries. A typical electrode reaction in a lead acid battery is as shown below:

$$\text{Anode: } Pb + H_2SO_4 \rightarrow PbSO_4 + 2H^+ + 2e^- \tag{1}$$

$$\text{Cathode: } PbO_2 + H_2SO_4 + 2H^+ + 2e^- \rightarrow PbSO_4 + 2H_2O \tag{2}$$

$$\text{Overall Cell reaction: } Pb + PbO_2 + 2H_2SO_4 \rightarrow 2PbSO_4 + 2H_2O \tag{3}$$
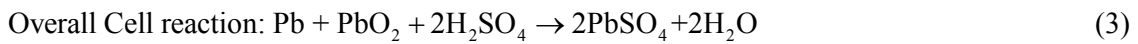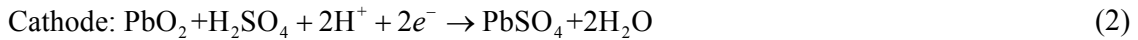
The energy storage and power characteristics of battery systems follow directly from the thermodynamic and kinetic formulations for chemical reactions as adapted to electrochemical reactions. The basic thermodynamic equations for a reversible electrochemical transformation are given as:

$$\Delta G = \Delta H - T\Delta S \tag{4}$$

$$\Delta G^* = \Delta H^* - T\Delta S^* \tag{5}$$

where ΔG is the change in Gibbs free energy which is the net energy of a reaction available for useful work; ΔH is the enthalpy change or the energy released by the reaction; ΔS is the change in entropy; T is the absolute temperature; $T\Delta S$ is the heat associated with the organization/ disorganization of materials. ΔG^*, ΔH^* and ΔS^* represent changes in Gibbs free energy, enthalpy and entropy, respectively for the material in the standard state at 25 °C and unit activity. The change in the standard free energy of a cell reaction is the driving force which enables a battery to deliver electrical energy to an external circuit. Consider the total cell reaction:

$$Li_xFePO_4 + Li_yC_6 \rightarrow Li_{x+\delta}FePO_4 + Li_{y-\delta}C_6 \tag{6}$$

The thermodynamic quantity describing the change in energy as a function of changes in Li concentration in the host matrix is the chemical potential (μ), defined as:

$$\mu = \frac{\partial G}{\partial x} \qquad (7)$$

-where x is the number of inserted Li atoms. The change in free energy can be expressed as:

$$\Delta G = -nFE \qquad (8)$$

-where n is the number of electrons in both electrode reactions (δ in the cell reaction above), F is the Faraday constant, E is the potential difference between the electrodes. Whenever a reaction occurs, there is a change in the free energy of the system as expressed in Equation (8). The relation between electrical and chemical energy in the system is obtained by combining (7) and (8):

$$-\partial FE = \mu_c - \mu_a \qquad (9)$$

-where μ_c and μ_a are the chemical potentials of the lithium ions in the cathode and anode respectively. The mechanism of battery electrode reactions often involves a series of physical, chemical, and electrochemical steps, including charge-transfer and charge transport reactions. The rates of these individual steps determine the kinetics of the electrode and, thus, of the cell/battery. The primary goal of battery development is to maximize the following characteristics while maintaining safety and reasonable cost:

- specific energy (Wh/kg): energy stored per unit mass

- energy density (Wh/L): energy stored per unit volume

- specific power (W/kg): power available per unit mass

- power density (W/L): power available per unit volume

- high reversibility of charge and discharge (for rechargeable batteries)

The amount of electrical energy expressed per unit of weight or per unit of volume that a battery can deliver is a function of the cell potential (which depends on the type of active

materials used) and the capacity (which depends on the amount of active materials used), both of which are linked directly to the basic chemistry of the system. Battery power depends mainly on the chemicals the battery contains and partly on the engineering design [15]. Maximizing the stored energy content of a battery requires maximising the chemical potential difference between the electrodes; and by controlling the specific charge that can be accommodated in the electrodes. The choice of electrode materials is constrained by the fact that electrodes must conduct both electrons and ions. In practice, only a fraction of the theoretical energy of the battery is realized. This is due to the need for electrolyte and nonreactive components (containers, separators, electrodes) that add to the weight and volume of the battery, as illustrated in Figure 3. Another contributing factor is that the battery does not discharge at the theoretical voltage (thus lowering the average voltage), nor is it discharged completely to zero volts (thus reducing the delivered ampere-hours capacity). Further, the active materials in a practical battery are usually not stoichiometrically balanced. This reduces the specific energy because an excess amount of one of the active materials is used [11].
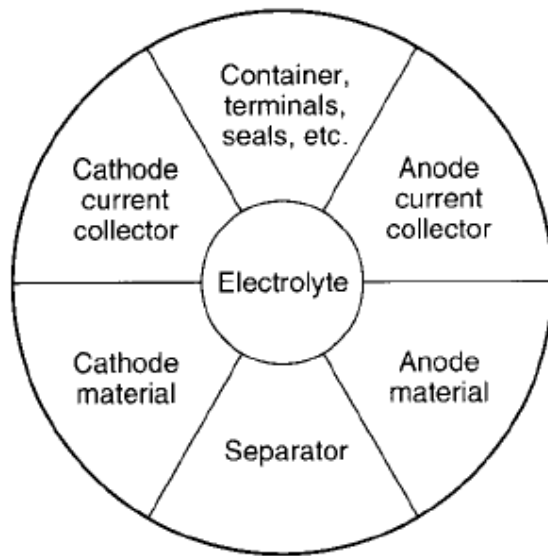
Figure 3: Components of a cell [11].

1.2.1 Polarisation effects and Ohmic drop

The maximum electric energy that can be delivered by the chemicals that are stored within or supplied to the electrodes in the cell depends on the change in free energy ΔG of the electrochemical couple, as shown in Equation (8). It would be desirable if during the discharge, all of this energy could be converted to useful electric energy. However, losses due to polarization occur when a load current, I, passes through the electrodes, accompanying the electrochemical reactions. These losses include: (a) activation polarization, which drives the electrochemical reaction at the electrode surface, and (b) concentration polarization, which arises from the concentration differences of the reactants and products at the electrode surface and in the bulk as a result of mass transfer. These polarization effects consume part of the energy, which is given off as waste heat, and thus not all of the theoretically available energy stored in electrodes is fully converted into useful electrical energy. In practice, it is difficult to determine the values for activation polarisation and concentration polarisation because of the complicated physical structure of the electrodes. Most battery electrodes are made of composite active material, binder, performance enhancing additives and conductive filler. They usually have a porous structure of finite thickness and require complex mathematical modelling with computer calculations to estimate the polarization components.

Another factor that strongly affects the performance or rate capability of a cell is the internal impedance of the cell. It causes a voltage drop during operation, which also consumes part of the useful energy as waste heat. The voltage drop due to internal impedance is usually referred to as ''Ohmic polarization'' or IR drop and is proportional to the current drawn from the system. The total internal impedance of a cell is the sum of the ionic resistance of the electrolyte (within the separator and the porous electrodes); the electronic resistances of the active mass, the current collectors and electrical tabs of both electrodes; and the contact

resistance between the active mass and the current collector. These resistances are Ohmic in nature, and follow Ohm's law, with a linear relationship between current and voltage drop. When connected to an external load R, the cell voltage E can be expressed as:

$$E = E_0 - \left[\left(\eta_{ct} \right)_a + \left(\eta_c \right)_a \right] - \left[\left(\eta_{ct} \right)_c + \left(\eta_c \right)_c \right] - IR_i = IR \tag{10}$$

-where E_0 = electromotive force or open circuit voltage of a cell

$(\eta_{ct})_a$, $(\eta_{ct})_c$ = activation polarization or charge-transfer overvoltage at anode and cathode

$(\eta_c)_a$, $(\eta_c)_c$ = concentration polarization at anode and cathode

   I = operating current of cell on load

   R_i = internal resistance of cell

As shown in Equation (10), the useful voltage delivered by the cell is reduced by polarization and the internal IR drop. It is only at very low operating currents, where polarization and the IR drop are small, that the cell may operate close to the open-circuit voltage and deliver most of the theoretically available energy. Figure 4 shows the relation between cell polarization and discharge current.
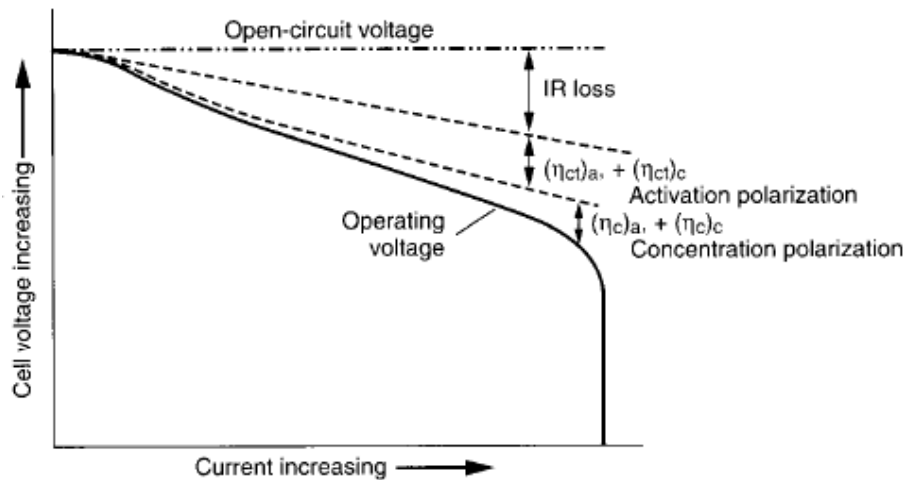
Figure 4: Cell polarization as a function of operating current [11].

1.2.2 Factors affecting the magnitude of charge-transfer reaction

It has been stated earlier that the available energy of a battery depends on the basic electrochemical reactions at both electrodes. However, there are many factors which affect the magnitude of the charge-transfer reaction, diffusion rates, and magnitude of the energy loss some of which factors include:

- electrode formulation and design;

- electrolyte conductivity;

- nature of the separators.

Based on the electrochemical principles, there are some essential rules, which are important in the design of batteries in order to achieve a high operating efficiency with minimal loss of energy:

(1) The conductivity of the electrolyte should be high enough that the *IR* polarization is not excessively large for practical operation. Batteries are usually designed for specific drain rate applications, ranging from microamperes to several hundred amperes. For a given electrolyte, a cell may be designed to have improved rate capability, with a higher electrode interfacial area and thin separator, to reduce the *IR* drop due to electrolyte resistance.

(2) Electrolyte salt and solvents should have chemical stability to avoid direct chemical reaction with the anode or cathode materials.

(3) The rate of electrode reaction at both the anode and the cathode should be sufficiently fast so that the activation or charge-transfer polarization is not too high to make the cell inoperable. A common method of minimizing the charge-transfer polarization is to use a porous electrode design. The porous electrode structure provides a high electrode surface area within a given geometric dimension of the electrode and reduces the local current density for a given total operating current.

(4) To avoid build-up of excessive concentration polarization, the cell should have adequate electrolyte transport to facilitate the mass transfer of the reaction products. Proper porosity and pore size of the electrode, adequate thickness and structure of the separator, and sufficient concentration of the reactants in the electrolyte are very important. Mass-transfer limitations should be avoided for normal operation of the cell.

(5) The material of the current collector or substrate should be compatible with the electrode material and the electrolyte without causing corrosion problems. The design of the current collector should provide a uniform current distribution and low contact resistance to minimize electrode polarization during operation.

(6) For rechargeable cells, the reaction products should be mechanically and chemically stable with the electrolyte to facilitate the reversible reactions during charge and discharge.

1.2.3 Factors affecting battery performance

Many factors influence the operational characteristics, capacity, energy output and performance of a battery. Some of these factors are discussed below:

Voltage level

Different references are made to the voltage of a cell or battery:

(a) The theoretical voltage is a function of the anode and cathode materials, the composition of the electrolyte and the temperature (usually stated at 25 ºC).

(b) The open-circuit voltage is the voltage under a no-load condition and is usually a close approximation of the theoretical voltage.

(c) The closed-circuit voltage is the voltage under a load condition.

(d) The nominal voltage is one that is generally accepted as typical of the operating voltage of the battery, for example, 1.5 V for a zinc-manganese dioxide battery.

(e) The working voltage is more representative of the actual operating voltage of the battery under load and will be lower than the open-circuit voltage.

(f) The average voltage is the voltage averaged during the discharge.

(g) The midpoint voltage is the central voltage during the discharge of the cell or battery.

(h) The end or cut-off voltage is designated as the end of the discharge. Usually it is the voltage above which most of the capacity of the cell or battery has been delivered. The end voltage may also be dependent on the application requirements.

Using the lead-acid battery as an example, the theoretical and open-circuit voltages are 2.1 V, the nominal voltage is 2.0 V, the working voltage is between 1.8 and 2.0 V, and the end voltage is typically 1.75 V on moderate and low-drain discharges; and 1.5 V for engine cranking loads. On charge, the voltage may range from 2.3 to 2.8 V.

When a cell or battery is discharged, its voltage is lower than the theoretical voltage. The difference is caused by IR losses due to cell (and battery) resistance and polarization of the active materials during discharge as shown in Figure 5. In the ideal situations, the discharge of the battery proceeds at the theoretical voltage until the active materials are consumed and the capacity is fully utilized. The voltage then drops to zero. Under actual conditions, the

discharge curve is similar to the other curves in Figure 5. The initial voltage of the cell under a discharge load is lower than the theoretical value due to the internal cell resistance and the resultant IR drop as well as polarization effects at both electrodes. The voltage also drops during discharge as the cell resistance increases due to the accumulation of discharge products, activation and concentration, polarization, and related factors. Curve 2 is similar to curve 1, but represents a cell with a higher internal resistance or a higher discharge rate, or both, compared to the cell represented by curve 1. As the cell resistance or the discharge current is increased, the discharge voltage decreases and the discharge shows a more sloping profile.
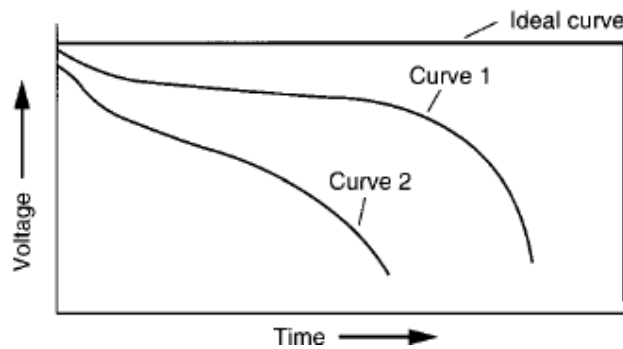
Figure 5: Characteristic discharge curves[11].

The specific energy that is delivered by a battery in practice is therefore lower than the theoretical specific energy of its active materials, due to: (1) the average voltage during the discharge is lower than the theoretical voltage. (2) The battery is not discharged to zero volts and all of the available ampere-hour capacity is not utilized.

Since specific energy is given by:

$$Watt\ hours\,/\,gram\ =\ Voltage\ x\ Ampere\ hours\,/\,gram \qquad (11)$$

The delivered specific energy is lower than the theoretical energy as both of the components of the Equation (11) are lower.

The shape of the discharge curve can vary depending on the electrochemical system, constructional features, and other discharge conditions. Typical discharge curves are shown in Figure 6. The flat discharge (curve 1) is representative of a discharge where the effect of change in reactants and reaction products is minimal until the active materials are nearly exhausted. The plateau profile (curve 2) is representative of two-step discharge indicating a change in the reaction mechanism and potential of the active material(s). The sloping discharge (curve 3) is typical when the composition of the active materials, reactants, internal resistance, and so on, changes during the discharge, affecting the shape of the discharge curve similarly.
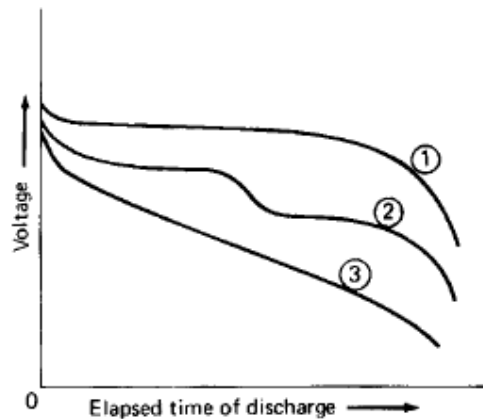
Figure 6: Battery discharge characteristics—voltage profiles [11].

Current drain of discharge

As the current drain of the battery is increased, the IR losses and polarization effects increase; the discharge is at a lower voltage, and the service life of the battery is reduced. Figure 7(a)

shows typical discharge curves as the current drain is changed. At extremely low current drains (curve 2) the discharge can approach the theoretical voltage and theoretical capacity.

However, with very long discharge periods, chemical deterioration during the discharge can become a factor and cause a reduction in capacity. With increasing current drain (curves 3–5), the discharge voltage decreases, the slope of the discharge curve becomes more pronounced, and the service life, as well as the delivered ampere-hour or Coulombic capacity, are reduced.

(a)   (b)
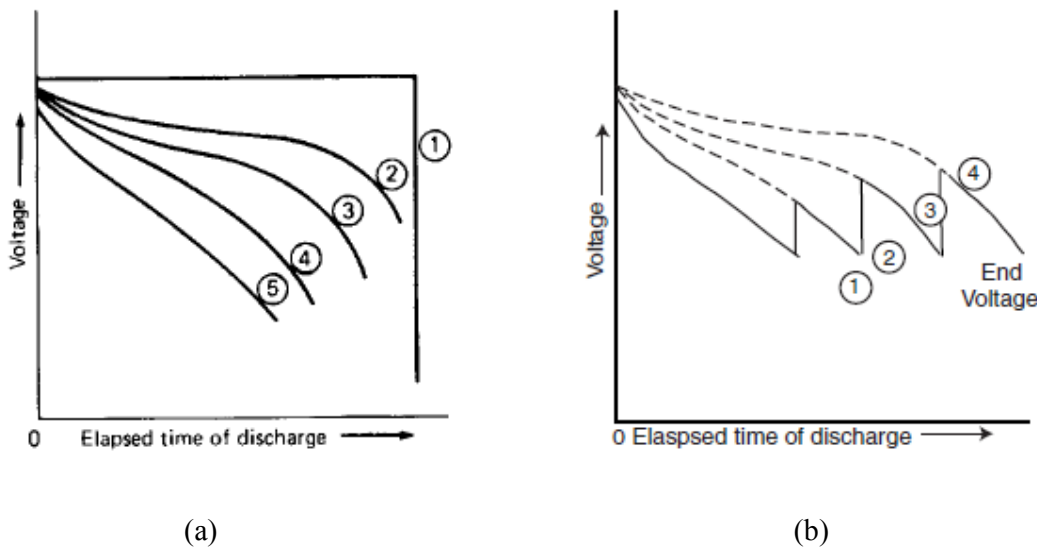
Figure 7: (a) Battery discharge characteristics—voltage levels. (b) Discharge characteristics of a battery discharged sequentially from high to lower discharge rates [11].

If a battery that has reached a particular voltage (such as the cut-off voltage) under a given discharge current is used at a lower discharge rate, its voltage will rise and additional capacity or service life can be obtained until the cut-off voltage is reached at the lighter load. Thus, for example, a battery that has been used to its end-of-life in a flash camera (a high drain application) can subsequently be used successfully in a quartz clock application which

operates at a much lower discharge rate. This procedure can also be used for determining the life of a battery under different discharge loads using a single test battery. As shown in Figure 7(b), the discharge is first run at the highest discharge rate to the specified end voltage. The discharge rate is then reduced to the next lower rate. The voltage increases and the discharge is continued again to the specified end voltage, and so on. The service life can be determined for each discharge rate, but the complete discharge curve for the lower discharge rates, as shown by the dashed portion of each curve, obviously is lost. In some instances a time interval is allowed between each discharge for the battery to equilibrate prior to discharge at the progressively lower rates.

1.2.4 Capacity and battery C-rates

The capacity of a cell/battery is the amount of charge available which is expressed in ampere-hour (Ah). An ampere is the unit of measurement used for electric current and is defined as a coulomb of charge passing through an electrical conductor in one second. The capacity of a cell or battery is related to the quantity of active materials in it and the amount of electrolyte and the surface area of the plates. The capacity of a battery is measured by discharging at a constant current until it reaches its terminal voltage. This is usually done at a constant temperature, under standard conditions (25°C). The capacity is calculated by multiplying the discharge current value by the time required to reach terminal voltage. The most common term used to describe a battery's current is its rated capacity. The charge and discharge current of a battery is measured in C-rate. Manufacturers frequently specify the rated capacity of their batteries in ampere-hour at a specific discharge rate. For example, a battery rated for 200 Ah (for a 10-hour rate) will deliver 20 amperes of current for 10 hours under standard conditions. Alternatively, a discharge rate may be specified by its charge rate or C-rate which

is expressed as multiple of the rated capacity of the cell or battery. A battery may have a rating of 200 Ah at a C/10 discharge rate. The discharge rate is determined by the equation below:

$$C/10 \; rate \; (amperes) \; = \; 200 \; Ah/10 \; h \; = \; 20 \; A \tag{12}$$

A discharge of 1 C draws a current equal to the rated capacity. For example, a battery rated at 1000 mAh provides 1000 mA for one hour if discharged at 1 C rate. The same battery discharged at 0.5 C, provides 500 mA for two hours. The same battery delivers 2000 mA for thirty minutes. 1C is often referred to as a one-hour discharge. A 0.5 C (C/2) would be a two-hour discharge and a 0.1 C (C/10) a 10-hour discharge. Battery capacity varies with the discharge rate. The higher the discharge rate, the lower the cell capacity. Lower discharge rates result in higher capacity.

1.3 Classification of batteries

Batteries are classified as primary or secondary depending on their capability of being electrically recharged.

1.3.1 Primary batteries

In primary batteries, the electrode reactions are not reversible and the cells are therefore not rechargeable, *i.e.* they are discharged once and discarded. *Discharge* is an operation in which a battery delivers electrical energy to an external load whereas *charge* involves the restoration of a battery to its original charged condition by reversal of the current flow. Primary batteries have high energy density, good storage characteristics and are usually inexpensive source of power for portable electronic and electric devices. Some examples of primary batteries are zinc-alkaline-manganese-dioxide (the Leclanche´ cell), zinc-mercuric-

oxide, zinc-silver oxide, zinc-air, magnesium-manganese-dioxide and primary lithium batteries. Zinc has been by far the most popular anode material for primary batteries because of its good electrochemical behaviour and compatibility with aqueous electrolytes but the lithium anode battery systems, offer the opportunity for higher energy density and other advances in the performance characteristics of primary systems. Lithium primary batteries use lithium metal as the anode. Lithium metal is attractive because of its light weight, high voltage, good conductivity and high electrochemical equivalence. Non-aqueous solvents are used as electrolytes in lithium batteries because of the reactivity of lithium in aqueous solutions. There are many kinds of primary lithium batteries based on the electrolyte and cathode material used. Examples are: lithium-sulphur dioxide (Li/SO_2), lithium-thionyl chloride ($Li/SOCl_2$), lithium-sulfuryl chloride (Li/SO_2Cl_2), lithium-manganese dioxide (Li/MnO_2) and lithium/carbon monofluoride $Li/ (CF)_n$ [11, 20-23].

1.3.2 Secondary (rechargeable) batteries

The electrode reactions in secondary batteries are reversible and the cells are rechargeable. Rechargeable batteries are used in automotive and aircraft systems, emergency no-fail and standby (UPS) power sources, hybrid electric vehicles and stationary energy storage (SES) systems for electric utility load levelling. They also find applications in portable consumer electronics, power tools, and electric vehicles. Conventional aqueous secondary batteries are characterized, in addition to their ability to be recharged, by high power density, flat discharge profiles, and good low-temperature performance. Their energy densities however, are usually lower, and their charge retention is poorer than those of primary battery systems. Lithium ion technologies, however, have higher energy densities, better charge retention, and other performance enhancements characterized by the use of higher energy materials [8, 11, 24]. In a rechargeable battery, the anode is the negative electrode during discharge while the

cathode is the positive electrode. On charging however, the anode becomes the positive electrode while the cathode is the negative electrode. The secondary batteries include the lead-acid, nickel-cadmium, nickel-metal hydride, lithium ion, nickel-iron, nickel-zinc, secondary silver-zinc, silver-cadmium, nickel-hydrogen, silver - hydrogen and lithium-metal batteries. Energy storage in a typical secondary battery involves Faradaic reactions occurring at the surface of an electrode, and mass and charge transfer through the electrode. Therefore, the surface area and the transport distance play important roles in determining the performance of the battery in question. Chemical composition and structure will have significant impacts on the surface reaction and transfer processes as well as on cyclic stability.

1.4 The role and challenges of lithium metal in batteries

Interest in this alkali metal as a promising anode material arose from the combination of its two unique properties: (a) it is a strong reducing agent with a very low standard reduction potential (a measure of the ease with which an ion is reduced back to the metallic state) of - 3.04 V which translates into high cell voltage when matched with cathodes that are capable of reversible lithium insertion, for example, MnO_2, MoS_2 or TiS_2 [21, 25]; and (b) it is the lightest metal with a density of 0.53 g cm^{-3} which makes it an anode of high specific capacity (3860 $mAhg^{-1}$). The electrochemical capacity of a metal is a practical property defined as the quantity of electric charge produced per gram of metal in the anode half reaction [26]. Because of these outstanding electrochemical features, the search for high-energy density batteries led to the use of lithium in primary and secondary batteries. Secondary lithium-metal batteries which have a lithium metal anode are attractive because of their high energy density. Lithium-molybdenum disulfide batteries were the world's first secondary cylindrical lithium-metal batteries. The continued efforts to expand lithium chemistry into rechargeable

technology, however, encountered severe difficulties in terms of the cycle life and safety. The reactivity of the lithium metal anode with the electrolyte and changes that occur after repetitive charge-discharge cycling leads to dendrite formation on the lithium electrode. These dendritic deposits pose risks of explosion as they are chemically hyper-reactive due to their high surface area. In 1989, incidents of fire as a result of overheating defects in the above secondary cylindrical lithium-molybdenum disulfide batteries in electronic devices, followed by the manufacturer's recalls highlighted the end of general enthusiasm in lithium metal as an anode [20-21, 23]. Lithium alloys with other metals such as aluminium, tin and silicon were studied to replace lithium metal [13, 17, 27-29] but the problem of large anode volume change was not solved until the introduction of the concept of lithium ion cells.

1.5 The Lithium ion battery

The failure of metallic lithium as an anode led to the development of rechargeable lithium ion batteries which comprise cells that employ intercalation compounds. Intercalation electrodes in batteries are electroactive materials that serve as hosts into which guest species are reversibly inserted through the electrolyte [30]. These batteries offer improved cycle life and safety than lithium-metal batteries. Lithium ion battery is light, compact and works with an average voltage of 3.8 V with a specific energy that ranges between 100 $Whkg^{-1}$ and 180 $Whkg^{-1}$ which is a factor of five higher than that stored by the much older lead acid batteries [15, 18]. The operation of lithium ion batteries is based on the intercalation process, a topotactic reaction where lithium ion is reversibly removed or inserted between anode and cathode via transport across the electrolyte whereas the electrons generated from the reaction: $Li \rightarrow Li^+ + e^-$, go through the external circuit to do work. The electrode system therefore, must allow for the flow of both lithium ions and electrons [31]. The principal

concept of lithium-ion batteries is illustrated in Figure 8. On discharge, lithium ions are de-intercalated from the negative electrode, through the electrolyte and intercalated into the positive electrode. An exact reverse reaction occurs during the charge process. Hence, lithium ions shuttle back and forth between the electrodes during the discharge-charge cycle. This electrochemical insertion/extraction process is a solid state redox reaction involving electrochemical charge transfer coupled with insertion/extraction of mobile guest ions into/from the structure of an electronic and ionic conductive solid host. The major structural features of the host are kept after the insertion/extraction of the guest. The rate determining step of the intercalation/de-intercalation process is the diffusion of lithium ion in and out of the electrode structures [18-19, 32] while the free energy change of the lithium migration process is the maximum reversible work that can be obtained.
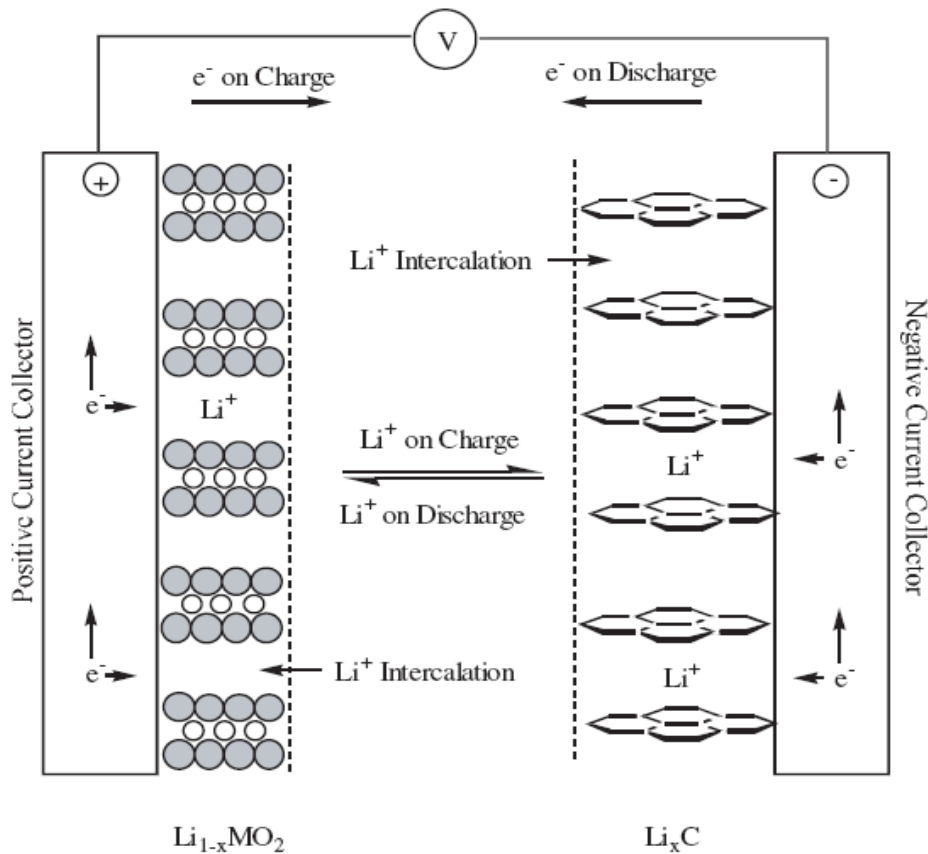
Figure 8: Schematic of the electrochemical process in a lithium ion cell [11].

The reactions at both electrodes in a typical lithium ion cell are as shown:

Positive: $\quad\quad\quad$ $LiMO_2 \underset{\text{discharge}}{\overset{\text{charge}}{\rightleftharpoons}} Li_{1-x}MO_2 + xLi^+ + xe^-$ $\quad\quad\quad\quad\quad\quad\quad$ (13)

Negative: $\quad$ $C + xLi^+ + xe^- \underset{\text{discharge}}{\overset{\text{charge}}{\rightleftharpoons}} Li_xC$ $\quad\quad\quad\quad\quad\quad\quad\quad\quad\quad$ (14)

Overall: $\quad\quad\quad$ $LiMO_2 + C \underset{\text{discharge}}{\overset{\text{charge}}{\rightleftharpoons}} Li_xC + Li_{1-x}MO_2$ $\quad\quad\quad\quad\quad\quad\quad$ (15)
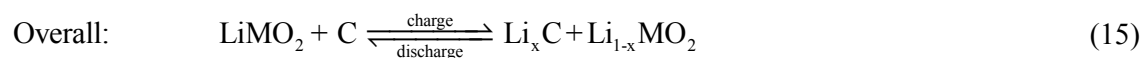
$LiMO_2$ represents lithiated transition metal oxide.

1.5.1 Electrolyte

The basic features of a battery performance (operating voltage, theoretical energy density etc.,) are essentially determined by the chemistry of the active materials used as the positive and negative electrodes. However, the chemistry of the electrolyte often affects battery performance significantly. A suitable electrolyte should have characteristics such as: (I) high ionic conductivity while being electronically insulating so that ion transport can be facile and self-discharge can be kept to a minimum. (II) Wide electrochemical window so that electrolyte degradation would not occur within the range of the working potentials of both the cathode and the anode. (III) Inert to other cell components such as cell separators, electrode substrates, and cell packaging materials. (IV) Thermal and chemical stability. (V) Environmentally friendly. Most compositions of electrolytes in current lithium ion cells are based on solutions of lithium salts in mixtures of two or more solvents. A mixed solvent formulation can provide better cell performance, higher conductivity, and a broader temperature range than a single solvent electrolyte; however, mixtures of salts are usually not used [20]. An ideal electrolyte solvent should meet the following requirements: (a) it should be able to dissolve salts to sufficient concentration. In other words, it should have a high dielectric constant (ε). (b) It should be fluid (low viscosity η), so that facile ion transport can

occur. (c) It should remain inert to all cell components, especially the charged surfaces of the cathode and the anode, during cell operation. (d) It should remain liquid in a wide temperature range. In other words, its melting point (T_m) should be low and its boiling point (T_b) high. (e) It should also be safe (high flash point T_f), nontoxic, and economical. The most commonly used solvents for electrolytes in lithium ion batteries are nonaqueous aprotic organic compounds including cyclic and acyclic carbonates, esters and ethers. Some of the major electrolyte solvents together with their physical properties are shown in Tables 3 and 4.

Table 3: Organic Carbonates and Esters as Electrolyte Solvents [20].

Solvent	Structure	M. Wt	T_m/ °C	T_b/ °C	η/cP 25 °C	ε 25 °C	Dipole Moment/debye	T_f/ °C	d/gcm^{-3}, 25 °C
EC		88	36.4	248	1.90, (40 °C)	89.78	4.61	160	1.321
PC		102	-48.8	242	2.53	64.92	4.81	132	1.200
BC		116	-53	240	3.2	53			
γBL		86	-43.5	204	1.73	39	4.23	97	1.199
γVL		100	-31	208	2.0	34	4.29	81	1.057
NMO		101	15	270	2.5	78	4.52	110	1.17
DMC		90	4.6	91	0.59 (20 °C)	3.107	0.76	18	1.063
DEC		118	-74.3 [a]	126	0.75	2.805	0.96	31	0.969
EMC		104	-53	110	0.65	2.958	0.89		1.006
EA		88	-84	77	0.45	6.02		-3	0.902
MB		102	-84	102	0.6			11	0.898
EB		116	-93	120	0.71			19	0.878

EC = ethylene carbonate; PC = propylene carbonate; BC = butylene carbonate; BL = butyro-lactone; DMC = dimethyl carbonate; DEC = diethyl carbonate; EMC = ethylmethyl carbonate; EA = ethyl acetate; MB = methyl butanoate; EB = ethyl butanoate.

Table 4: Organic ethers as electrolyte solvents [20].
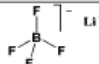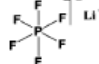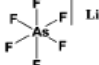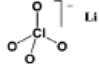
Solvent	Structure	M. Wt	$T_m/°C$	$T_b/°C$	η/cP 25 °C	ε 25 °C	Dipole Moment/debye	$T_f/°C$	d/gcm^{-3}, 25 °C
DMM		76	-105	41	0.33	2.7	2.41	-17	0.86
DME		90	-58	84	0.46	7.2	1.15	0	0.86
DEE		118	-74	121				20	0.84
THF		72	-109	66	0.46	7.4	1.7	-17	0.88
2-Me-THF		86	-137	80	0.47	6.2	1.6	-11	0.85
1,3-DL		74	-95	78	0.59	7.1	1.25	1	1.06
4-Me-1,3-DL		88	-125	85	0.60	6.8	1.43	-2	0.983
2-Me-1,3-DL		88			0.54	4.39			

DMM = dimethoxy methane; DME = dimethoxy ethane; DEE = diethoxy ethane; THF = tetrahydrofuran; Me = methyl; 1,3-DL = 1,3-dioxolane.

The solid electrolyte interface (SEI) film (Section1.5.3) formed on carbonaceous anode influences the choice of solvents for lithium ion electrolytes. The solvent system commonly used involves a combination of carbonates, usually EC/DMC [33]. Guyomard and Tarascon [34-35] discovered that this mixture offers a wide electrochemical stability window and has very good conductive properties; most importantly the formulation produces the best protective surface films on graphite electrodes thus minimizing solvent co-intercalation. EC is the indispensable solvent component while DMC serves as the co-solvent to increase the fluidity and reduce the high melting point of EC. The ability to effectively form the SEI protective film on graphite is the reason EC is mostly preferred to PC [36] despite the seemingly slight difference in molecular structure between the two. PC causes degradation in graphite electrodes as it co-intercalates with lithium ions resulting in exfoliation [11]. Other linear carbonates such as DEC [37-38] and EMC [39] can also be used as co-solvents as there is no significant difference between them and DMC in terms of electrochemical characteristics. The co-solvents on their own (that is, as single solvents) are unsuitable because of their inability to solvate lithium salts as well as their instability on the oxidizing

surface of cathode materials. However, ethers are more readily oxidized on the cathode since their α-hydrogens are highly susceptible to oxidation than the carbonates [40]. The gassing of lithium ion cells during long term cycling is also believed to arise from the co-solvents [20]. The choice of electrolyte salt is also important. An ideal electrolyte solute should meet the following requirements: (I) it should be able to completely dissolve and dissociate in the nonaqueous media, and the solvated ions (especially lithium ions) should be able to move in the media with high mobility. (II) The anion should be stable against oxidative decomposition at the cathode. (III) The anion should be inert to electrolyte solvents. (IV) Both the anion and the cation should remain inert toward the other cell components such as separator, electrode substrate, and cell packaging materials. (V) The anion should be non-toxic and remain stable against thermally induced reactions with electrolyte solvents and other cell components. The most commonly used salts together with some basic physical properties are listed in Table 5.

Table 5: Salts used in electrolytes for lithium ion cells [20].

Salt	Structure	M. Wt	T_m/ °C	$T_{decomp.,}$ / °C in solution	Al-corrosion	σ /mScm^{-1} (1.0 M, 25 °C)	
						in PC	in EC/DMC
LiBF$_4$		93.9	293 (d)	> 100	N	3.4 [a]	4.9 [c]
LiPF$_6$		151.9	200 (d)	~ 80 (EC/DMC)	N	5.8 [a]	10.7 [d]
LiAsF$_6$		195.9	340	> 100	N	5.7 [a]	11.1 [c]
LiClO$_4$		106.4	236	>100	N	5.6 [a]	8.4 [d]
Li Triflate	Li$^+$ CF$_3$SO$_3^-$	155.9	>300	>100	Y	1.7 [a]	
Li Imide	Li$^+$ [N(SO$_2$CF$_3$)$_2$]$^-$	286.9	234 [b]	>100	Y	5.1 [a]	9.0 [e]
Li Beti	Li$^+$ [N(SO$_2$CF$_2$CF$_3$)$_2$]$^-$				N		

LiBF$_4$ = lithium tetrafluoroborate; LiPF$_6$ = lithium hexafluorophosphate
LiAsF$_6$ = lithium hexafluoroarsenate; LiClO$_4$ = lithium perchlorate
Li Triflate = lithium trifluoromethanesulfonate;
Li Imide = lithium bis (trifluoromethanesulfonyl) imide
Li Beti = lithium bisperfluoroethanesulfonimide.

Each salt has some inherent drawbacks associated with it. Lithium tetrafluoroborate is less toxic than $LiAsF_6$ and has higher safety than $LiClO_4$ [41] but moderate in ionic conductivity due to its low dissociation constant [42]. Interestingly, electrolyte compositions based on $LiBF_4$ show improved performance at low and elevated temperatures (up to 50 $^\circ$C) than in $LiPF_6$ [43-44]. Lithium hexafluorophosphate is the most widely used electrolyte solute in lithium ion cells [45]. In 1990, when lithium ion technology moved from concept to product, it was used by Sony in the first generation lithium ion cell [46] and has remained the salt of choice since then. Its ability to effectively resist oxidation up to 5.1 V [35] in mixed carbonate solvent systems makes it one of the few salts that can actually support the operation of 4.0 V cathode materials. However, it is costly and sensitive towards ambient moisture. Lithium hexafluoroarsenate was found to be a superior salt to $LiClO_4$ as an electrolyte solute for lithium ion batteries [47] but very toxic due to the presence of arsenic. Lithium perchlorate is less hygroscopic and more stable to ambient moisture than other lithium salts but at high temperature and high current charge, it constitutes explosive hazards with most organic species and was found unsuitable for industrial purposes some decades ago [48-49]. A recent publication by Aurbach and co-workers has however revealed that $LiClO_4$ may still be considered for use in lithium ion batteries [50]. Despite the shortcomings in large-scale applications, it is frequently used as a salt of convenience in various laboratory tests because it is easy to handle and economical.

Polymer electrolytes (PEs) are also under extensive study for lithium ion cells. They offer the following advantages [51]: (1) suppression of dendritic growth. (2) Enhanced endurance to varying electrode volume. (3) Reduced reactivity towards lithium unlike in liquid electrolytes. (4) Improved safety. (5) Better shape flexibility and manufacturing integrity. PEs are of two types: Solid polymer electrolytes (SPEs) and gel polymer electrolytes (GPEs).

SPEs are composed of lithium salts (such as those discussed above) dissolved in high molecular weight poly-ether hosts, for example, poly (ethylene oxide) (PEO) and poly (propylene oxide) (PPO) which serve as solvents as well as mechanical matrix to support processability. GPEs are usually obtained by incorporating a larger quantity of liquid plasticizer and/or solvents to a polymer matrix that is capable of forming a stable gel with the polymer host structure. In order to improve the mechanical properties of the gel electrolytes, components that can be cross-linked and/or thermoset may also be added to the gel electrolyte formulation. They are characterised by a higher ambient ionic conductivity [52-53] but poorer mechanical properties when compared with pure SPEs. However, the ionic conductivities of SPEs at room temperature are less than 10^{-4} S/cm, which is not sufficient for power production [23]. As studies on SPEs still remain of academic interest without immediate commercial applications, GPE technology has been commercialised in lithium ion cells [54] and such cells are mostly designed as traction power in electric vehicles [55]. While the electrolyte chemistry profoundly affects the performance of the lithium ion cells, the fact remains that the choice of electrolyte components is dictated by the nature of the electrode materials.

1.5.2 Lithium ion intercalation electrodes

Typically, both electrodes in a lithium ion battery are intercalation compounds, which as their name implies, store Li^+ by inserting them into their crystal structure in a topotactic manner. The idea of intercalation electrodes for secondary lithium batteries was initiated in the 1970s [56] and since then, intensive research is being conducted to develop new materials. Considering the fact that the energy of a battery depends on the product of its voltage and capacity [11, 57], the use of high-capacity electrode materials that can also offer high cell voltages is therefore important for the development of high-energy-density batteries. A high

voltage can be achieved with negative (anode) and positive (cathode) electrodes that have, respectively, smaller and larger work functions ϕ_a and ϕ_b. The open-circuit voltage, V_{oc}, of a lithium cell is given by the difference in the lithium chemical potential between the cathode ($\mu_{Li(c)}$) and the anode ($\mu_{Li\,(a)}$) according to the equation [58]:

$$V_{oc} = \left(\mu_{Li(c)} - \mu_{Li(a)}\right)\big/F \tag{16}$$

The cell voltage is determined by the energies involved in both the electron transfer and the Li^+ transfer. Thus, Equation (16) is due to the energy involved in Li^+ transfer which is determined by the crystal structure and the coordination geometry of the site into/from which lithium ions are intercalated/de-intercalated while the energy involved in electron transfer is related to the work functions of the cathode and anode and is as shown in Equation 17 [59]:

$$V_{oc} = \left(\phi_c - \phi_a\right)\big/e \tag{17}$$

where e is the electronic charge. A schematic energy diagram of a cell at open circuit is shown in Figure 9. Thermodynamic stability considerations require the redox energies of the cathode (E_c) and the anode (E_a) to lie within the band gap, E_g of the electrolyte as depicted in Figure 9, so that no unwanted reduction or oxidation of the electrolyte occurs during the charge/discharge process. Thus, the electrochemical stability requirement imposes a limitation on the cell voltage as:

$$eV_{oc} = \left(\mu_{Li(c)} - \mu_{Li(a)}\right) < E_g \tag{18}$$
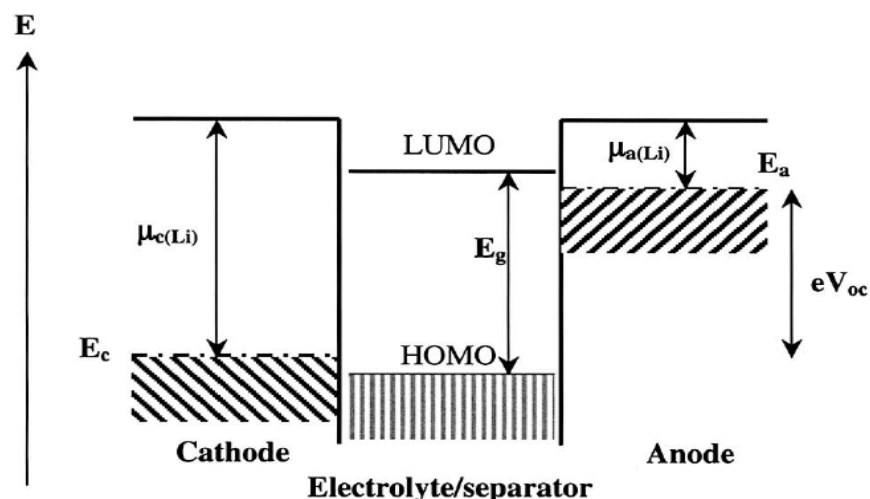
Figure 9: Schematic energy diagram of a lithium cell at open circuit. HOMO and LUMO refer respectively to the highest occupied molecular orbital and lowest unoccupied molecular orbital in the electrolyte [58].

The theoretical capacity of a material can easily be calculated from Faraday's 1st law of electrolysis, which states that 1 gram equivalent weight of a material will deliver a charge of 96485 coulombs (or 26.8 Ah) per mole of electron. This can be very useful when considering the synthesis of new materials. It can be readily assessed whether the material can compete with existing electrode materials in terms of specific capacity. For example, $LiFePO_4$ has an equivalent weight of 157.7 g/mol which translates into a theoretical capacity of: (26.8/157.7) 170 mAh/g, if the whole charge/discharge range is exploited. The electrode material should allow an insertion/extraction of a large amount of lithium to maximize the cell capacity. This is because $LiCoO_2$, for example, has a theoretical capacity of: 274 mAh/g but in practice, a capacity of about 130 mAh/g [31, 60] is achieved because only around 0.5 lithium ions per $LiCO_2$ formula could be reversibly cycled [31, 58] without causing cell capacity loss as a result of changes in the $LiCoO_2$ structure. A flat discharge curve (voltage-capacity profile) is also desirable for all intercalation electrodes as this means that the voltage remains constant

as the battery is used up. Therefore, intercalation electrode materials are selected based on the following requirements:

- the cathode intercalation compound should have a high lithium chemical potential and work fuunction in order to maximize the cell voltage. This implies that the transition metal ion, M in $Li_xM_yX_z$ (X= anion) should have a high oxidation state.

- The intercalation compound should allow an insertion/extraction of a large amount of lithium to maximize the cell capacity.

- The lithium insertion/extraction process should be reversible with no or minimal changes in the host structure over the entire range of lithium insertion/ extraction in order to provide a good cycle life for the cell.

- The intercalation compound should support good electronic and lithium ion conductivities to minimize cell polarizations. The high conductivities are essential to support a large current density and also a high power density.

- The insertion material should be chemically stable over the entire voltage range without undergoing any reaction with the electrolyte.

- The redox energy of the cathode in the entire range of lithium insertion/extraction should lie within the band gap of the electrolyte as shown in Figure 3 to prevent any unwanted oxidation or reduction of the electrolyte.

- From a commercial point of view, the intercalation compound should be inexpensive, environmentally friendly, and lightweight to minimize the battery weight.

The electrochemical potential ranges of some lithium intercalation compounds versus metallic lithium are given in Figure 10:
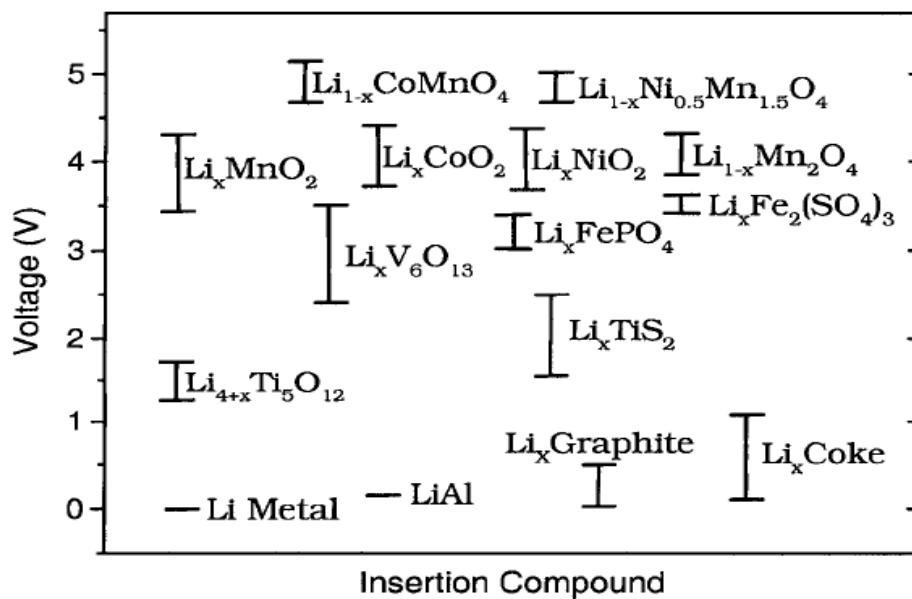
Figure 10: Electrochemical potential ranges of some lithium intercalation compounds in reference to metallic lithium metal [58].

1.5.3 Anode

Since lithium metal constituted a safety problem, attention shifted to the use of carbonaceous materials. Anodes of carbon origin have the ability to reversibly intercalate lithium [29, 61] and the fact that the chemical potential of lithiated carbon is close to that of metallic lithium, as shown in Figure 10, makes them viable alternatives to lithium metal. Furthermore, they show long term cycling performance superior to lithium alloys due to their better dimensional stability. In addition, most carbon materials suitable as anodes for lithium ion cells are cheap and abundant compared with the other materials such as polymers, transition metal oxides or chalcogenides. Although carbon has several allotropes (graphite, coke, activated carbon, carbon fibre), graphite and its disordered forms are used as practical anode materials. Dahn et al studied the dependence of the intercalation process on the crystal structure of a variety of carbons. It was found that the morphology, crystallinity and orientation of crystallites determine the electrochemical characteristics of carbonaceous materials; and together with the anode thickness, it plays an important role in the number of lithium ions that can be exchanged [62-63]. For example, coke has a turbostratic structure and can intercalate a low amount of lithium to form Li_xC_6, where $0 < x < 0.5$ [36]. Graphite, however, which almost has a perfectly layered structure that consists of hexagonal graphene sheets of atoms weakly bonded together by van der Waals forces into an ABAB stacking sequence along the c-axis as shown in Figure 11, is able to intercalate twice the amount of lithium forming Li_xC_6, where
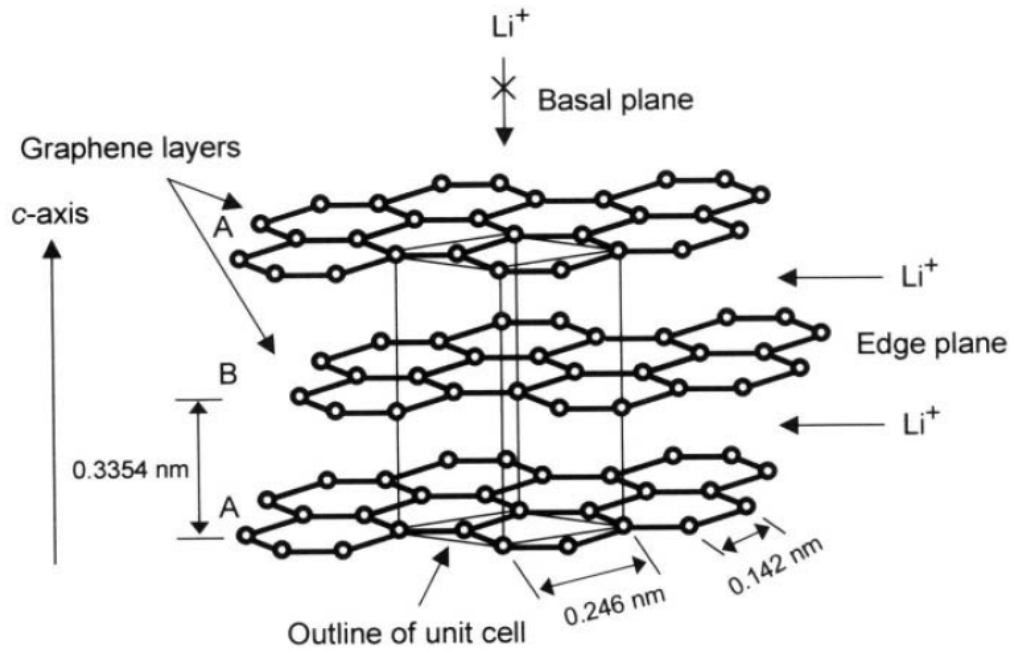
Figure 11: Crystal structure of hexagonal graphite showing the ABAB stacking of graphene sheets and the unit cell [64].

$0 < x < 1$ and gives a higher capacity of 372 mAh/g [36] when compared to the 185 mAh/g obtained from coke. Peled in 1979 developed a model to describe the passivation on lithium metal [65] which he referred to as "solid electrolyte interface" (SEI). Based on this model, Dahn and co-workers discovered that during the first electrochemical cycles, the electrolyte decomposes on the carbon anode surface, forming the SEI protective film. Once this film that is an ionic conductor but an electronic insulator forms over the entire graphite surface, the electrolyte does not further decompose and the cell can be cycled continuously with no capacity loss [36]. Coke-type carbons were utilised in the first generation lithium ion cells [11]. However, due to the higher capacities, lower costs, desirable lithium intercalation ratios and flatter discharge profiles of graphite, graphitic anodes are currently used commercially in all lithium ion batteries [64]. The addition of carbon black to graphite results in a better capacity retention [62] although it lowers lithium intercalation. It is possible to exceed the lithium intercalation in graphite beyond LiC_6 [66] but the formation of dendrite on the anode

surface [62] raises concern for safety. The lithium ion cell is usually manufactured in a fully discharged state. This is due to the fact that lithiated carbon is thermodynamically unstable [11, 25, 51]. Thus, the anode is made with a non-lithiated carbon and lithiation is carried out by subsequent formation of the cell whereby during the first charge, lithium ion from the cathode intercalates into the carbon anode to form the SEI film which kinetically protects the air-sensitive lithiated electrode. While the search for a superior lithium intercalation anode material continues, researchers posit that nanoscale silicon and tin are the most promising anode materials for the next-generation of lithium ion batteries [6] as both allow for a maximum lithium insertion that is over four times greater than that of graphite; that is, $Li_{4.4}Si$ and $Li_{4.4}Sn$, with theoretical specific capacities of 4200 and 996 mAh/g, respectively [67].

1.5.4 Cathode

Worldwide research and development is in progress for rechargeable lithium ion batteries because of their wide applications in portable electronics and electric/hybrid vehicles. Much of this effort is focused on developing the cathode materials because the performance and cost of the batteries are often decided by the properties of the cathode materials in use [68-69]. A survey of the main properties of intercalation compounds and their impact on battery characteristics revealed that a 50% increase in the specific capacity of the cathode material results in an overall 28% improvement in the specific energy of the cell whereas the same change in the anode material gives only a 13% increase [70]. A further illustration is given in Figure 12 where the cathode materials are seen to have lower capacities than the anodes indicating that the cathodes are the real bottlenecks in lithium ion battery development.
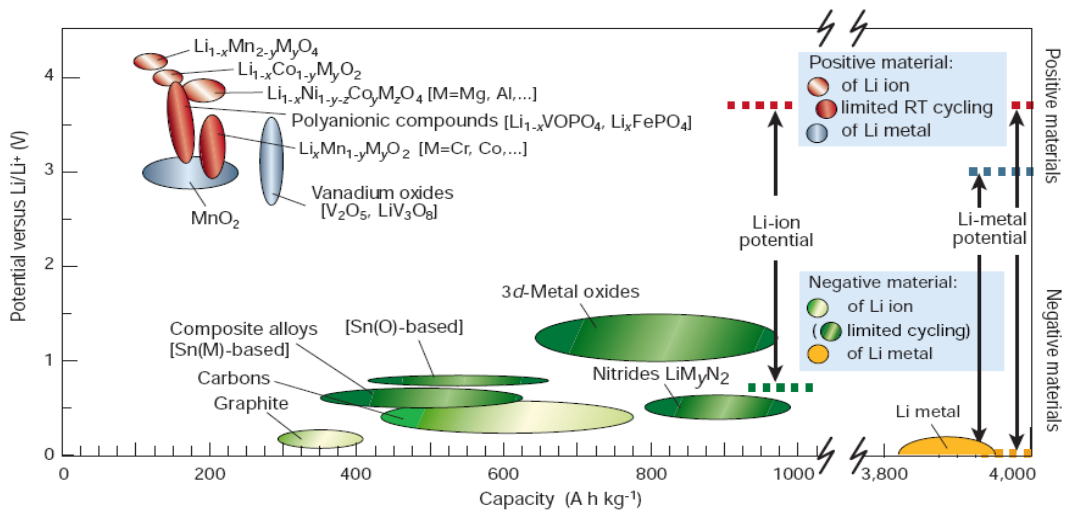
Figure 12: Voltage versus capacity for cathode and anode materials presently used or under serious considerations for next generation of rechargeable Li-based batteries [13].

Besides the big difference in capacity between the cathode and the anode materials, attention is drawn to the huge difference in capacity between lithium metal and the other negative electrodes, which explains why it remains a main attraction as a potential anode. Hence the great interest in solving the problem of dendrite growth [13].

There are three main types of cathode materials that have been investigated for use in lithium ion batteries [25]: (1) inorganic transition metal oxides and chalcogenides (2) organic molecules and (3) polymers. Class 1 constitutes the largest number of cathode materials evaluated. Table 6 represents an overview of some of these materials. Based on the type of void spaces available for lithium insertion, transition metal oxides and chalcogenides can be classified as one, two or three-dimensional structures. Examples of one dimensional host are transition metal trichalcogenides like TiS_3 and $NbSe_3$ which possess unlinked channels. The two dimensional intercalation cathode materials include the layered dichalcogenides of the transition metals Ti, Nb, Ta, Mo and W; as well as the layered transition metal oxides of the

formula, $LiMO_2$ (M = V, Cr, Fe, Co and Ni). These structures have empty spaces between the MO_2 layers that can accommodate lithium ion. The three dimensional cathode materials comprise the Mn, Co and Fe oxide spinels; high-valent oxides of vanadium and complex frame work structures like iron phosphates and sulphates. They have cross-linked channels that are sufficiently large to allow lithium insertion.

Table 6: Characteristics of representative cathode materials for lithium batteries.

positive electrode material	Molecular weight	Density [kg/L]	Reversible range Δx	Theoretical specific charge [Ah/kg]	Theoretical charge density [Ah/L]
Charged					
TiS_2	112.01	3.27	1	239	782
MoS_2	160.06	5.06	0.8	134	678
V_2O_5	181.88	3.36	1	147	495
V_6O_{13}	5i3.64	3.91	3.6	188	734
MnO_2	86.94	5.03	0.5	154	775
$NbSe_3$	329.81	8.7	3	244	2121
Discharged					
$LiCoO_2$	97.87	5.16	0.5	137	706
$LiNiO_2$	97.63	4.78	0.7	192	919
$LiMn_2O_4$	180.82	4.28	1	148	634

The values are either for fully lithiated (discharged) host materials or lithium-free (charged) host materials, and the specific charges are based on a reversible range of the lithium content during the charging/discharging process.

The major inorganic cathode materials can be simply categorised into: (a) layered oxides (b) spinels and (c) olivines.

1.5.4.1 Layered oxides

An ideal lithium metal oxide, $LiMO_2$, has the α-$NaFeO_2$-type structure which can be regarded as a distorted rock salt superstructure as shown in Figure 13.
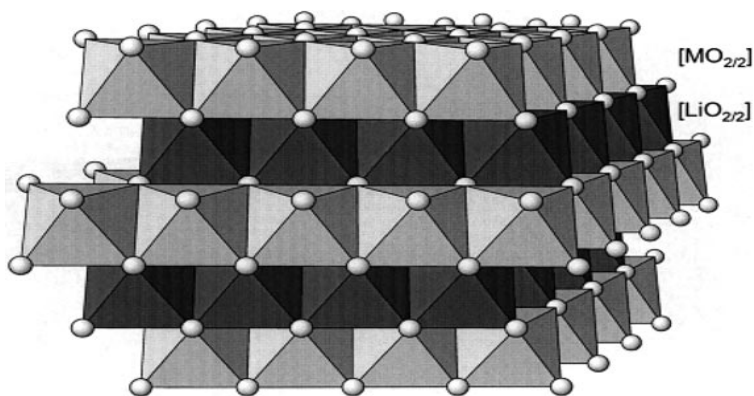
Figure 13: The two dimensional crystal structure of $LiMO_2$ (M = Ni, Co, V) of the α-$NaFeO_2$-type [25].

The oxygen sub-lattice in the rock-salt structure takes an ABCABCABC cubic close-packed stacking sequence along the c-axis. The oxides crystallize in a layered structure in which the lithium and transition metal cations are ordered in the octahedral interstitial sites formed by the cubic close-packed oxygen framework in such a way that the rigid host possesses MO_2 layers composed of edge sharing MO_6 octahedra [25] while lithium resides in octahedral LiO_6 coordination leading to alternating (111) planes of the cubic rock-salt structure to give a layer sequence of O-Li-O-M-O along the c axis [58] as shown in Figure 14. This (111) ordering induces a slight distortion of the lattice to hexagonal symmetry. The structure is designated as the O3 layer structure since the lithium ions occupy the octahedral sites (O refers to octahedral) and there are three MO_2 sheets per unit cell. The structure with a strongly (covalently) bonded MO_2 layers allows a reversible de-intercalation/intercalation of lithium ions from/into the lithium planes. The interconnected lithium ion sites through the edge-shared LiO_6 octahedral arrangement between the MO_2 layers provide fast two-dimensional lithium ion diffusion leading to high conductivity. The fully delithiated host (assuming it does not transform) possesses the layered $CdCl_2$ structure type [25]. On the other hand, the edge-shared MO_6 octahedral arrangement with a direct M-M interaction can

39

provide good electronic conductivity depending on the electronic configuration of the M^{3+} ion. As a result, the $LiMO_2$ oxides crystallizing in the O3 structure are attractive as cathodes [58].

<div align="center">(A)   (B)</div>
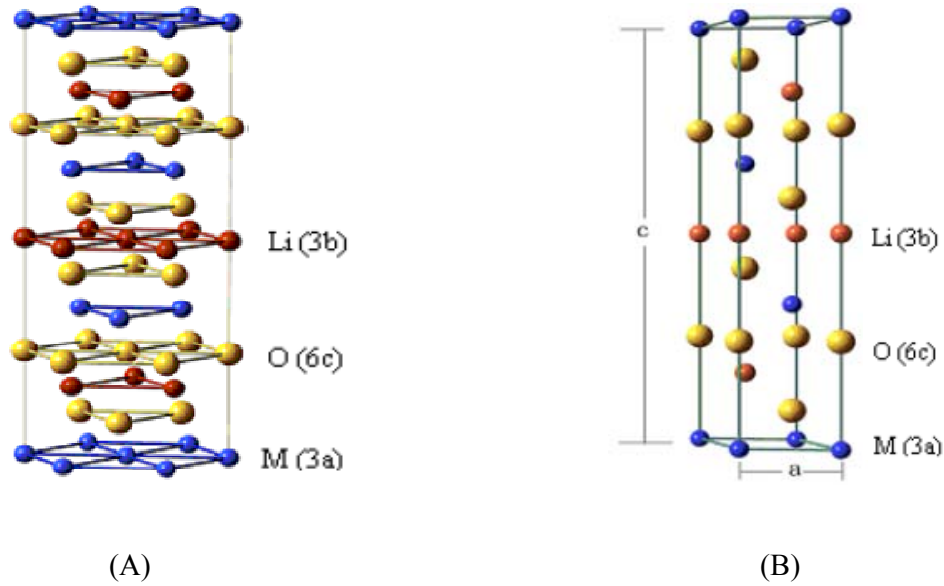
Figure 14: (A) Ball-stick structure model of hexagonal layered $LiMO_2$ (B) unit cell of $LiMO_2$ [68].

The oxides are thermodynamically stable only in the intercalated $LiMO_2$ state. This is due to the high electronegativity of oxygen, which leads to a higher ionic character of the metal oxygen bonds. The resulting negative charge of the transition metal-oxygen layers causes repulsive interactions between adjacent layers which are compensated by positively charged ions between the oxygen layers. The compounds of interest among the group include: $LiCoO_2$, $LiNiO_2$ and the mixed oxides, $Li(Co, Ni)O_2$ [25].

1.5.4.1.1 LiCoO$_2$

The use of LiCoO$_2$ as a cathode material was suggested for the first time in 1980 by Goodenough and co-workers [71]. It was later utilised in the world's first commercial lithium ion battery introduced by Sony in 1990. It possesses the α-NaFeO$_2$ layered structure in the trigonal R$\bar{3}$m space group with Co at the 3a site (0, 0, 0), Li at the 3b site (0, 0, 0.5) and O at the 6c site (0, 0, 0.25) [72] as shown in Figure 13. The lattice parameters in the hexagonal setting have been experimentally measured as a = 2.816 Å and c = 14.058 Å [72]. It should be noted that the "a" and "b" constants in hexagonal crystal structures are equal. Hence, reference is made only to the "a" and "c" constants. In the layered structure of LiCoO$_2$, a cubic close-packed oxygen array provides a two-dimensional network of edge-shared CoO$_6$ octahedra for lithium ions [73]. LiCoO$_2$ therefore adopts the O3 layer structure as shown in Figure 10 with an excellent ordering of the Li$^+$ and Co^{3+} ions on the alternate (111) planes of the rock salt lattice.
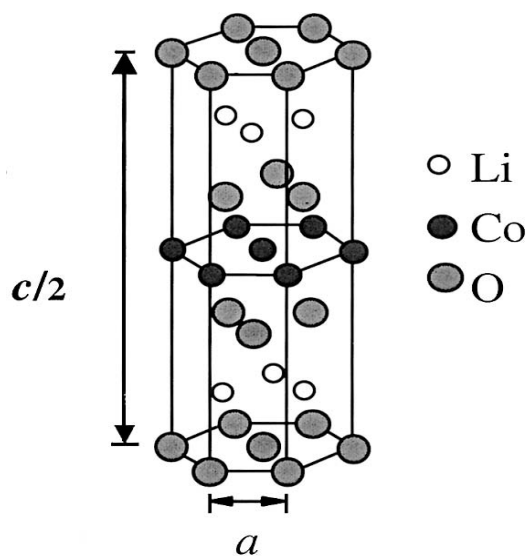
Figure 15: Crystal structure of LiCoO$_2$ having the O3 layered structure [58].

A high lithium chemical potential associated with the highly oxidized $Co^{3+/4+}$ provides a high cell voltage of around 4 V and the discharge voltage does not change significantly with the degree of lithium intercalation/de-intercalation [58]. Lithium diffusion coefficient in $LiCoO_2$ is 5×10^{-9} cm^2/s while cycling at a current density of 4 mA/cm^2 [31, 74]. On complete removal of lithium, the oxygen layers rearrange themselves to give a hexagonal close packing of the oxygen in CoO_2 [31, 75]. Between these composition limits, several phases are formed with varying degrees of distortion of the cubic close-packed oxygen lattice. Thus, $LiCoO_2$ is not stable and can undergo performance degradation or failure when overcharged [76-78]. A stable delithiated structure can only be obtained by a 50% reversible cycling of lithium, which limits the maximum practical specific capacity of $LiCoO_2$ to about 130 mAh/g [31, 58, 79] although it has been reported that surface coatings may improve its capacity [80-81]. Apart from the moderate specific capacity, $LiCoO_2$ also has the disadvantages of being unsafe, toxic, and costly due to the limited availability of cobalt. However, it remains the most commonly used cathode material for lithium ion batteries but a search is underway for materials with better capacity, lesser toxicity and lower cost than cobalt.

1.5.4.1.2 LiNiO$_2$

This compound is isostructural with $LiCoO_2$ and therefore crystallizes in the O3 layered structure but it is lower in cost and with a practical specific capacity of about 150 mA/g; which is higher than that of $LiCoO_2$ [82-83]. The $Ni^{3+/4+}$ couple with a high lithium chemical potential provides a high cell voltage of around 4 V like $LiCoO_2$ [58]. Its main drawback as a cathode material is that of being less stable and less ordered than the more popular cobalt analogue due to poor cyclability and unsatisfactory thermal stability [84-86]. In addition, it is difficult to synthesize stoichiometric $LiNiO_2$ and there is no clear evidence that such has been achieved [16, 31]. The non-stoichiometry is ascribed to the tendency to form a nickel-rich

non-stoichiometric phase which results in excess nickel ions occupying sites in the lithium plane as in $Li_{1-z}Ni_{1+z}O_2$ [87], with subsequent reduction in lithium diffusion coefficient and electrochemical performance. The migration of nickel ions from the octahedral sites of the nickel plane to the octahedral sites of the lithium plane via neighbouring tetrahedral sites, is attributed to a lower octahedral-site stabilization energy (OSSE) associated with Ni^{3+} ions in the low spin state [58]. This defect in the stoichiometry of the layered structure can however, be stabilized by incorporating cobalt into $LiNiO_2$ as it is reported to increase the degree of ordering by suppressing cation disorder and Jahn–Teller distortion thereby keeping the nickel in its layer rather than in the lithium plane [88-92]. The optimal doping content was determined to be between 20-30% cobalt [68, 89]. Doping $LiNiO_2$ with some elements such as magnesium as in $LiNi_{1-y}Mg_yO_2$ [93] and aluminium as in $LiAl_{1/4}Ni_{3/4}O_2$ [94] limits the various phase transitions and improves cycling performance. Many studies have deployed this doping strategy in multiple substituted nickel oxides such as $LiNi_{0.8-y}Ti_yCo_{0.2}O_2$ [95] and $LiNi_{1-y-z}Co_yAl_zO_2$ [31]. The latter is expected to find use in advanced lithium batteries for hybrid electric vehicles [31]. Poor thermal stability makes $LiNiO_2$-based batteries unsafe. It is reported that thermal stability is significantly lower in $LiNiO_2$ than in $LiCoO_2$ and $LiMn_2O_4$. The increasing order of thermal stability is: $LiNiO_2 < LiCoO_2 < LiMn_2O_4$ [96]. Guilmard *et al* studied the thermal stability of lithium nickel oxide derivatives [97-98]. The study showed that the stability of the delithiated material decreases with decreasing lithium content. Generally, Cathode materials show good thermal stability at full lithiation, but would decompose at low temperature and low lithium content [68]. In other words, the delithiation state of the material is a first order parameter of its thermal stability [70]. The thermal stability of delithiated nickel-rich phases can as well be modified by substitution of nickel with other cations. Whatever the nature of the substitution, layered materials with the lowest amount of foreign cations in the lithium site must be obtained in order to maintain a very

high electrochemical activity [86]. From the foregoing, enhancing structural and thermal stability during cycling is one of the major challenges in the practical application of layered $LiNiO_2$-based cathode materials. It is expected that the multiple substitution strategy will pave the way for the much anticipated breakthrough in its commercialisation.

1.5.4.1.3 Other layered oxides

$LiVO_2$ and $LiCrO_2$ crystallize in the O3 structure but unlike $LiCoO_2$ and $LiNiO_2$, both are not promising cathode materials. Approximately one third of the vanadium ions in Li_xVO_2 (x= 0.3) migrate from the vanadium layer to the lithium planes due to low OSSE [25, 58] while it is difficult to extract lithium from $LiCrO_2$. $LiTiO_2$ is difficult to synthesize and $LiFeO_2$ synthesized by high temperature procedures does not adopt the O3 structure. Layered $LiMnO_2$ is the most attractive in terms of safety, cost and toxicity when compared to other cathode materials with the $LiMO_2$ composition. Unfortunately, it is thermodynamically unstable at elevated temperature and the synthetic route is quite cumbersome [31, 99-100]. The thermodynamically stable form does not have the α-$NaFeO_2$ structure but a modified rock salt structure with a distorted cubic close-packed oxygen anion array and the orthorhombic space group, Pmmn. The lithium and manganese cations occupy the 3a and 3b octahedral interstitial sites respectively in alternating zigzag layers of edge-sharing LiO_6 and MnO_6 octahedra [25, 101]. Metastable layered $LiMnO_2$ can be formed from layered $NaMnO_2$ by ion exchange [99, 102]. The resultant structure is distorted from the $R\bar{3}m$ space group to monoclinic C2/m by the collective Jahn-Teller distortion but it retains the connectivity of the layered structure; that is, distorted cubic close-packed oxygen framework with alternating layers of lithium and manganese ions. However, both the O3-type $LiMnO_2$ and the conventional $LiMnO_2$ (with orthorhombic structure) transform to the spinel-like structure leading to poor cyclability.

1.5.4.2 Spinels

Oxides with the general formula LiM_2O_4 (M = Mn, Ti, and V) crystallize in the normal spinel structure as shown in Figure 11. The oxygen anions occupy the crystallographic 32e sites of the $Fd\bar{3}m$ space group while the Li^+ and the $M^{3+/4+}$ ions occupy, respectively, the 8a tetrahedral and 16d octahedral sites of the cubic close-packed oxygen array to give a cation distribution of $(Li)_{8a}[M_2]_{16d}O_4$. A strong edge-shared octahedral $[M_2]O_4$ array permits diffusion of lithium ions from the tetrahedral sites without collapsing the three-dimensional $[M_2]O_4$ spinel framework [103-104].

○ Li (8a site)

◉ Mn (16d site)

● O (32e site)
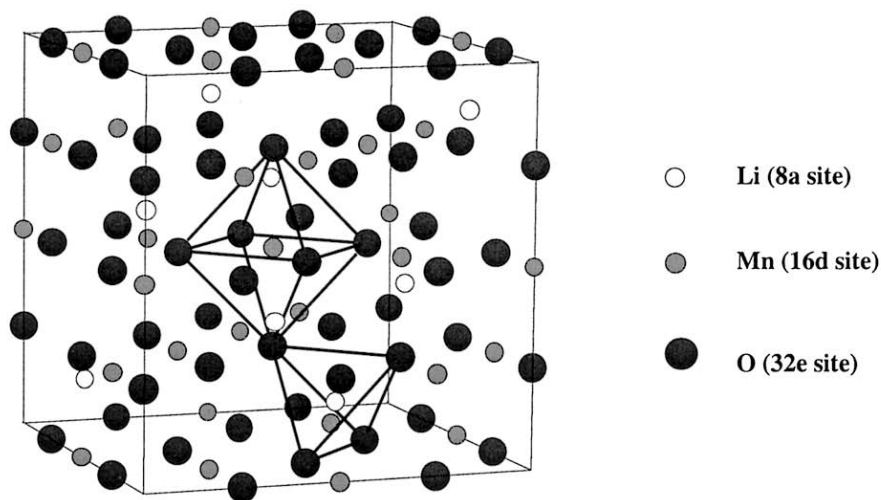
Figure 16: Crystal structure of spinel $LiMn_2O_4$.

Additional lithium can also be inserted into the empty 16c octahedral sites of the spinel framework to give the lithiated spinel $Li_2[M_2]O_4$ [25, 58]. However, an electrostatic repulsion between the lithium ions in the 8a tetrahedral and 16c octahedral sites, which share common faces, causes a displacement of the tetrahedral lithium ions into the neighbouring empty 16c sites to give an ordered rock salt structure having a cation distribution $[Li_2]_{16c}[M_2]_{16d}O_4$. Thus theoretically, two lithium ions per LiM_2O_4 formula unit could be reversibly intercalated/de-

intercalated. While the edge shared MO_6 octahedral arrangement with direct M-M interaction, as in the layered $LiMO_2$ oxides, provides good electrical conductivity, the interconnected interstitial lithium sites in the three-dimensional spinel framework provide good lithium-ion conductivity. This makes the spinel LiM_2O_4 oxides attractive cathodes for lithium ion batteries. $LiMn_2O_4$ is the major cathode material in the spinel group.

1.5.4.2.1 LiMn$_2$O$_4$

Spinel $LiMn_2O_4$ is a low cost, environmentally friendly alternative to the layered oxide cathodes. The extraction of two lithium ions from the $Li[Mn_2]O_4$ spinel framework occurs in two distinct steps [104]. While the lithium de-insertion from the 8a tetrahedral sites reversibly proceeds at around 4 V with the maintenance of the initial cubic spinel symmetry, extraction from the 16c octahedral sites occurs at around 3 V by a two-phase mechanism involving the cubic spinel $Li[Mn_2]O_4$ and the tetragonal lithiated spinel $Li_2[Mn_2]O_4$. The cubic to tetragonal transition is due to the Jahn-Teller distortion of the Mn^{3+} ion [25, 58, 70]. This transition induces a change in the c/a ratio as well as in the unit cell volume which is too severe for the electrodes to maintain structural integrity during the charge/discharge cycle. As a result, $LiMn_2O_4$ exhibits rapid capacity fade in the 3 V regions. Hence, $LiMn_2O_4$ could only be used in the 4 V regions with a limited practical capacity of around: 120 mAh/g which corresponds to an extraction/insertion of: 0.4 lithium per manganese; Unfortunately, even with a limited capacity, $LiMn_2O_4$ tends to exhibit capacity fade in 4 V region as well especially at elevated temperatures (50 °C) [58, 105]. The fading, particularly at elevated temperature, is far worse than that observed with nickel or cobalt-rich materials [70]. Apart from the poor capacity retention in $LiMn_2O_4$ during cycling [106], capacity loss has also been observed during storage due to dissolution of manganese in the electrolyte [107] or due to

changes in the particle morphology or crystallinity [108]. A lot of research work is still ongoing to understand and improve the behaviour of $LiMn_2O_4$.

1.5.4.3 Olivines

In the late 1980's, Manthiram and Goodenough [109-110] discovered that other materials based not on the oxygen anion but on a polyanion network (XO_4^{2-}; X = S, Mo and W) could be used as lithium insertion/extraction hosts. The use of cathode materials containing these compact tetrahedral polyanion structural units was predicated on the assumption that the covalently bonded groups would, through inductive effect, increase the cell voltage [111]. Sequel to this discovery, Padhi *et al*. [112] reported the reversible cycling of lithium ion in phospho-olivine cathodes, $LiMPO_4$ (M = Fe, Mn, Co, Ni). The olivine structure, as shown in Figure 17 for $LiFePO_4$, consists of a slightly distorted hexagonal close-packed oxygen framework. The phosphorus atoms occupy the tetrahedral 4c sites while the lithium and M atoms occupy the octahedral 4a and 4c sites, respectively. The two octahedral sites are crystallographically distinct and differ in size. The LiO_6 octahedra form edge-sharing chains along the b-axis in the alternate a-c plane while the MO_6 octahedra are linked through zigzag corners in the other a-c plane. One MO_6 octahedron shares common edges with two LiO_6 octahedra and a PO_4 tetrahedron. The PO_4 groups share one edge with an MO_6 octahedron and two edges with LiO_6 octahedra.
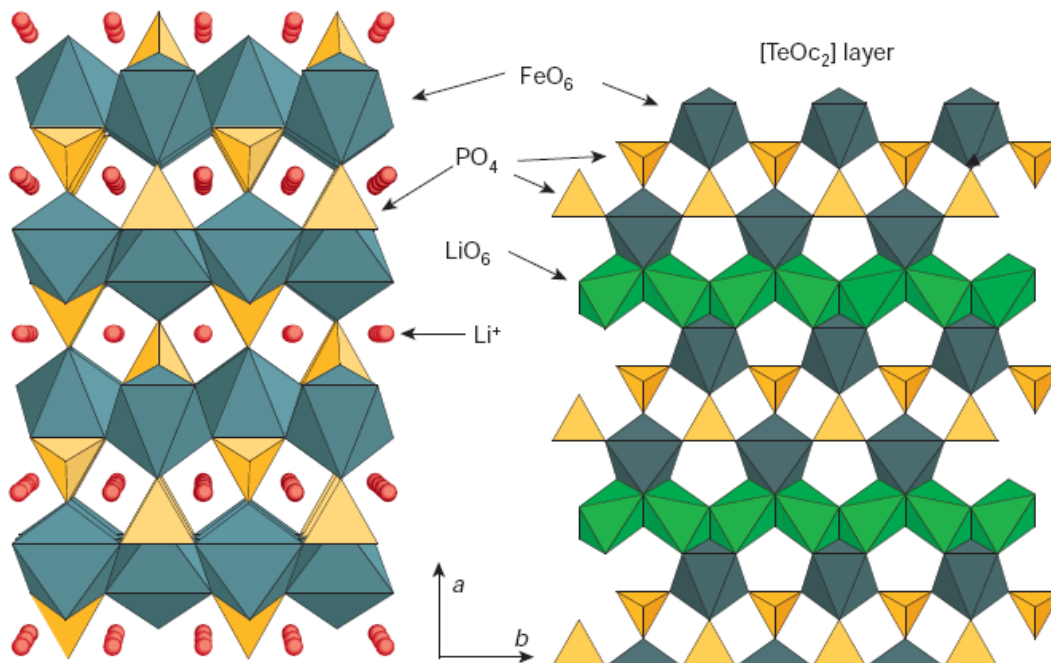
Figure 17: The crystal structure of olivines [13].

On the left, is the expanded view of the framework built on FeO_6 octahedra and PO_4 tetrahedra, with lithium ions in red. On the right, is the restricted view of Li, Fe and P distribution between two distorted, hexagonal close-packed oxygen-dense layers ($P_{Td}[LiFe]_{oct}.O_4$) [13]. Comparing the different olivine compounds, $LiMnPO_4$ has a higher potential than $LiFePO_4$ but its electrochemical behaviour is shrouded in controversy and generates little interest due to its much poorer rate capability [31, 113]. Cobalt and nickel olivines are more thermally unstable upon delithiation and have low capacities, extremely low conductivities and very high oxidation potentials which makes them unsuitable for use in known electrolytes [113]. $LiFePO_4$ however, is the most important member of the group.

1.5.4.3.1 LiFePO$_4$

LiFePO$_4$ occurs in nature as the mineral, triphylite and crystallizes in the olivine structure with the pmnb space group [112, 114] having cell parameters: a = 6.008 Å; b = 10.334 Å; c = 291.392 Å with volume of the unit lattice as 291.392 Å^3. The central Fe atom together with surrounding oxygen atoms forms the FeO$_6$ octahedron which shares edges with two LiO$_6$ octahedra and one PO$_4$ tetrahedron. Lithium ions reside within the octahedral channels in a three-dimensional zigzag framework formed by corner-shared FeO$_6$ octahedra and edge-shared PO$_4$ tetrahedra as depicted in Figure 18. The presence of the heavier PO$_4$ groups restricts free movement of lithium ions to a one-dimensional pattern. LiFePO$_4$ has an exceptionally flat discharge potential at about 3.4 V vs. lithium with a capacity of 170 mAh/g which is comparable to that of stabilized LiNiO$_2$ but higher than that obtained for LiCoO$_2$. Delithiation of LiFePO$_4$ results in FePO$_4$ in which the Fe^{2+} ions are oxidised to Fe^{3+}, leaving the 3D olivine framework intact. Thus, there is no structural change upon lithium extraction/insertion. Only a slight variation in lattice parameters is observed [115]. The excellent reversibility of the cells is due to the striking similarity of the two structures as shown in Figure 18:
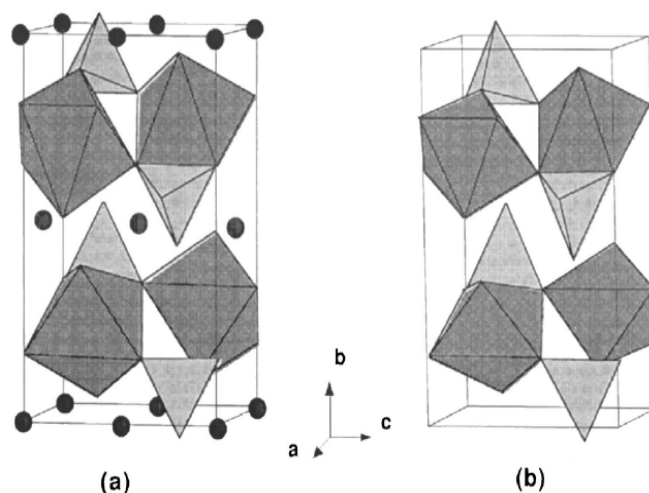
Figure 18: Crystal structures of (a) $LiFePO_4$ and (b) $FePO_4$ consisting of FeO_6 octahedra and PO_4 tetrahedra. The circles represent lithium ions [112].

This structural stability imparts a good cycle life on $LiFePO_4$ cells as there is no obvious capacity fade even after several hundred cycles [112]. In addition to its attractive electrochemical features, it is based on iron, an element that is abundant, inexpensive and environment-friendly as shown in Table 7.

Table 7: Cost, deposits and environmental regulation value of transition metals [57].

	Fe	Mn	Ni	Co
Market price of metal (\$/kg)	0.23	0.5	13	25
Atomic contents in crust (ppm)	50,000	950	75	25
Permissible amount in air (mg/m^3)	10	5	1	0.1
Permissible amount in water (mg/l)	300	200	13.4	0.7

Thermal stability is an important issue in large scale applications of lithium ion batteries. Cathode materials may potentially release oxygen at elevated temperatures which can combust the electrolyte and lead to runaway reactions and fire. While the cathode in its

discharge state is usually relatively stable with respect to oxygen release, cathodes based on layered $LiCoO_2$, $LiNiO_2$, and spinel $LiMn_2O_4$ decompose with oxygen evolution [96] when heated in the highly oxidized charged state. Olivine $LiFePO_4$ on the other hand, offers much better thermal stability [116-117] and low oxidative ability with the electrolyte. It has been tacitly assumed that all materials based on the phosphate polyanion would share this advantage [118-119]. Unfortunately, $LiFePO_4$ has a poor electronic conductivity at 10^{-9} S/cm [114, 120] which was found to be far lower than that of $LiCoO_2$ [121] and $LiMn_2O_4$ [122] at 10^{-3} S/cm and 10^{-4} S/cm, respectively. The poor kinetics of lithium intercalation in $LiFePO_4$ caused by the intrinsic low electronic conductivity and low lithium diffusion coefficient [123] could adversely affect its practical capacity especially at higher current densities. Since its discovery, research has been focused on improving its performance [124-125].

1.6 Nanomaterials

Nanomaterials are structures with dimensions in the nanoscale range, normally between 1 and 100 nm [126-128]. The use of nanomaterials as building blocks for devices not only helps to downscale conventional technologies by at least an order of magnitude but also offers a cheaper and more environmentally friendly production route, due to a drastic reduction in the necessary amount of raw materials. The chemical and physical properties of substances can be considerably altered and fine-tuned when they exist on a nanoscopic scale. An increase in the specific surface area is one of such changes that could occur when the particle size of a material is scaled down to nanometre dimensions. Typical applications of nanomaterials include energy conversion, electrochemistry, catalysis and environmental chemistry, where the use of nanomaterials increases efficiency, sensitivity and response time. Nanostructured materials are becoming increasingly important for electrochemical energy storage [17, 129-130] because of the unusual mechanical, electrical, optical and structural properties endowed

by confining their dimensions and because of the combination of bulk and surface properties to the overall behaviour. Most attempts to improve the design of lithium ion batteries have tackled the problem at the macroscopic level but work is now focusing on the nanoscale [15]. There are three primary types of nanoscale building blocks that may be used for further device fabrication and applications [131]:

(i) 0-D (e.g., nanoparticles, nanoclusters, nanocrystals, quantum dots)

(ii) 1-D (e.g., nanotubes, nanofibres, nanowires, nanoribbons)

(iii) 2-D (e.g. graphene/graphene oxide sheets)

The direct incorporation of these nano-architectures in existing materials improves their properties. The small particle size of nanoscale materials allows short diffusion distances in lithium ion cells which translate into high rate capability of active materials and increased capacity utilization [19, 61, 132].

1.6.1 Carbon nanotubes

Carbon nanotubes (CNTs) are well-ordered, all–carbon, graphitic nanomaterials with lengths ranging from several hundred nanometres to several micrometers; and diameters from a few to tens of nanometres which results in a high aspect ratio [133-134]. They are classified as either single-wall carbon nanotubes (SWNT) with internal diameters of 0.7 – 2 nm [135] or multi-wall carbon nanotubes (MWNT) which typically have inner diameters of 2 – 30 nm [136]. Conceptually, the nanotubes are viewed as rolled-up structures of one or multiple layers of graphene sheets for SWNTs and MWNTs respectively. For the MWNTs, the number of concentric graphene sheets can range from 2 to ~100 [137]. These one dimensional carbon allotropes have high electrical conductivity, high surface area, high mechanical strength, and excellent chemical and thermal stability. As a result, CNTs are highly attractive for fundamental research and commercial applications.

1.7 Electrochemical techniques

1.7.1 Cyclic voltammetry

The main target of an electrochemical experiment is to study in detail the electron transfer process of a material and an understanding of the redox behaviour of the material requires the study of the kinetic aspects of the electron transfer processes exhibited by that material as well as the thermodynamic aspects of such electron transfer processes.

A preliminary electrochemical overview of the redox aptitude of a material can easily be obtained by:

(a) Varying with time the potential applied to an electrode immersed in a solution of the material under study and recording the relevant current-potential curves. These curves first reveal the potential at which redox processes occur.

(b) Determining the size of the currents generated by the relative Faradaic processes which is normally proportional to the concentration of the active species.

(c) Examining the shape of the response as a function of the potential scan rate. This allows one to determine whether there are chemical complications (adsorption or homogeneous reactions) which accompany the electron transfer processes.

Cyclic voltammetry (CV) certainly constitutes the most useful technique for a preliminary determination of the redox properties of a given material.

In CV, the potential is ramped from an initial potential (E_i) and at the end of its linear sweep, the direction of the potential scan is reversed, usually stopping at the initial potential. The potential may commence with additional cycles. The potential at which the change in direction occurs is also known as the switch potential (E_λ). The scan rate between E_i and E_λ is the same as that between E_λ and E_i and the values of the scan rate $v_{forward}$ and $v_{reverse}$ are

always written with positive numbers. Oxidation usually takes place during the forward part of the CV, if scanned from a negative to a positive potential. The reverse part of the CV will then represent reduction, with the potential running from a positive to a negative potential. However, if the potential is scanned from a positive to a negative value, then reduction would occur during the forward part of the CV scan and oxidation during the reverse CV scan. Important parameters are usually obtained from cyclic voltammograms for analysis of reversible reaction properties and properties of an electroactive sample. These parameters include anodic and cathodic peak potentials, denoted as E_{pa} and E_{pc}, respectively as well as anodic and cathodic peak currents denoted as I_{pa} and I_{pc}, respectively. A typical cyclic voltammogram illustrating these parameters is shown in Figure 19.
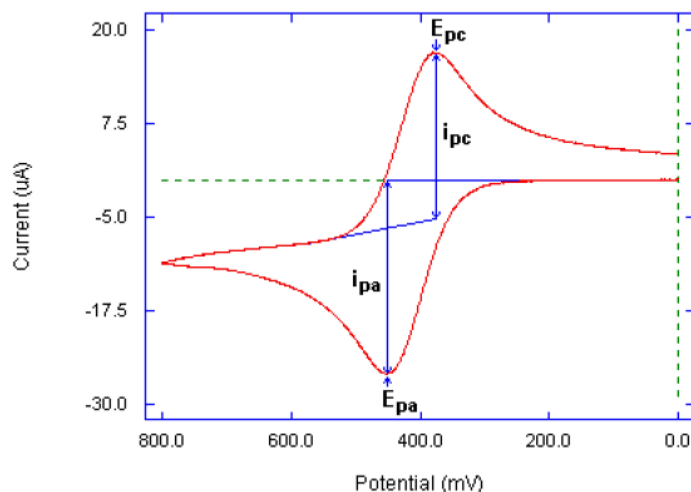
Figure 19: A typical cyclic voltammogram showing the basic peak parameters [138].

The position of both the cathodic and anodic peaks gives thermodynamic information of the redox couple. The anodic and cathodic peak potentials also enable the calculation of the formal electrode potential, $E^{o'}$ as follows:

$$E^{o'} = \frac{E_{pa} + E_{pc}}{2} \tag{19}$$

By decreasing the reversibility, the difference between the two peak potentials increases.

1.7.1.1 Diagnostic criteria to identify a reversible process

An electrode process is defined as electrochemically reversible when the rate of the electron transfer is higher than the rate of the mass transport.

To prove reversibility of the system, the following conditions should hold:

- the ratio of the currents passed at reduction (I_{pc}) and oxidation (I_{pa}) is near unity ($I_{pa} = I_{pc}$ or $I_{pa} / I_{pc} = 1$)

- the peak potentials (E_{pa} and E_{pc}) is independent of the scan rate, v

- the formal potential is positioned midway between E_{pa} and E_{pc}

- the peak current (I_p) is proportional to v.

- the separation between the peak potentials E_{pa} and E_{pc} is 59 mV/n for an n-electron couple at 25 ^{o}C or, $|E_{pa}$-$E_{pc}|$ would be 59 mV for a 1 electron process and 30 mV for a two -electron process.

The maximum current *(i.e.* the current at the potential corresponding to the maximum of the peak) for a planar electrode is expressed by:

$$I_p = 0.4463 n FAC_o \left(\frac{nF}{RT} \right)^{1/2} D^{1/2} v^{1/2} \tag{20}$$

Where n is the number of electrons transferred; F is the Faraday's constant; A is the electrode area; C_o is the bulk concentration; R is the gas constant; D is the diffusion coefficient and v is the speed at which the potential is scanned. At 25 ºC, equation (20) becomes:

$$I_p = 2.69 \times 10^5 \, n^{3/2} \, A^{1/2} \, D^{1/2} \, v^{1/2} C_o \qquad (21)$$

Equation (21) is known as the Randles-Sevčik equation. From the equation, if a plot of I_p vs. $v^{1/2}$ yields a straight line which passes through the origin, such a process is said to be diffusion controlled and the value of D can be calculated from the slope.

When plotted, the log of peak current versus the log of scan rate gives a linear plot whose slope distinguishes between diffusion controlled peaks, adsorption controlled peaks or even a mixture of the two. When a slope of 0.5 is obtained, it implies a diffusion controlled peak and a slope of 1 is for an adsorption peak. Moreover, when an intermediate value of the slope (0.5-1) is obtained, the suggested mechanism is mixed (diffusion-adsorption) [139].

CV can also be used to evaluate the interfacial behaviour of electroactive compounds. Both the reactant and the product can be involved in an adsorption –desorption process. Such interfacial behaviour can occur in studies of numerous organic compounds, as well as of metal complexes (if the ligand is specifically adsorbed) [140]. In some cases, the sample to be characterized may be immobilised onto the surface of a working electrode (chemically modified electrodes). In such a case, the surface concentration (Γ) of the adsorbed species could be estimated from a plot of current (I_p) versus scan rate (v) in accordance with the Brown Anson model using the equation [140-141]:

$$I_p = \frac{n^2 F^2 \Gamma A v}{4RT} \qquad (22)$$

56

During the reduction or adsorption of the adsorbed layer, the quantity of the charge (Q) consumed can also be used to calculate the surface coverage or surface concentration (Γ) [140]:

$$Q = nFA\,\Gamma \tag{23}$$

-where Q is the charge in Coulomb (C) and (Γ) is the surface coverage in mol/cm^2.

1.7.1.2 Diagnostic criteria to identify an irreversible process

The most important characteristic of a cyclic voltammogram of a totally irreversible system is the total absence of a reverse peak. For totally irreversible systems, the peak potential shifts with the scan rate. In addition, the individual peaks are reduced in size and widely separated as shown in Figure 20 (Curve c). Such processes are characterised by sluggish electron transfer.
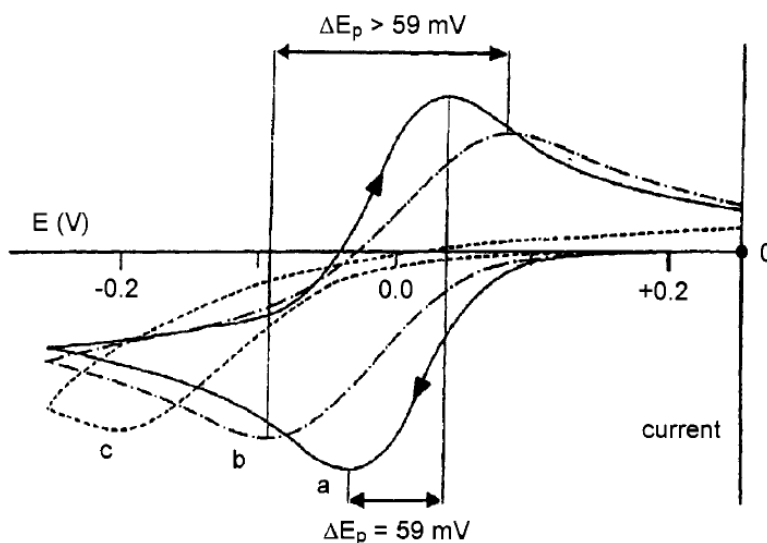
Figure 20: Qualitative behaviour of the cyclic voltammetric profiles for a reduction process having features of (a) reversibility; (b) quasi reversibility; (c) irreversibility [141].

57

The following conditions are required to identify whether an electrochemical process is irreversible:

- there is no reverse peak

- I_{pa} or I_{pc} is proportional to $v^{1/2}$

- the value of E_p shifts - $30/\alpha n$ for each decade increase in v

- $|E_p - E_{p/2}| = 48/\alpha n$ mV

The dependence of peak potential with scan rate for an irreversible process is expressed in the following equation [140]:

$$E_p = E^{o'} - \frac{RT}{\alpha nF}\left[0.78 - \ln\left(\frac{k^o}{D^{1/2}}\right)\right] + \ln\left(\frac{\alpha nFv}{RT}\right)^{1/2} \tag{24}$$

Where k^o is heterogeneous rate constant and α is the transfer coefficient

Thus, E_p occurs at higher potentials than $E^{o'}$ when the over-potential depends on k^o and α. In a case where E_p is independent of k^o, the shift of the peak potential could be compensated by an appropriate change of the scan rate. Therefore, when αn decreases, the voltammogram could become more drawn out. Equation 24 also allows for the calculation of the heterogeneous rate constant, k^o, if the values of $E^{o'}$ and D are known.

The peak current for an irreversible process is given by:

$$I_p = (2.99 \text{ x } 10^5)n(\alpha n)^{1/2}AC_oD^{1/2}v^{1/2} \tag{25}$$

For the irreversible process, the peak current (I_p) is proportional to the bulk concentration (C_o) but can be lower in value depending on the value of the transfer coefficient (α). The chemical meaning of an irreversible electrochemical process implies that a large activation

barrier to the electron transfer takes place causing breakage of the original molecular frame with the formation of new species [141].

1.7.1.3 Diagnostic criteria to identify a quasi-reversible process

It is common that in electron transfer processes one observes that at low scan rates, the process behaves reversibly, whereas at high scan rates the process behaves irreversibly (such behaviour is more easily seen for processes that are not complicated by coupled reactions). Processes occurring in the transition zone between reversible and irreversible behaviour are called quasi reversible. A quasi reversible process occurs when the rate of the electron transfer $Ox + ne^- \rightarrow Red$ is of the same order of magnitude as the mass transport. A typical cyclic voltammogram for a quasi-reversible process is shown in Figure 20 (Curve b). A quasi-reversible process is characterised by determining either the thermodynamic parameter $E^{o\prime}$ (formal potential) or the kinetic parameters, α (transfer coefficient) and k^o (rate constant) [141].

For a quasi-reversible system, the following conditions should hold:

- $|I_p|$ increases with $v^{1/2}$ but is not proportional to it

- $I_{pa} = I_{pc}$ or $I_{pa}/I_{pc} = 1$ provided $\alpha_c = \alpha_a = 0.5$

- ΔE_p is greater than 59/n mV and increases with increasing v

- E_{pc} shifts negatively with increasing v.

The current for a quasi-reversible process (with $10^{-1} > k^{\circ} > 10^{-5}$ cm/s) is controlled by both charge transfer and mass transport. In such a case, the shape of the CV is a function of

$\dfrac{k^{\circ}}{\sqrt{\pi \alpha D}}$ and $\alpha = \dfrac{nFv}{RT}$. When the values of $\dfrac{k^{\circ}}{\sqrt{\pi \alpha D}}$ increase, the quasi-reversible process approaches the reversible system and when its values decreases (i.e., at very fast scan rate) an irreversible process behaviour is observed. Compared to reversible systems, cyclic voltammograms of a quasi-reversible system are more drawn-out and have a larger peak potential separation [140]. Furthermore, the chemical meaning of a quasi-reversible electrochemical process suggests that some important structural reorganisation accompanies the redox step, but it does not allow the molecular framework to undergo fragmentation [141].

The equilibrium potential for the intercalation processes:

$$xLi^{+} + xe^{-} + nC \rightarrow Li_xC_n \tag{26}$$

Where x, the degree of intercalation, is given by the Nernst equation:

$$E = E^0 + \frac{RT}{F} \ln \frac{[Ox]}{[Red]} \tag{27}$$

-in which during lithium ion reversible insertion in the guest structure, the reduction of the guest species occurs. Equation 27 corresponds to [142]:

$$E(x) = E^0 + \frac{RT}{F} \ln \frac{x}{1-x} \tag{28}$$

For slow scan rate cyclic voltammetry (SSCV), the obtained voltammograms reflect steady-state conditions, and can be used to describe intercalation curves; x vs. E (by integration of

the current measured at each potential) (Figure 21) or to evaluate the Coulombic efficiency of intercalation systems by comparing the integrated areas.
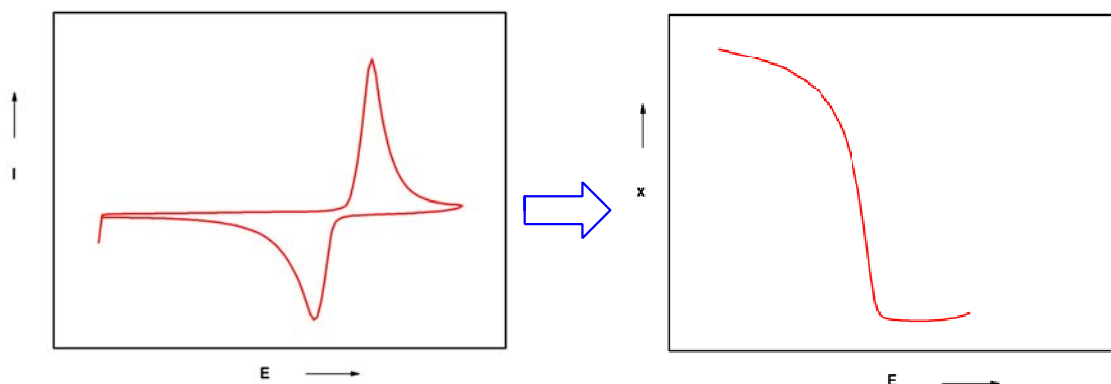
Figure 21: Example of cyclic voltammogram and the corresponding intercalation curve**.**

1.7.2 Electrochemical impedance spectroscopy (EIS)

An electrochemical reaction at the electrode– electrolyte interface cannot be fully understood only by using traditional electrochemical measurements. Those methods provide only currents made of Faradaic and non-Faradaic components. A complete description requires impedance measurements made over a broad frequency range at various potentials. EIS is an excellent, non-destructive, accurate and rapid in-situ technique for examining processes occurring at electrode surfaces. The technique involves superimposing a small sinusoidal (AC) voltage (or current) signal of known amplitude and frequency (the perturbation) to an electrochemical cell at a steady bias potential (or current) and monitoring the AC amplitude and phase response of the cell. The AC perturbation is typically applied over a wide range of frequencies, hence the name impedance spectroscopy. This is in contrast to the usual spectroscopic techniques where interactions of electromagnetic waves and materials are measured. The response to an applied sinusoidal potential excitation is an AC current signal,

(or potential or another signal of interest) which can be analysed as a sum of sinusoidal functions (a Fourier series). The ratio and the phase-relation between the AC voltage and current signal response is the complex impedance $Z(j\omega)$ of the system which permits analysis of electrode process in relation to diffusion, kinetics, double layer, coupled homogeneous reactions, etc. Electrochemical Impedance is normally measured using a small excitation signal. This is done so that the cell response is pseudo-linear. In a linear (or pseudo-linear) system, the current response to a sinusoidal potential will be a sinusoid at the same frequency but shifted in phase as shown in Figure 22:
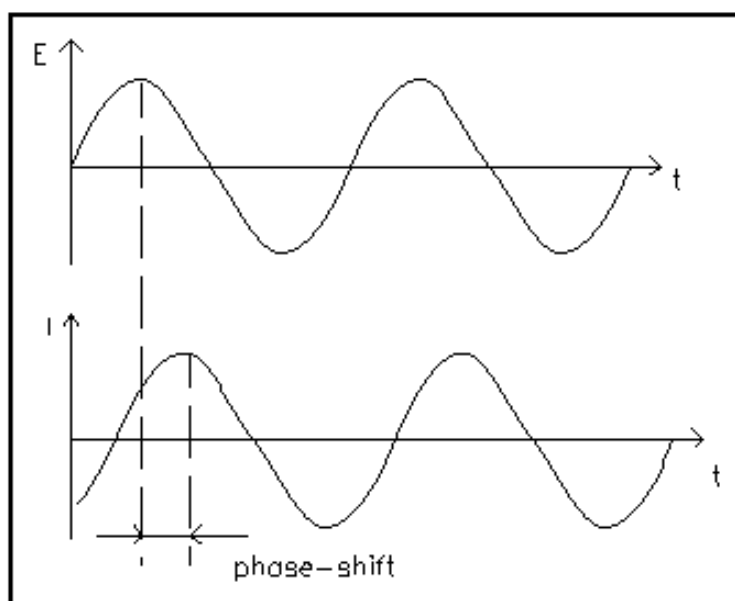
Figure 22: Sinusoidal current response in a linear system.

In traditional Electroanalytical techniques, an applied potential is either constant (potentiostatic) or changing (potentiodynamic) when ramped at a constant rate (v) of $V = dE/dt$. However, in impedance, a small perturbing potential is applied across a cell or sample that changes in a cyclic sinusoidal manner and generates a current resulting from the overpotential (η) caused by the difference of the potential from the equilibrium value. Over a

time period, the average over potential is zero. Because the potential is only perturbing, it has the advantage of minimising the concentration change within the cell or sample after the experiment. The induced current alternates because the voltage changes in a cyclic manner, and hence the term alternating current (AC). The term impedance is therefore a measure of the ability of a circuit to resist the flow of an alternating current (AC). It is synonymous to resistance (R) used in direct current (DC). The ratio of the applied voltage (E) to measured current (I) is the impedance of the system ($Z = E/I$). Since an AC potential is applied to the cell, there will probably be a phase shift by an angle (φ) between the applied AC potential waveform and the AC current response.

The excitation signal, expressed as a function of time, has the form:

$$E_t = E_0 \sin (\omega t) \tag{29}$$

E_t is the potential at the time t, E_0 is the amplitude of the signal, and ω is the angular frequency. The relationship between angular frequency ω (expressed in radians/second) and frequency f (expressed in hertz) is:

$$\omega = 2\,\pi f \tag{30}$$

In a linear system, the response signal, I_t, is shifted in phase (φ) and has different amplitude:

$$I_t = I_0 \sin (\omega t + \varphi) \tag{31}$$

Since the analysis of impedance spectra involves complex numbers, the in-phase and out-of phase impedances are often referred to as real and imaginary impedances. The complex impedance (Z) is made up of a resistive or real part Z', attributable to resistors (in phase with the applied voltage), and a reactive or imaginary part Z'', attributable to the contributions of capacitors (out of phase with the applied voltage by $\pi/2$) and /or inductors (out of phase with

the applied voltage by -π/2). The impedance is related to the resistance (R), reactance (X) and capacitance (C) by the equation:

$$Z = R - jX \tag{32}$$

$$X = 1/\omega C \tag{33}$$

The notation, Z, denotes the complete impedance, which has two components, real (Z') and imaginary (Z''). They are related by the equation:

$$Z = Z' - jZ'' \tag{34}$$

$$j = \sqrt{-1} \tag{35}$$

By considering a pure resistor that does not have any capacitance, its resistance when determined with a continuous current (DC) is R because its impedance is frequency independent. Hence we can write that:

$$Z = Z' = R \tag{36}$$

For an electric circuit or an electrochemical system, the transfer function from the potential

(Input function) to the current (output function) is called the admittance (Y) of the system which is the inverse of impedance:

$$Y = 1/z \tag{37}$$

An expression analogous to Ohm's Law allows the calculation of the impedance of the system as:

$$Z = \frac{E_t}{I_t} = \frac{E_0 \sin(\omega t)}{I_0 \sin(\omega t + \varphi)} = Z_0 \left(\frac{\sin(\omega t)}{\sin(\omega t + \varphi)} \right) \tag{38}$$

The impedance is therefore expressed in terms of a magnitude, Z_0, and a phase shift, φ. With the Euler's relationship,

$$\exp(j\alpha) = \cos\alpha + j\sin\alpha \qquad (39)$$

-it is possible to express the impedance as a complex function whereby the potential is described as:

$$E_t = E_0 \exp(j\omega t) \qquad (40)$$

And the current response as:

$$I_t = I_0 \exp(j\omega t + \varphi) \qquad (41)$$

The impedance is then represented as a complex number:

$$Z(\omega) = \left(\frac{E}{I}\right) = Z_0 \exp(-j\varphi) = Z_0(\cos\varphi - j\sin\varphi) \qquad (42)$$

1.7.2.1 Graphical representations of EIS data

(a) The Nyquist plot

This is a plot of the imaginary part of Z (ImZ) vs. the real part of (ReZ). The impedance can be represented as a vector (arrow) of length |Z|. The angle between this vector and the x-axis is f (= arg Z). A typical Nyquist plot is as shown in Figure 23:
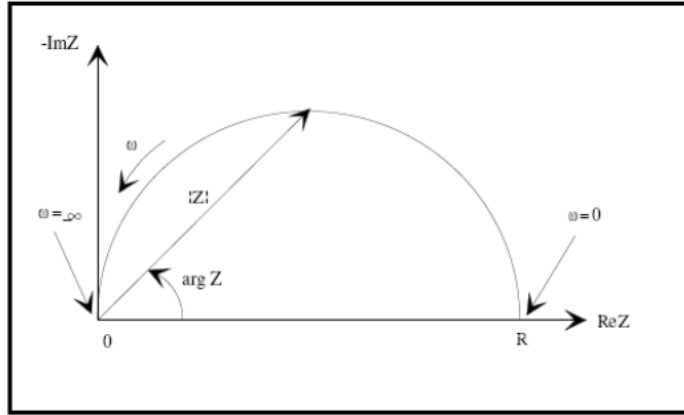
Figure 23: A typical Nyquist plot [143].

(b) The Bode diagram

This is a plot of the logarithm of the magnitude of impedance and phase angle versus the logarithm of frequency. The magnitude of impedance, $|Z|$ measured in Ohms (Ω), is given by:

$$|Z| = \sqrt{Z'^2 + Z''^2} \tag{43}$$

Impedance data are well resolved at all frequencies in a Bode plot as shown in Figure 24:
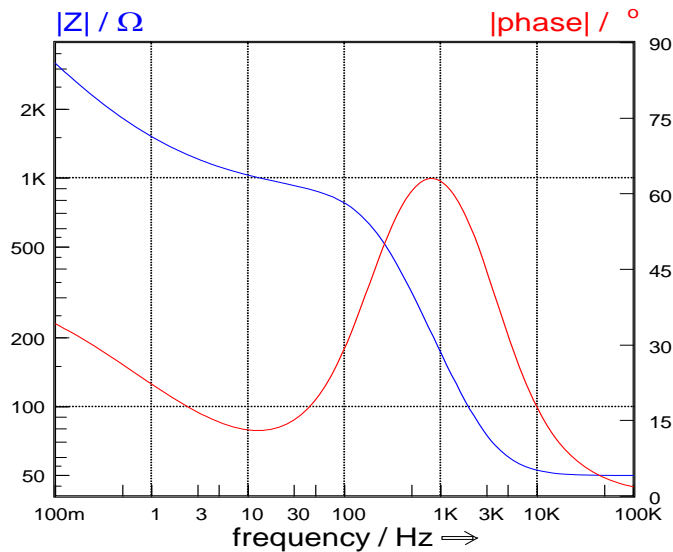
Figure 24: A typical Bode plot [143].

66

EIS data are commonly analysed by fitting them to an equivalent electrical circuit model. An equivalent circuit is an electrical circuit that, at any frequency, is able to give the same electrical response to an electrical AC-stimulus as the electrochemical system under examination. This means that the electrochemical system can be described in terms of real or complex circuit elements as resistors, capacitors or inductors (more generally in terms of complex impedances) and distributed elements such as constant phase element and Warburg impedance. To be useful, the elements in the model should have a basis in the physical electrochemistry of the system. As an example, most models contain a resistor that models the cell solution resistance.

Table 8 shows the common circuit elements and their current – voltage and impedance relationships:

Table 8: Common circuit elements.

Circuit element	Current vs. voltage	Impedance
Resistor	$E = IR$	$Z = R$
Inductor	$E = L\, dI/dt$	$Z = j\,\omega\,L$
Capacitor	$I = C\, dE/dt$	$Z = 1/j\,\omega\,C$

The impedance of a resistor is independent of frequency and has no imaginary component. With only a real impedance component, the current through a resistor stays in phase with the voltage across the resistor. The impedance of a capacitor is a function of frequency and has only an imaginary part. A capacitor's impedance decreases as frequency increases. The

impedance versus frequency behaviour of a capacitor is opposite to that of an inductor. As a result, the current through a capacitor is phase shifted -90° with respect to the voltage. Inductors have only an imaginary impedance component. The current through an inductor is phase shifted 90° with respect to the voltage. The impedance of an inductor increases as frequency increases.

In order to develop an equivalent circuit, the circuit elements can be arranged in series and parallel connections. A common circuit used for impedance data modelling is the Randles equivalent circuit as shown in Figure 25:
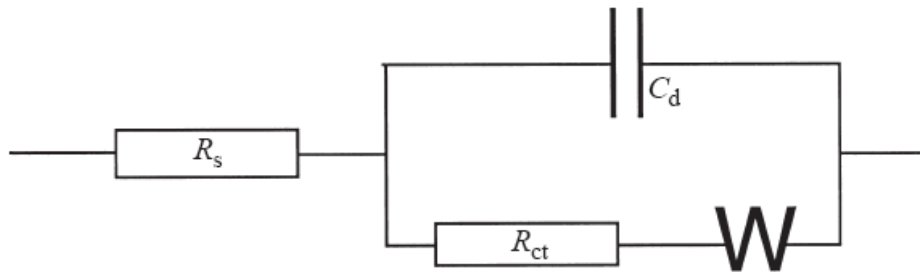
Figure 25: The Randles equivalent circuit in series with the solution resistance.

1.7.2.2 Physical electrochemistry and electrical circuit elements

The contributions to the resistance of a cell are the solution resistance (R_s), the charge transfer resistance (R_{ct}) and Warburg impedance (Z_w) while contribution to the capacitance could be as a capacitor (C) and constant phase element (CPE).

(a) Solution resistance (R_s)

The solution resistance is the resistance between the working electrode and the reference electrode. This is indicated as a small offset on the real impedance axis. Its measurement is taken at the high frequency intercept close to the origin of the Nyquist plot. The resistance of an ionic solution depends on the ionic concentration and type of ions present in the electrolyte, temperature and the geometry of the area in which current is carried. In addition, the solution resistance arises from the finite conductance of the ions in bulk solution. In a bound space, with area A and length l, carrying a uniform current, the resistance is defined as:

$$R_s = \rho \frac{l}{A} \qquad (44)$$

ρ is the solution resistivity. The reciprocal of ρ, (κ), is more commonly used, and it is the conductivity of the solution. Its relationship with solution resistance is:

$$\kappa = \frac{l}{RA} \qquad (45)$$

The unit of κ is Siemens per meter (S/m). The Siemens is the reciprocal of the ohm (1 S = 1/Ohm).

(b) Charge transfer resistance (R_{ct})

The charge transfer resistance is the resistance associated with the charge transfer mechanisms for electrode reactions. It is the resistance to electron transfer at the electrode interface. The charge transfer resistance (R_{ct}) is a manifestation of two effects (1) the potential energy associated with the oxidation or reduction event at the electrode (i.e. the

overpotential) and (2) the energy barrier of the redox species reaching the electrode due to electrostatic repulsion or steric hindrance. It can be deduced from the kinetically controlled electrochemical reaction at low over-potentials. From the Butler-Volmer equation which is the principal equation of electrochemical kinetics [144], the current (I) from the oxidation and reduction reactions is given by:

$$I = I_0 \left(\exp\left(\alpha \frac{nF}{RT} \eta \right) - \exp\left(-(1-\alpha) \right) \frac{nF\eta}{RT} \right) \tag{46}$$

When $nF\eta/RT$ is well below unity, the linearization of the Butler-Volmer equation is necessary to obtain:

$$I = I_0 nF\eta / RT \tag{47}$$

By analogy with Ohm's law [144], and when the over-potential, η, is very small and the electrochemical system is at equilibrium, the equation below is called charge transfer resistance:

$$R_{ct} = \frac{RT}{nFI_0} \tag{48}$$

-where I_0 is the exchange current in Amperes (A) and R_{ct} is charge transfer resistance in ohms (Ω). Thus, the charge transfer impedance is equal to charge transfer resistance, given by the equation below:

$$Z_{Rct} = R_{ct} = \frac{RT}{nFI_0} \tag{49}$$

From this equation the exchange current (I_0) can be calculated when R_{ct} is known. The charge transfer resistance (or charge transfer impedance) is estimated from the diameter of the semicircular region on the real impedance axis of the Nyquist plot. When the chemical

system is kinetically sluggish, the R_{ct} will be very large and may display a limited frequency region where mass transfer is a significant factor. However, if the system is kinetically facile, and the mass transfer always plays a role, the semicircular region is not well formed [145].

(c) Warburg impedance (Z_W)

This is the resistance associated with the diffusion of ions across the electrode/electrolyte interface. In other words, the impedance due to diffusion is called the Warburg-impedance. The impedance depends on the frequency of the potential perturbation. It is associated with the difficulty in mass transport of electroactive species. Layers of ions at the electrode interface behave like RC element (i.e. a resistor and a capacitor in parallel) and this produces an infinite sum of RC elements called the Warburg impedance. The Warburg impedance (Z_w), only of physical importance in Faradaic EIS, represents the delay arising from diffusion of the electroactive species to the electrode [145]. It is only appreciable at low frequencies and is affected by convection. It is characterised as a linear portion at an angle of 45°, and its Nyquist plot is a straight line with a slope of unity and its Bode plot is a straight line having a slope of -0.5 [144, 146]. The equation for the infinite Warburg impedance is given by [144]:

$$Z_w = \frac{\sigma(1-j)}{\sqrt{\omega}}$$ (50)

With σ, the Warburg coefficient defined as:

$$\sigma = \frac{RT}{\sqrt{2}\, n^2 F^2 A} \left(\frac{1}{D_o^{1/2} C_o} + \frac{1}{D_r^{1/2} C_r} \right)$$ (51)

-where, ω is the angular frequency, D_o is the diffusion coefficient of the oxidant, D_r is the diffusion coefficient of the reductant, A is the surface area of the electrode, n is the number of

electrons involved, C_o is the concentration of oxidant at the electrode surface, C_r is the concentration of reductant at the electrode surface, F is the Faradays constant, T is the temperature and R is the gas constant.

(e) Double layer capacitance

The capacitance, (C) is defined as the ability of an electrochemical system to store or retain Charge [145-146]. An electrical double layer exists at the interface between an electrode and its surrounding electrolyte. This double layer is formed as ions from the solution "stick on" the electrode surface and electronic carriers (electrons or holes) of the opposite sign accumulate at the electrode side of the interface. Charges in the electrode are separated from ions charges by the electrode/electrolyte interface. The separation is very small, often on the order of angstroms. Charges separated by an insulator form a capacitor. The value of the double layer capacitance depends on many variables. Electrode potential, temperature, ionic concentrations, types of ions, oxide layers, electrode roughness, impurity adsorption, etc. are all factors.

The electrical double layer is the array of charged particles and/or oriented dipoles that exists at all materials interface. In electrochemistry, double layer reflects the ionic zones formed in the solution to compensate for the excess of charge on the electrode [140]. When an electrode is polarized relative to the solution, it attracts ions of opposite charge. This tendency is countered by the randomising thermal motion of the ions, but resulting in a local build-up of excess ions of opposite charge. Thus, any electric field arising at the electrode or within ionic solution decays exponentially because the excess ions screen the field. The characteristic

length of this decay or Debye length is proportional to the square root of ion concentration [145] (about1 nm for biological ionic strengths). This effect creates a capacitance called double layer capacitance or diffuse layer capacitance. Ions adsorbed at bare electrodes increase the capacitance in accordance with the Gouy- Chapman-Stern model. The double layer capacitance depends on the voltage because an increase in the electrode voltage attracts the diffuse ion layer, therefore increasing capacitance. If an insulator (e.g. an insulating probe layer) covers the electrode, forming a capacitance, the double layer capacitance appears in series with it. Thus, measurement of the double layer capacitance can provide valuable insights into adsorption and desorption processes, as well as into the structure of the film-modified electrodes.

(F) Constant phase element (CPE)

Capacitors in EIS experiments often do not behave ideally. Instead they act like a constant phase element. The impedance of a CPE is given by:

$$Z_{CPE} = \frac{1}{j\omega Q_o} = \frac{1}{j\omega C} \tag{52}$$

1.8 Rationale

Various attempts have been made in the past to improve the conductivity and electrochemical properties of $LiFePO_4$ cathode. Many researchers have suggested solutions such as: coating with a conductive layer around the particles [147]; ionic substitution to enhance the electrochemical properties [148-150]; and synthesis of particles with well-defined morphology [151]. Li *et al.* [152] demonstrated that $LiFePO_4$/MWCNTs composite cathode

73

displayed an initial discharge capacity of 155 mAh/g at 0.1 C rates and a gradual decrease in discharge capacity upon cycling. Whittingham *et al*. [153] indicated that the added MWCNTs in pure $LiFePO_4$ enhanced the electronic conductivity of the final product. Sakamoto and Dunn [154] incorporated single walled carbon nanotubes (SWNT) as a conductive additive in V_2O_5 aerogels. The V_2O_5/SWNTs composite electrode retained high specific capacity at high discharge rate. Zaghib *et al*. [5] reported the electrochemical performance of natural graphite-fibres/polyethylene oxide (PEO)-based gel electrolyte/$LiFePO_4$ batteries. Huang and Goodenough [125] showed that significantly improved capacity and rate capability can be achieved in $LiFePO_4$/polymer composite cathodes.

It can be seen from the above that attempts have been made to improve the electrochemical properties and conductivity of $LiFePO_4$ cathode. However, to the best of my knowledge, $LiFePO_4$/carbon nanotubes/polyaniline composite cathodes (with the carbon nanotubes previously functionalised with inorganic nanocrystals of iron-cobalt alloy nanoparticles have not been synthesized. Iron-cobalt alloy nanoparticles due to their porous structure provide viable routes for the facile transfer of electrons during lithium ion deinsertion/insertion in a 3-D nanonetwork that is formed between the carbon nanotubes and adjacent $LiFePO_4$ particles. It is expected that the iron-cobalt derivatised carbon nanotubes, in combination with polyaniline conducting polymer, will bring about synergistic effects in the electrochemical properties and performance of lithium iron phosphate cathode in a lithium ion cell.

1.9 Aim and objectives

The aim of this research work is therefore to develop novel lithium ion cathode systems with enhanced electrochemical properties that will fit the characteristics (high capacity, safety and low cost) required in modern lithium ion batteries for applications not only in portable

electronics but also in zero or controlled emission vehicles, so as to curb the environmental challenges and threats posed by CO_2 emissions from fossil fuel in internal combustion engines. Accordingly, this thesis focused on the following objectives:

(i) Preparation and microscopic analysis of nanocrystal alloys of iron-cobalt (FeCo) and carbon nanotubes (CNTs).

(ii) Preparation and microscopic analysis of nanocrystal alloys of iron-cobalt and their CNTs composites (FeCoCNT).

(iii) Preparation of FeCoCNT/polyaniline composites (FeCoCNT-PA).

(iv) Assembly of pristine $LiFePO_4$ and $LiFePO_4$/FeCoCNT-PA composites battery coin cells and the determination of their voltammetric, impedimetric and charge/discharge properties.

Chapter 2

Methodology

2.1 Instrumentation

Cyclic voltammetry (CV), electrochemical impedance spectroscopy (EIS) and charge/discharge studies were carried out using crimp-sealed LIR 2032 laboratory coin cells. CV and EIS measurements were conducted on Zahner IM6ex (Germany) Electrochemical Workstation. A Potential range of: 2.3 - 4. 0 V and 0.1- 0.8 mV/s scan rates were used for CV while EIS measurements were recorded at a formal potential of 3.4 V and perturbation amplitude of 5 mV within the frequency range of 100 mHz – 100 KHz. Charge/discharge data were recorded from MTI 8 Channels Battery Analyser between 3.0 - 4.0 V at 0.1 C rates. The surface morphology and size distribution of the nanomaterials were examined through SEM and TEM images obtained from JEOL JSM-7500F Scanning Electron Microscope (US) and Tecnai G2 F20X-Twin MAT 200 kV Field Emission Transmission Electron Microscope (FEI, Eindhoven, Netherlands). Coin cells were assembled in an argon-filled LAB STAR MBRAUN glove box in which the oxygen and water contents were maintained below 1 ppm. All potentials were measured against Li/Li^+.

2.2 Reagents and materials

Iron (II) sulfate heptahydrate ($FeSO_4.7H_2O$), cobalt (II) chloride hexahydrate ($CoCl_2.6H_2O$), sodium borohydride ($NaBH_4$, 98%), triethylamine ($C_6H_{15}N$, 99.5%), trisodiumcitrate dihydrate ($Na_3C_6H_5O_7.2H_2O$, 99%), ethanol (C_2H_6O, absolute), acetone (C_3H_6O, 99.8 %), aniline ($C_6H_5NH_2$, 99%), poly(4-styrenesulfonic acid, 18% w/v aqueous solution), ammonium persulfate (($NH_4)_2S_2O_8$), nitric acid (HNO_3, 65%), N-methyl-2-pyrrolidone,

lithium ribbon (0.75 mm thick, 45 mm wide, 99.9%) were all purchased from Sigma-Aldrich. Sulfuric acid (H_2SO_4, 98%) was purchased from Kimix; hydrochloric acid (HCl, 37%) was purchased from Fluka; poly(vinylidene fluoride), carbon black, $LiFePO_4$ powder, 1 M stock electrolyte solution of $LiPF_6$ in 1:1 v/v ethylene carbonate-dimethyl carbonate, aluminium foil, positive and negative electrode casings, springs, spacers and celgard separators were obtained from MTI Corporation. Home grown carbon nanotubes (CNTs; diameter of 40-200 nm and length up to 20 μm; synthesized according to [155]) were used. Water obtained from a Millipore Milli-Q purification system with resistivity 18.2 MΩ cm, was used to prepare all aqueous solutions. Before use, all the glassware was cleaned with freshly prepared aqua regia (HNO_3: HCl) 1:3, % v/v), rinsed thoroughly with water, and dried.

2.3 Preparation of iron-cobalt (FeCo) bimetallic nanoparticles

Bimetallic FeCo nanoparticles were synthesized by a procedure described previously for Fe-Ni nanoparticles [156] with some modification. 20 mL of 0.05 M aqueous mixture of $FeSO_4.7H_2O$ and $CoCl_2.6H_2O$ in a Fe: Co atomic ratio of 3:2 was stirred, under nitrogen saturation, for 20 min followed by gentle addition of 0.6 g $NaBH_4$. The solution colour changed from brownish pink to black upon addition of $NaBH_4$. After further stirring for 20 min, 2 mL of 1 M triethylamine was added to stabilize the nanoparticles. Stirring was continued for an additional 20 min and followed by vacuum filtration through 0.2 μm Nylon 6.6 membrane filter paper. To get rid of the excess borohydride, the particles were washed with copious amounts of water and rinsed with ethanol and acetone, in that order. The washed particles were vacuum dried overnight at 50 ºC.

2.4 Preparation of FeCo functionalised CNTs

CNTs were first purified according to the procedure developed by Liu et al [157]. Briefly, 50 mg of CNT was added to 100 mL of an acid mixture of 3:1 concentrated sulphuric acid and concentrated nitric acid. The CNTs were sonicated in a DC 200 H ultrasonic cleaner (mrc) for 8 h. The purified nanotubes were centrifuged using a Mini - Plus Eppendorf: 12-place fixed-angle rotor for 1.5 – 2.0 mL tubes (F-45-12-11) of radius 6 cm at 14100 relative centrifugal force (RCF) and washed with water until the pH tested neutral. The washed CNTs were vacuum dried overnight at 50 °C. Functionalisation of the purified CNTs with FeCo nanoparticles was achieved through the reductive precipitation of metal salts within a CNT suspension according to the modified procedure [158]: 1 mg CNT and 2 mL of 1% sodium citrate (complexant) were added into a 100 mL flask containing 0.05 M aqueous mixture of $FeSO_4.7H_2O$ and $CoCl_2.6H_2O$. The resultant mixture was ultrasonicated for 2 h at room temperature followed by careful addition of 0.6 g $NaBH_4$ and 1 mL of 1 M triethylamine (TEA; stabilizer). This was allowed to stir for 30 min followed by filtration and vacuum drying according to the above procedure for FeCo nanoparticles preparation.

2.5 FeCoCNT/polyaniline composites synthesis

Chemically synthesized FeCoCNT/polyaniline composites were obtained by a simultaneous chemical polymerization of aniline monomer in the presence of acidic suspension of FeCoCNT according to the outline:

Distilled Aniline + FeCoCNT dispersion in 1 M HCl $\xrightarrow[\substack{(NH_4)_2S_2O_8 \\ 0\text{-}5^o\,C\,,\,Stirring}]{+\ \ poly(4\text{-styrenesulfonic acid})}$ FeCoCNT-polyaniline
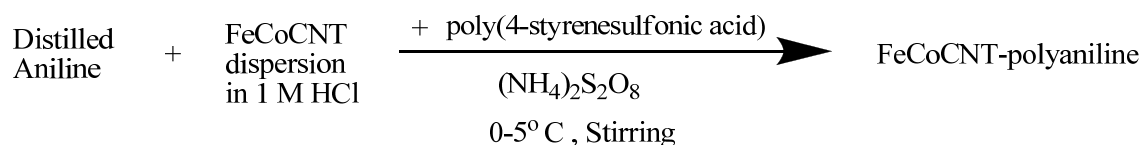
First, 0.05 mg FeCoCNT in 50 mL of 1 M HCl was sonicated for 30 min; then 1 mL distilled aniline monomer and poly (4-styrenesulfonic acid) dopant (monomer to dopant ratio of 4:1) were dissolved in the suspension and stirred magnetically in ice bath for 30 min. 0.5 g of $(NH_4)_2S_2O_8$ that acts as an oxidant was slowly added into the above suspension. The mixture was reacted for 30 min at 0-5 °C. The dark suspension became green which is an indication of the beginning of polymerisation reaction of aniline monomer. Polymerisation was carried out at 0-5 °C for 24 h. The composites were obtained by filtering and rinsing the reaction mixtures several times with distilled water and ethanol, resulting in the conductive emeraldine salt form of FeCoCNT/polyaniline composites. Finally, the dark-green composites were dried at 60 °C for 24 h under vacuum. This composite will be subsequently referred to as FeCoCNT-PA. Pure polyaniline free of FeCoCNT was also polymerized at the same conditions [125, 159].

2.6 Preparation of LiFePO$_4$/10% FeCoCNT-PA composites

The composites were prepared according to a reported procedure [160]. FeCoCNT-PA was dispersed in water under short sonication in ultrasonic bath. To this solution, LiFePO$_4$ powder was added (in a proportion of 10% of FeCoCNT-PA in the mixture) and stirred overnight. The suspension was subsequently evaporated to dryness. Similar procedure was adopted for the preparation of LiFePO$_4$/50% FeCoCNT-PA composites.

Thus, the three active lithium cathode materials used in this thesis include:

(a) LiFePO$_4$/10% FeCoCNT-PA

(b) LiFePO$_4$/50% FeCoCNT-PA

(c) Pristine LiFePO$_4$

2.7 Coin cell assembly

The LIR 2032 coin cells of Li│ LiPF$_6$ (EC: DMC=1:1in volume ratio) │active Li cathode employed in this thesis were assembled according to the following steps: First the working cathode was prepared by mixing 80% of the active material with 10% carbon black and 10% poly (vinylidene fluoride) in N-methyl-2-pyrrolidone. The mixed slurry was spread uniformly on a thin aluminium foil and dried in vacuum at 120 ℃ for 12 h. The coated aluminium foil was roll-pressed and punched out to the required dimension with a punching machine. A metal lithium ribbon (permanently kept in the glove box) was used as anode and punched to the same dimension as the cathode. Together with the other cell components (positive and negative electrode casings, spring, spacer, polypropylene micro-porous film (celgard) separator and the electrolyte), the LIR 2032 coin cells (Figure 26) were assembled in a dry argon-filled glove box and crimp-sealed for further electrochemical studies.
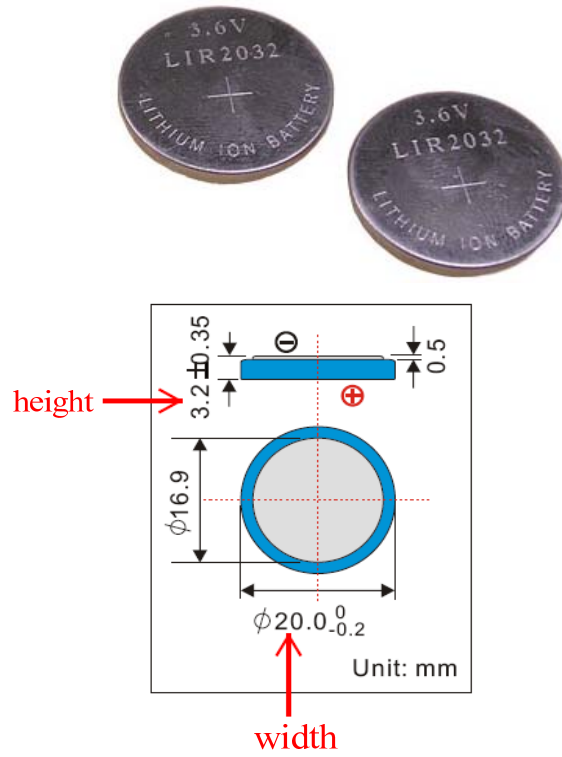
Figure 26: Lithium ion rechargeable (LIR) 2032 coin cells.

Chapter 3

Results and discussions

3.1 Electrochemical studies

The composite LiFePO$_4$ battery coin cells were interrogated by cyclic voltammetry and electrochemical impedance spectroscopy to ascertain the cathode composition with better electrochemical performance.

3.1.1 Cyclic voltammetry

The CV profiles of LiFePO$_4$/10% FeCoCNT-PA and LiFePO$_4$/50% FeCoCNT-PA are shown in Figure 27.
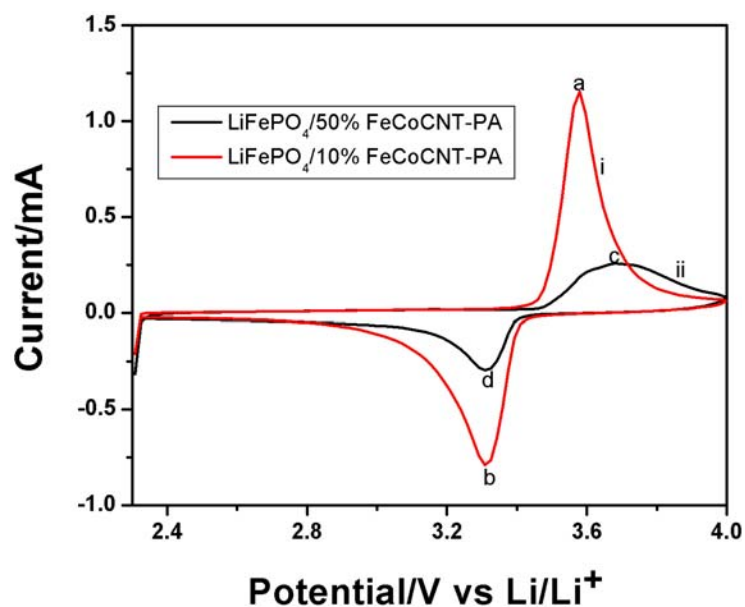
Figure 27: Cyclic voltammograms of (i) LiFePO$_4$/10% FeCoCNT-PA and (ii) LiFePO$_4$/50% FeCoCNT-PA in 1 M LiPF$_6$ containing 1:1 v/v ethylene carbonate – dimethyl carbonate solvent mixture. Scan rate 0.1 mV/s (voltage range: 2.3 – 4.0 V).

The cyclic voltammograms are characterised by a well-defined pair of redox peaks which are associated with the electrochemical lithium ion deinsertion/insertion within the octahedral sites of the $LiFePO_4$ structure upon the two phase oxidation/reduction of Fe^{2+}/Fe^{3+} redox couple [112, 161-162]. However, the shapes of the voltammograms show that the $LiFePO_4$/50% FeCoCNT-PA composite cathode with diminished and broadened peaks revealed more sluggish lithium deinsertion/insertion behaviour. This could be consistent with a pseudo capacitive type phenomenon taking place on the electrode surface [163-164] due to more carbon nanotubes content in this composite than in the 10% composite cathode. The sharp peaks of $LiFePO_4$/10% FeCoCNT-PA composite cathode indicate a more facile lithium ion transfer resulting in better reaction kinetics. Again, the peak to peak separation in $LiFePO_4$/10% FeCoCNT-PA ($\Delta E_p = E_{pa}- E_{pc} = 270$ mV) is less than that of $LiFePO_4$/50% FeCoCNT-PA ($\Delta E_p = 370$ mV) which suggests better electrochemical reversibility in the former than in the latter. The electrochemical deinsertion/insertion of lithium ions into $LiFePO_4$ can be described as:

$$LiFePO_4 \xrightleftharpoons[\text{discharge}]{\text{charge}} Li_{1-x}FePO_4 + xLi^+ + xe^-$$

(53)

Analysis of voltammogram i, which is due to $LiFePO_4$/10% FeCoCNT-PA, gave an anodic peak, a, ($I_{pa} = 1.15$ mA, $E_{pa} = 3.58$ V) and a cathodic peak, b, ($I_{pc} = 0.79$ mA, $E_{pc} = 3.31$ V) at a formal potential, $\Delta E^{0`} = (E_{pa} + E_{pc})/2 = 3.44$ V. This formal potential value has been reported [116, 165] and is synonymous with the potential at the point of inflexion on the flat plateau at 3.45 V, observed during battery cycling experiments (charge/discharge curve) (Section 3.1.7), where lithium deinsertion/insertion occurs as a two-phase process. Peak a, corresponds to the delithiation of $LiFePO_4$ to the charged state of the functioning battery, $FePO_4$. Complete extraction of lithium (when x = 1) according to Equation (53), corresponds to a theoretical specific capacity of 170 mAh/g. It is well known that the electrochemical

deinsertion/insertion mechanism of LiFePO$_4$ electrode in nonaqueous electrolytes has already been established [112]. The corresponding equation for the anodic process (lithium deinsertion) can be written as:

$$\text{LiFePO}_4 - x\text{Li}^+ - xe^- \rightarrow x\text{FePO}_4 + (1\text{-}x)\text{LiFePO}_4 \tag{54}$$
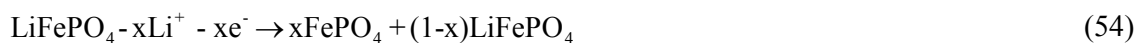
Conversely, peak b arose from the lithiation of the isostructural FePO$_4$ under the electrochemically reducing conditions. The cathodic process (lithium insertion) is governed by the equation [112]:

$$\text{FePO}_4 + x\text{Li}^+ + xe^- \rightarrow x\text{LiFePO}_4 + (1\text{-}x)\text{FePO}_4 \tag{55}$$

Voltammogram ii (Figure 27) showed that the LiFePO$_4$/50% FeCoCNT-PA composite gave an anodic peak at c (I_{pa} = 0.26 mA; E_{pa} = 3.68 V) and a cathodic peak, d, (I_{pc} = 0.29 mA; E_{pc} = 3.31 V) at a formal potential, $\Delta E^{0`}$ = 3.49 V. Peak c corresponds to lithium deinsertion as peak a while peak d involves the insertion of lithium as peak b. The value obtained from the integrated area under the anodic peak at the scan rate of 0.1 mV/s, indicates that the composite LiFePO$_4$/10% FeCoCNT-PA cathode exhibited a charge capacity of 148 mAh/g and a discharge capacity of 134 mAh/g for the insertion of lithium and reduction of Fe^{3+} to Fe^{2+} upon integration of the cathodic peak; thus, giving a charge/discharge reversibility of 91%. The charge capacity corresponds to 87% of the theoretical capacity of LiFePO$_4$ while both capacities were found to be well within the range of reported values using data obtained from cyclic voltammetry [116, 160, 166]; and higher than values obtained for the LiFePO$_4$/50% FeCoCNT-PA composite cathode with charge and discharge capacities calculated to be 86 mAh/g and 73 mAh/g, respectively. The capacities were calculated according to the following steps:

For the 10% cathode composition (Figure 27 (i)), the integration of the anodic peak obtained at 0.1 mV/s (1 x 10^{-4} V/s) scan rate gave the area under the current-potential curve as 1.95 x 10^{-4} Ampere-Volt (AV).

But charge, $Q = \dfrac{\text{Area (AV)}}{\text{Scan rate (V/s)}}$ (56)

Thus $\quad Q = \dfrac{1.95 \text{ x } 10^{-4} \text{ (AV)}}{1 \text{ x } 10^{-4} \text{ (V/s)}}$ (57)

$\Rightarrow \quad Q = 1.95 \text{ As} = 1.95 \text{ Coulombs}$

However, in battery parlance, capacity is calculated in Ampere-hour (Ah). Since 3600 As = 1 Ah,

$\Rightarrow \quad Q = \left(\dfrac{1.95}{3600}\right) \text{Ah}$ (58)

$\Rightarrow \quad Q = 5.42 \text{ x } 10^{-4} \text{ Ah}$ (59)

This Q is the electric charge in Ah which represents the coulometric capacity of the battery. But interest is on the specific capacity of the battery which is defined as the capacity per gram of the active cathode material [11, 125] and is obtained by dividing the coulometric capacity in (Ah) by the mass of the active electrode material. For the 10% composite cathode, mass = 3.672 mg = 3.672 x 10^{-3} g. Therefore the specific capacity becomes:

Specific Capacity $= \dfrac{5.42 \text{ x } 10^{-4} \text{ (Ah)}}{3.672 \text{ x } 10^{-3} \text{ (g)}} = 0.148 \text{ Ah/g}$ (60)

This parameter is usually expressed in mAh/g. Therefore, the specific capacity becomes 0.148 Ah/g x 1000 = 148 mAh/g. The same procedure was adopted for all other capacity calculations with data obtained from cyclic voltammetry.

It is obvious from the foregoing that lithium deinsertion/insertion occurs faster and at a lower onset potential ($\Delta E^{0`}$ values) on LiFePO$_4$/10% FeCoCNT-PA composite electrode. It therefore presents a better electrochemical performance as a lithium ion cathode than the composite LiFePO$_4$/50% FeCoCNT-PA electrode. This observation is consistent with results obtained from electrochemical impedance spectroscopy.

3.1.2 Electrochemical impedance spectroscopy (EIS) (Part 1)

EIS tests were conducted to evaluate the interfacial properties as well as the Li$^+$ migration dynamics of the two composite electrodes. The Nyquist plots are presented in Figure 28.
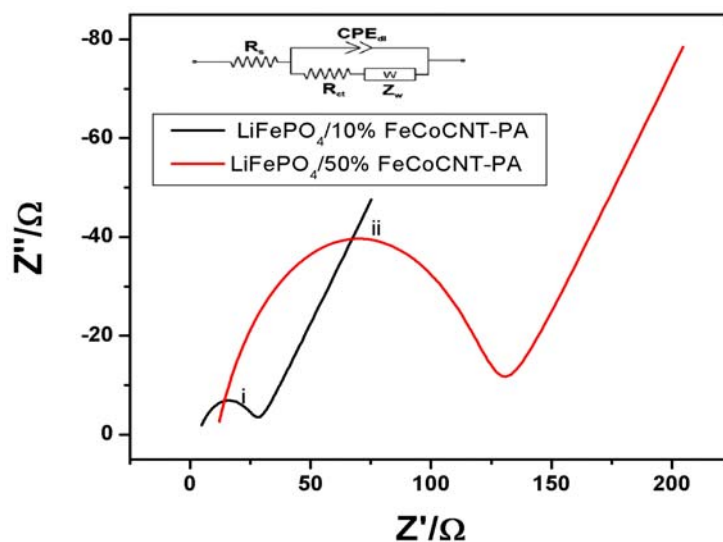
Figure 28: Comparative Nyquist plots of (i) LiFePO$_4$/10% FeCoCNT-PA and (ii) LiFePO$_4$/50% FeCoCNT-PA at formal potential of 3.4 V vs. Li/Li$^+$ and perturbation amplitude of 5 mV.

Each plot gave a well-defined, single semi-circle at high frequency and an inclined line at low frequency attributed to Warburg impedance associated with lithium ion diffusion in the bulk of the electrode, which is an indication that during lithium deinsertion/insertion, the kinetics

of the electrode process is controlled by the diffusion process in the low frequency region and by the charge transfer in the high frequency region [161, 164, 167-168]. The semi-circle attributed to the solid electrolyte interface (SEI) layer [164, 169-170] was not observed. An intercept of the semi-circle with the Z'-axis in the very high frequency region identifies the Ohmic resistance (R_s) of the electrolyte and electrodes. The diameter of the semicircle at high frequency region on the Z'-axis is related to the charge transfer resistance (R_{ct}) which controls the transfer kinetics at the electrode interface. Extrapolation of the semi-circle to lower frequencies gives an intercept corresponding to $R_s + R_{ct}$ from which the value of R_{ct} is determined by subtracting R_s value. Impedance parameters were obtained by fitting from a modified Randles equivalent electrical circuit (inset). CPE is the constant phase element that models the double layer capacitance (C_d) which is due to surface roughness. The time constant (τ); exchange current (I_o) (a measure of the rate of exchange of charge between oxidized and reduced species at any equilibrium potential without net overall change [11]) and heterogeneous rate constant of electron transfer (k_{et}) were calculated according to the equations [145, 171-172]:

$$\tau = \frac{1}{\omega_{max}} \tag{61}$$

$$R_{ct} = \frac{RT}{nFI_0} \tag{62}$$

$$I_0 = nFAk_{et}C \tag{63}$$

$$k_{et} = \frac{I_0}{nFAC} \tag{64}$$

Where, ω_{max} is the angular frequency at maximum impedance; R is the gas constant = 8.314 J/mol K [173]; T is the room temperature = 298 K [173]; n is the number of electrons

transferred per molecule of lithium = 1 [165]; F is Faraday's constant = 96485 C/mol [173]; A is the geometric area of the electrode (16 mm diameter; measured from experiment) = 2.01 cm^2 ; C is the concentration of lithium ion in $LiFePO_4$ = 0.0228 mol/cm^3 [162, 165-166]. The other parameters have their usual meanings. The calculated values are shown in Table 9.

Table 9: Kinetic parameters of $LiFePO_4$/10% FeCoCNT-PA and $LiFePO_4$/50% FeCoCNT-PA obtained from electrochemical impedance spectroscopy at 298 K.

Cathode composition	τ/s rad^{-1}	R_{ct}/Ω	I_0/A	k_{et}/cm s^{-1}	σ/Ω s$^{-1/2}$	D_{app}/cm^2 s^{-1}
10%	6.43 x 10^{-5}	24.57	1.045 x 10^{-3}	2.36 x 10^{-7}	38.41	4.57 x 10^{-14}
50%	2.13 x 10^{-4}	115.7	2.219 x 10^{-4}	5.0 x 10^{-8}	63.62	1.67 x 10^{-14}

The 50% cathode composition exhibited a larger semi-circle with an R_{ct} value that is an order of magnitude higher than that of the 10% composite cathode which is an indication of a kinetically sluggish system. The values of other parameters in the Table point to the fact that facile reaction kinetics occur on the latter as previously confirmed from CV data. Similar phenomenon was reported by Feng, where a composite cathode with 7 wt% multi-walled carbon nanotubes and $LiFePO_4$ showed better electrochemical performance than that with 10 wt% multi-walled carbon nanotubes and $LiFePO_4$ [164].

Generally, the diffusion of lithium ions within the electrodes is the rate-limiting step. The exploitation of the Warburg domain allows determination of the kinetics of this limiting

process through the calculation of the diffusion coefficient, D [161, 174] from the equations [145], where at low frequencies:

$$Z_{re} = R_{\Omega} + R_{ct} + \sigma\omega^{-1/2} \tag{65}$$

$$Z_{im} = \sigma\omega^{-1/2} + 2\sigma^2 C_d \tag{66}$$

Z_{re} is the real impedance $= Z'$; Z_{im} is the imaginary impedance $= Z''$; R_{Ω} is the solution resistance $= R_s$; σ is the Warburg coefficient. The other parameters have their usual meanings.

From Equation (65), a plot of Z_{re} vs. $\omega^{-1/2}$ gives slope $= \sigma$ and intercept $= (R_s + R_{ct})$ as shown in Figures 29 and 30.
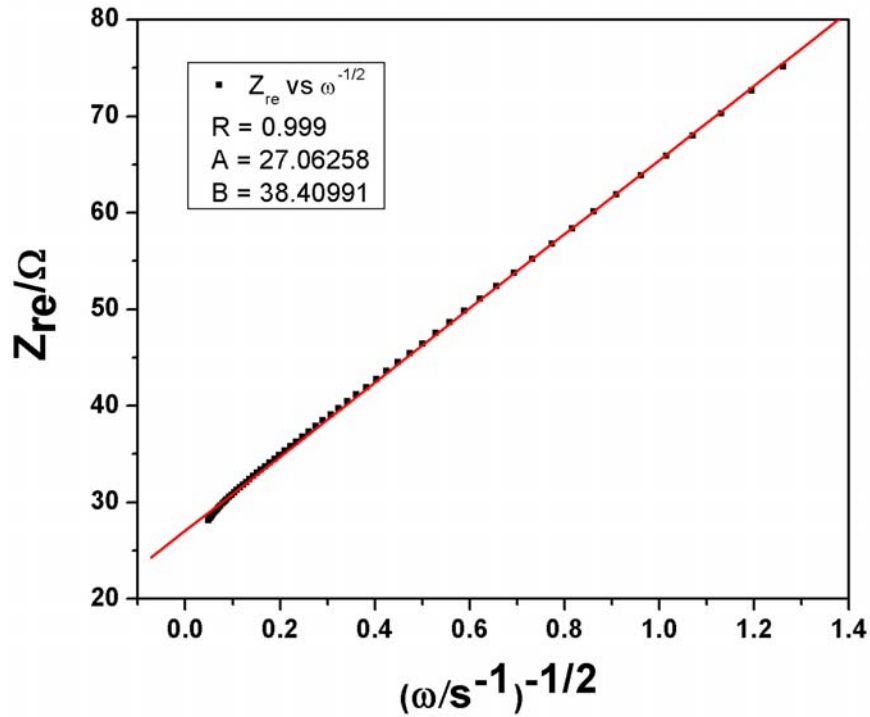
Figure 29: The plot of Z_{re} vs $\omega^{-1/2}$ for composite LiFePO$_4$/10% FeCoCNT-PA cathode.
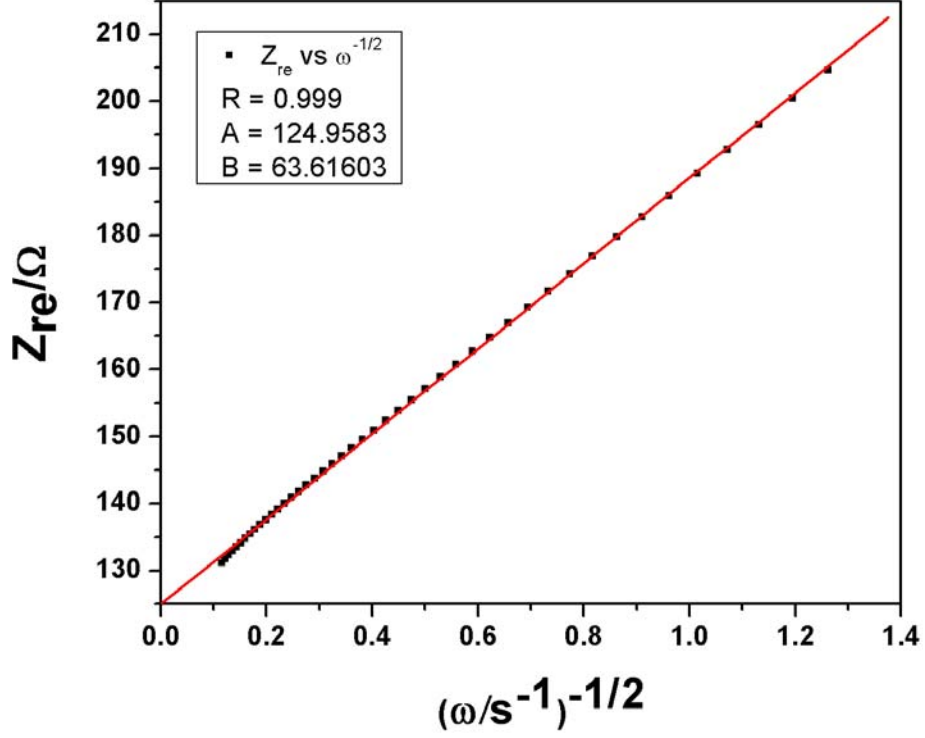
Figure 30: The plot of Z_{re} vs $\omega^{-\frac{1}{2}}$ for composite LiFePO$_4$/50% FeCoCNT-PA cathode.

The straight lines were drawn from the lower frequency region where the Warburg impedance is significant.

σ is defined according to the equation [145]:

$$\sigma = \frac{RT}{\sqrt{2}\, n^2 F^2 A}\left(\frac{1}{D_o^{1/2} C_o} + \frac{1}{D_r^{1/2} C_r}\right) \tag{51}$$

Assuming diffusion coefficients $D_o = D_r = D$ and concentrations $C_o = C_r = C$, Equation (51) can be simplified according to the following steps to obtain an expression for D:

$$\sigma = \frac{RT}{\sqrt{2}\, n^2 F^2 A}\left(\frac{1}{D^{1/2} C} + \frac{1}{D^{1/2} C}\right) \tag{67}$$

$$\sigma = \frac{RT}{\sqrt{2}\ n^2 F^2 A}\left(\frac{1}{\sqrt{D}\ C} + \frac{1}{\sqrt{D}\ C}\right)$$

$$\Rightarrow\ \frac{1}{\sqrt{D}\ C} + \frac{1}{\sqrt{D}\ C} = \frac{\sigma \sqrt{2}\ n^2 F^2 A}{RT} \tag{68}$$

Rationalising the surdic quantities, Equation (68) becomes:

$$\left(\frac{1}{\sqrt{D}} \times \frac{\sqrt{D}}{\sqrt{D}} \times \frac{1}{C}\right) + \left(\frac{1}{\sqrt{D}} \times \frac{\sqrt{D}}{\sqrt{D}} \times \frac{1}{C}\right) = \frac{\sigma \sqrt{2}\ n^2 F^2 A}{RT} \tag{69}$$

$$2\left(\frac{\sqrt{D}}{\left(\sqrt{D}\right)^2} \times \frac{1}{C}\right) = \frac{\sigma \sqrt{2}\ n^2 F^2 A}{RT} \tag{70}$$

But $\left(\sqrt{n}\right)^2 = n$, therefore Equation (70) becomes:

$$\frac{2\sqrt{D}}{DC} = \frac{\sigma \sqrt{2}\ n^2 F^2 A}{RT} \tag{71}$$

Squaring both sides of Equation (71) gives:

$$\left(\frac{2\sqrt{D}}{DC}\right)^2 = \left(\frac{\sigma \sqrt{2}\ n^2 F^2 A}{RT}\right)^2 \tag{72}$$

$$\left(\frac{2^2 D}{D^2 C^2}\right) = \left(\frac{\sigma \sqrt{2}\ n^2 F^2 A}{RT}\right)^2 \tag{73}$$

$$\frac{2^2}{DC^2} = \left(\frac{\sigma \sqrt{2}\ n^2 F^2 A}{RT}\right)^2 \tag{74}$$

$$DC^2 = \frac{2^2 \left(RT\right)^2}{\left(\sqrt{2}\right)^2 \left(\sigma n^2 F^2 A\right)^2} \tag{75}$$

Making D the subject and re-arranging, Equation (75) becomes:

$$D = \frac{2^2 (RT)^2}{2 (\sigma n^2 F^2 AC)^2} \tag{76}$$

$$D = \frac{2 (RT)^2}{(\sigma n^2 F^2 AC)^2} \tag{77}$$

Substituting $\left(\sqrt{2}\right)^2$ for 2, Equation (77) becomes:

$$D = \frac{\left(\sqrt{2}\right)^2 (RT)^2}{(\sigma n^2 F^2 AC)^2} \tag{78}$$

$$D = \frac{\left(\sqrt{2}\, RT\right)^2}{(\sigma n^2 F^2 AC)^2} \tag{79}$$

Equation (79) can be re-written as:

$$D = \left(\frac{\sqrt{2}\, RT}{\sigma n^2 F^2 AC}\right)^2 \tag{80}$$

Due to the initial assumptions, the calculated diffusion coefficients are approximate values and are referred to as apparent diffusion coefficients (D_{app}) as indicated in Table 9 above. It is evident from the Table that the composite with lower value of σ has higher D_{app} value. The calculated D_{app} values are in good agreement with values reported by Prosini et al using similar technique (electrochemical impedance spectroscopy) [123]. The superiority of the LiFePO$_4$/10% FeCoCNT-PA composite cathode over the LiFePO$_4$//50% FeCoCNT-PA cathode is further highlighted by the Bode phase-impedance plots as shown in Figure 31:
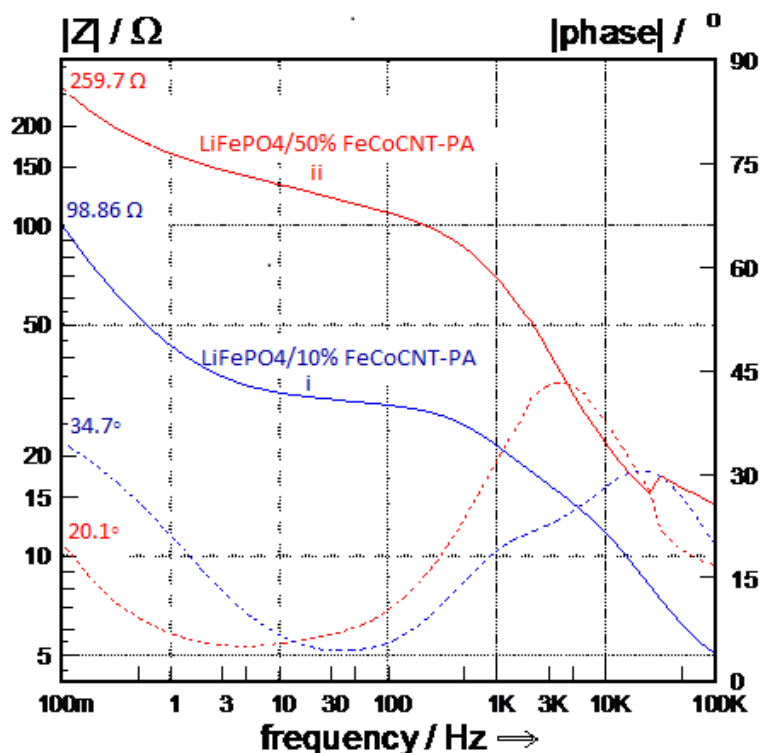
Figure 31: Comparative Bode phase-impedance diagrams of (i) LiFePO$_4$/10% FeCoCNT-PA and (ii) LiFePO$_4$/50% FeCoCNT-PA at 3.4 V vs. Li/Li$^+$ and perturbation amplitude of 5 mV.

At low frequencies (100 mHz), where the electronics of the electrode systems are minimally perturbed and electrochemical equilibrium almost maintained, the LiFePO$_4$/10% FeCoCNT-PA was observed to exhibit lower impedance at 98.86 Ω with higher phase angle at 34.7° which is indicative of better conducting properties and faster kinetics than the LiFePO$_4$/50% FeCoCNT-PA with impedance and phase angle at 259.7 Ω and 20.1°, respectively.

The above diagnostic tests show that the composite LiFePO$_4$/10% FeCoCNT-PA cathode gave better electrochemical reversibility and kinetics towards lithium ion transport within the electrode/electrolyte interface than the LiFePO$_4$/50% FeCoCNT-PA. Hence, detailed analyses on LiFePO$_4$/10% FeCoCNT-PA and comparisons with pristine LiFePO$_4$ are presented in subsequent sections.

3.1.3 Scan rate studies

The cyclic voltammograms of LiFePO$_4$/10% FeCoCNT-PA at different scan rates (0.1 to 0.8 mV/s) are shown in Figure 32.
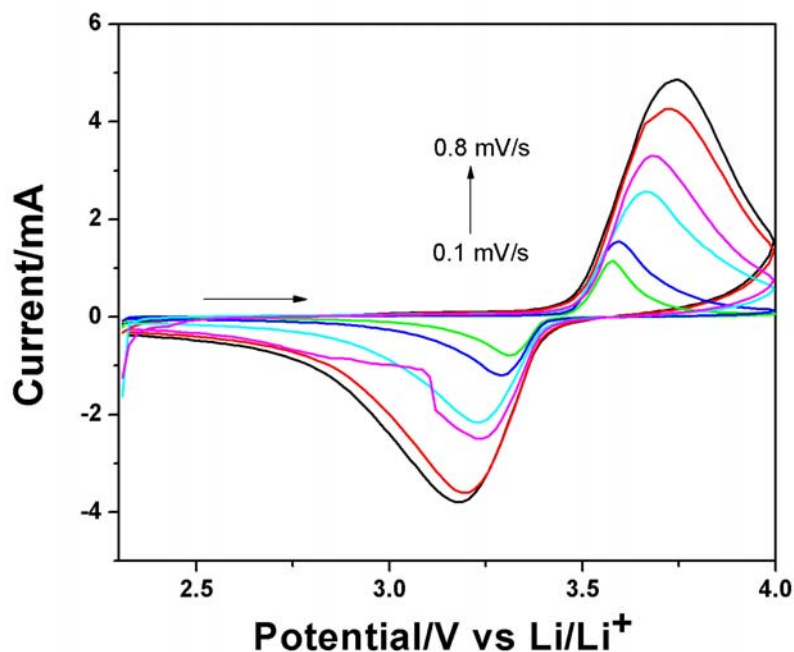
Figure 32: The effect of potential scan rate on the cyclic voltammograms of LiFePO$_4$/10% FeCoCNT-PA in 1 M LiPF$_6$ containing 1:1 v/v ethylene carbonate – dimethyl carbonate solvent mixture between 0.1 – 0.8 mV/s. Voltage range: 2.3 – 4.0 V.

As stated previously (Section 3.1.1), the pairs of peaks, consisting of anodic and cathodic peaks, corresponded to the two-phase charge–discharge reaction of the Fe^{2+}/Fe^{3+} redox couple. These voltammograms indicate that only one electrochemical reaction, corresponding to the peak pairs occurred during the charge and discharge of the composite cathode material. The mean redox potential , $E_{1/2}$ = 3.45 V vs. Li/Li$^+$. Although the wave shapes of the anodic and cathodic peaks were almost symmetrical, the difference between the peak potentials, ΔE_p, was observed to increase with scan rate, v, and calculated to be 421 ± 121 mV which is higher than the 59 mV expected for an ideal Nernstian process; and shows that there are some

kinetic limitations during the electrochemical processes [141, 175]. Such behaviour is attributed to lithium ion interfacial charge transfer as well as other electrochemical processes involved in the diffusion of lithium ions in a solid phase and electron jumping across a poorly or fairly conducting compound [174, 176]. Thus, the ΔE_p, unlike in an ideal reversible condition, is dependent on ν. Moreover, the peak intensities follow the linear law, $I_p = f(\nu)$ (Figure 37) with the ratio of peak currents, (I_{pa}/I_{pc}) calculated to be 1.29 ± 0.1. Furthermore, considering the fact that quasi-reversible electron transfer processes behave reversibly at low scan rates and irreversibly at high scan rates [141] as depicted in Figure 33:
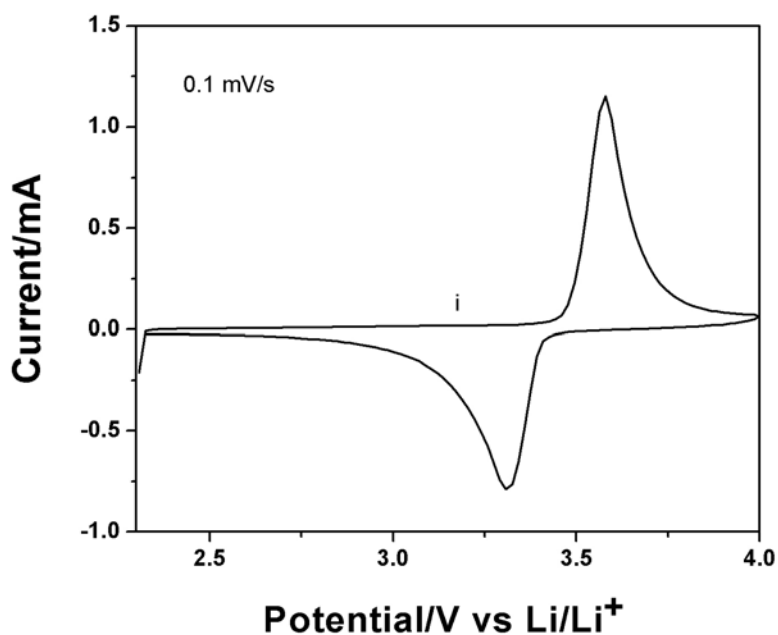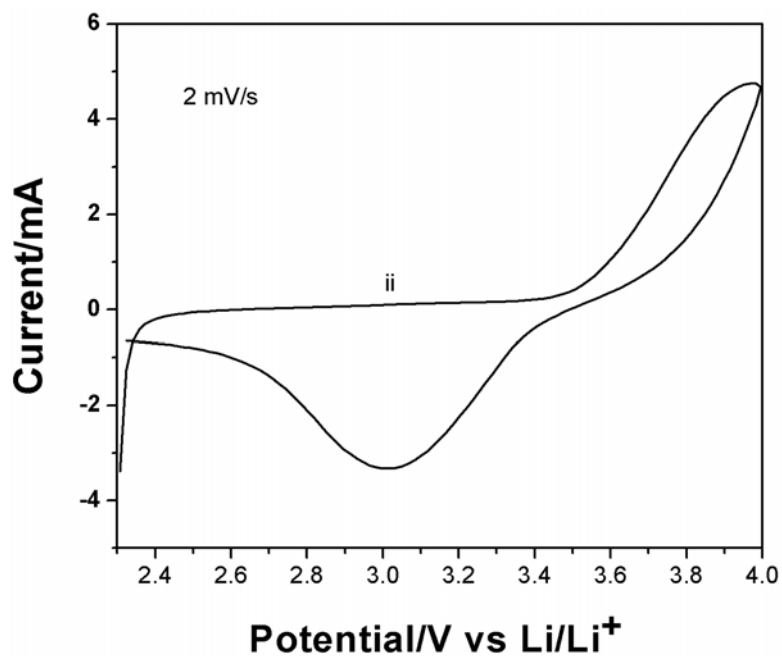
Figure 33: Comparative cyclic voltammograms of LiFePO$_4$/10% FeCoCNT-PA at (i) 0.1 and (ii) 2 mV/s scan rates.

-for 0.1 and 2 mV/s scan rates, it therefore suggests that the Fe^{2+}/Fe^{3+} redox reaction in the LiFePO$_4$/10% FeCoCNT-PA electrochemical system under study is quasi-reversible. This observation was also reported by other researchers [116, 165, 177] and equally observed in the behaviour of the pristine LiFePO$_4$ used in this work (Figure 34). However, the degree of irreversibility is higher in the pristine electrode (ΔE_p = 704 ± 220 mV; formal potential = 3.45 ± 0.004 V; I_{pa}/I_{pc} = 1.3 ± 0.1).
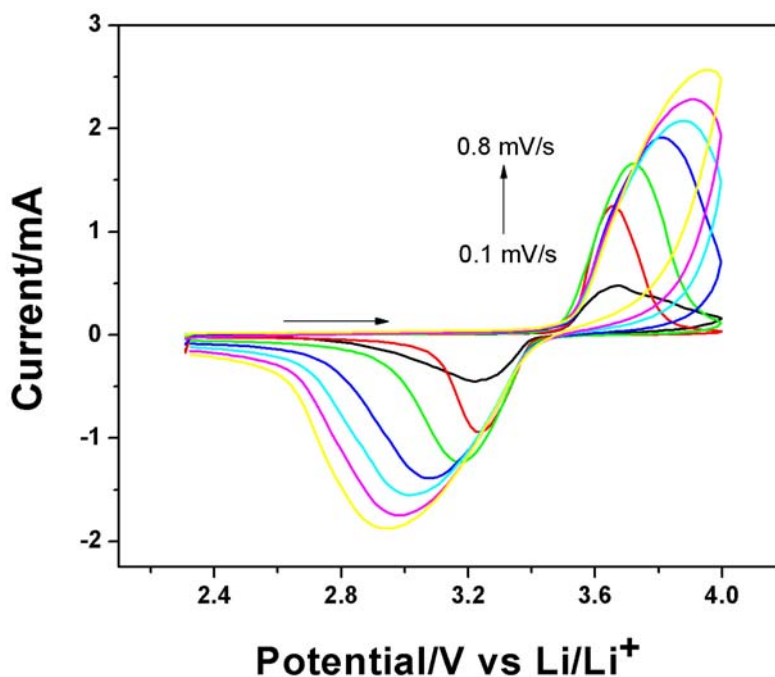
Figure 34: The effect of potential scan rate on the cyclic voltammograms of pristine LiFePO₄ in 1 M LiPF₆ containing 1:1 v/v ethylene carbonate – dimethyl carbonate solvent mixture between 0.1 – 0.8 mV/s. Voltage range: 2.3 – 4.0 V.

The improvement of the composite electrode over the pristine electrode (Figure 35) is ascribed to a synergistic kinetic-effect of the conductive polyaniline and carbon nanotubes additives in the former which enhances its elctrochemical activity. Polyaniline serves as a host for lithium ion intercalation and extraction and provides good electronic contact between the LiFePO₄ particles and the current collector through an overlap of the electrochemically active energies of the conductive polymer and that of the working redox couple of the carbon- coated oxide insertion compound, LiFePO₄ [125]. On the other hand, the nanoscale networking with carbon nanotubes enhances the mobility of electrons between the adjacent LiFePO₄ particles during the lithiation/delithiation process in such a way that the nanotubes interlace adjacent LiFePO₄ nanoparticles together to form a 3D network wiring without blocking the lithium ion transport [178].
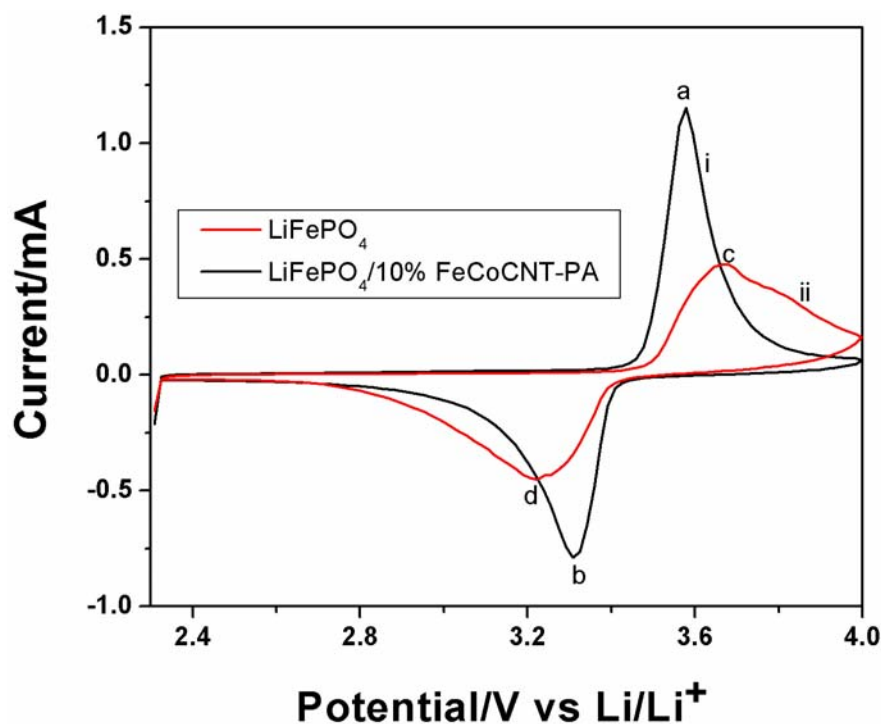
Figure 35: Comparative cyclic voltammograms of (i) LiFePO$_4$/10% FeCoCNT-PA and (ii) pristine LiFePO$_4$ in 1 M LiPF$_6$ containing 1:1 v/v ethylene carbonate − dimethyl carbonate solvent mixture. Scan rate 0.1 mV/s (voltage range: 2.3 – 4.0 V).

The peak notations and descriptions follow similar trends as in the comparisons made between the LiFePO$_4$/10% FeCoCNT-PA and LiFePO$_4$/50% FeCoCNT-PA composite cathodes (Section 3.1.1). The integration of the area under the anodic and cathodic peaks at 0.1 mV/s scan rate gave the values of the anodic charge (Q_a) and cathodic charge (Q_c) to be 1.95 and 1.77; 1.62 and 1.50 Coulombs for the composite and pristine electrodes, respectively; indicating that an almost equal quantity of lithium ions can be reversibly deinserted and inserted. The Q values of the pristine LiFePO$_4$ correspond to charge and discharge capacities of 127 and 117 mAh/g, respectively. The capacity values again show better performance of the composite electrode than the pristine electrode.

Figures 36 and 37 illustrate the scan rate dependence of the peak potentials (E_{pa} and E_{pc}) and peak currents (I_{pa} and I_{pc}) for LiFePO$_4$/10% FeCoCNT-PA. Plots for the pristine electrode are shown in Appendices A and B. From Figure 36, E_{pa} increases while E_{pc} decreases as scan rate increases.

99
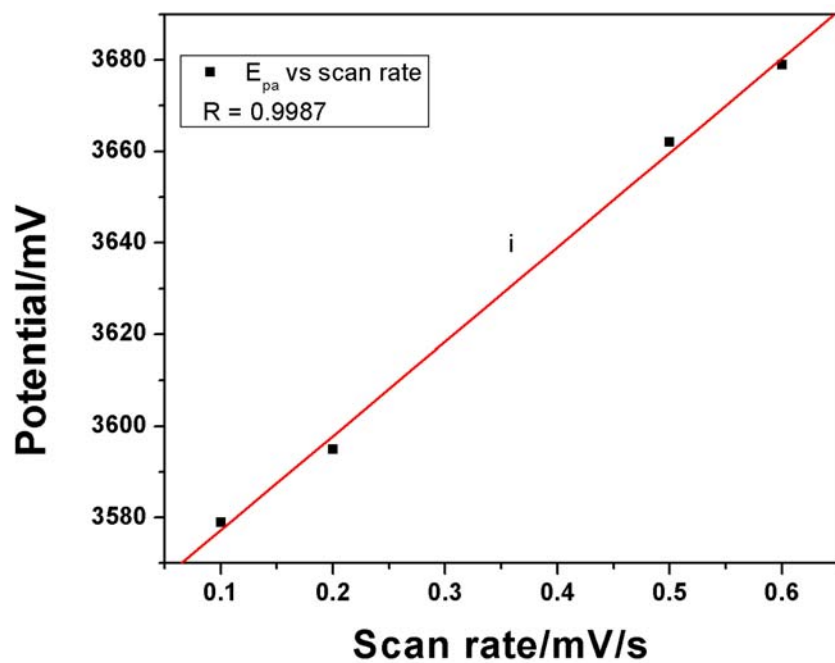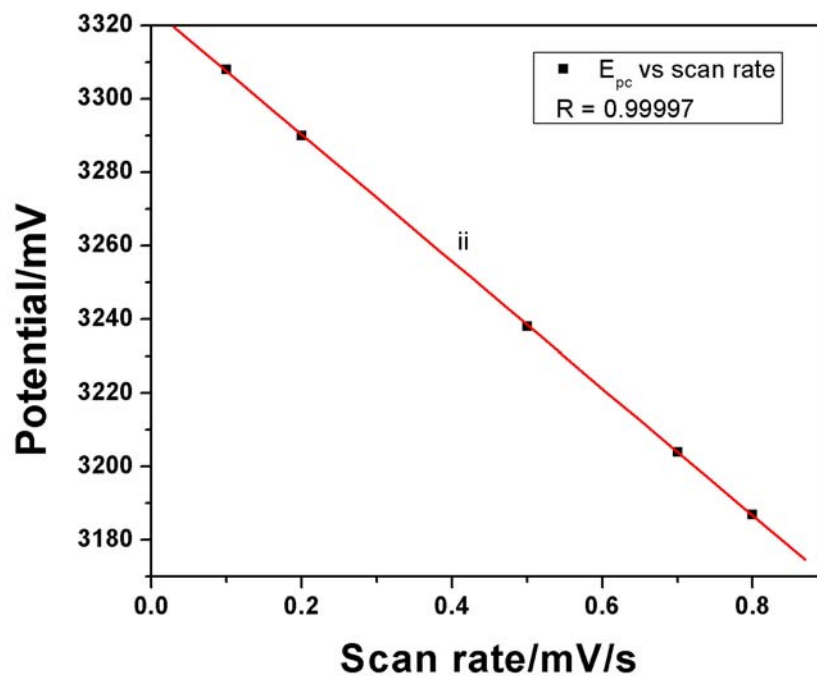
Figure 36: The plots of the (i) anodic peak potential as a function of potential scan rate (ii) cathodic peak potential as a function of potential scan rate for LiFePO$_4$/10% FeCoCNT-PA.
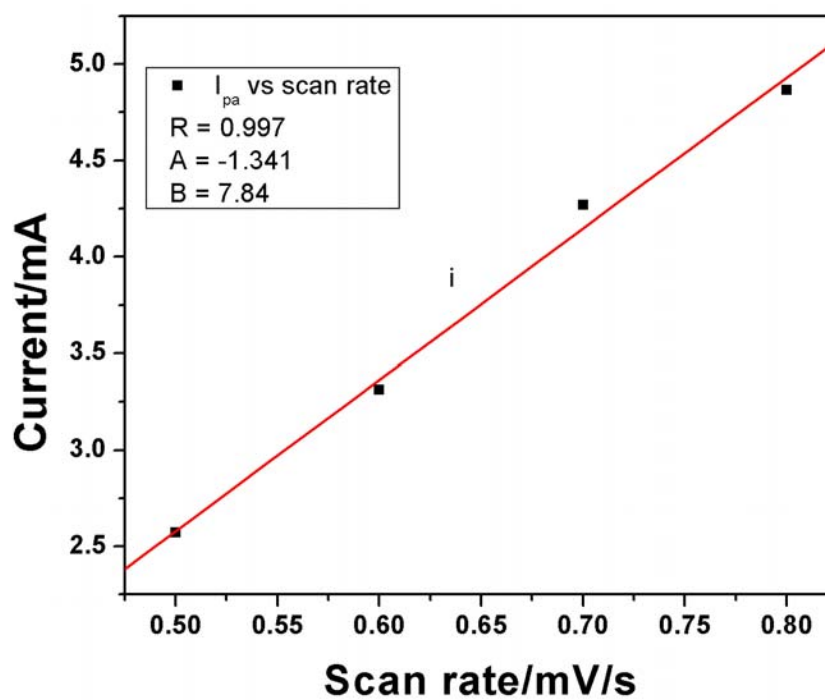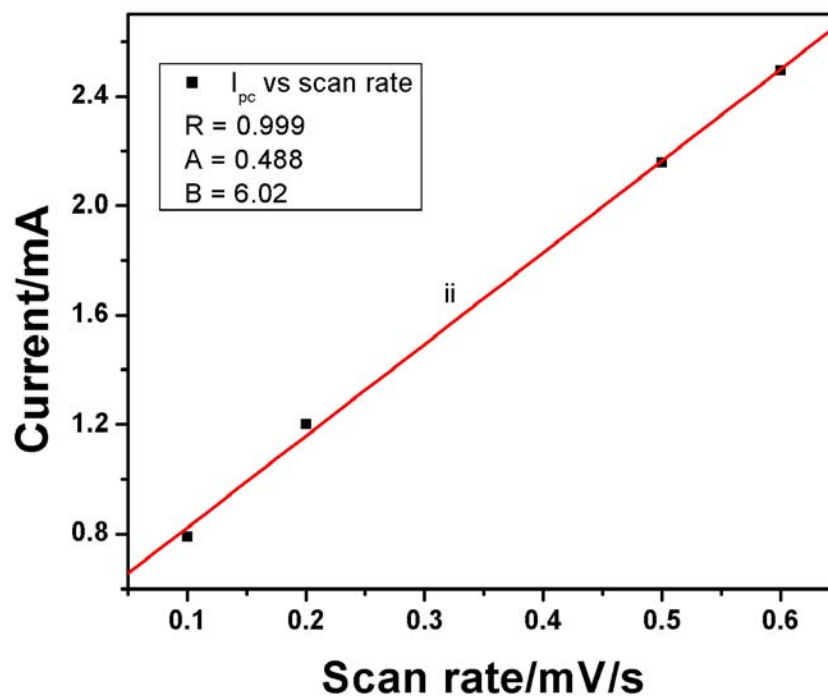
Figure 37: The plots of the (i) anodic peak current as a function of potential scan rate (ii) cathodic peak current as a function of potential scan rate for LiFePO$_4$/10% FeCoCNT-PA.

A linear dependence of peak current on scan rate was observed in the above plots as explained previously.

From the graph, A = intercept; B = slope.

The linear dependence of peak current on the square root of scan rate was also demonstrated in the Randles-Sevcik plot (Figure 38; Equation (21)), for LiFePO$_4$/10% FeCoCNT-PA. Plots for the pristine LiFePO$_4$ are shown in Appendix C.
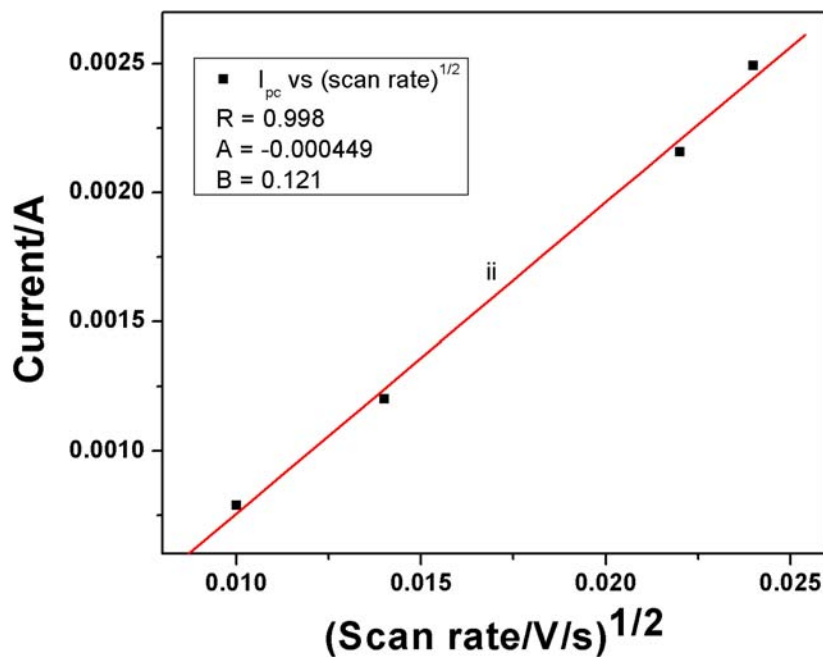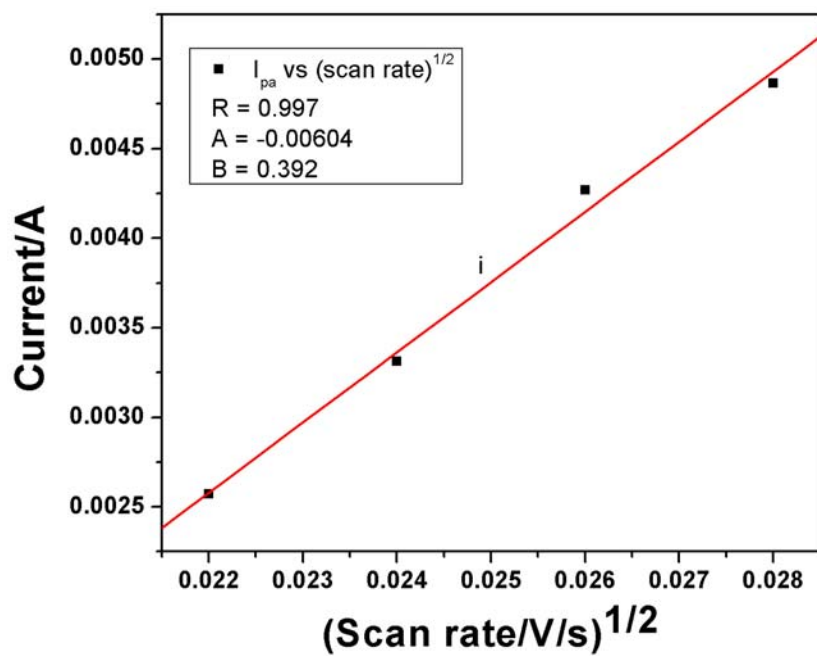
Figure 38: The plots of the dependence of (i) anodic peak current and (ii) cathodic peak current on the square root of potential scan rate for LiFePO$_4$/10% FeCoCNT-PA.

The non-zero intercepts observed are due to the contributions of non-Faradaic currents. This linearity is a confirmation of a diffusion-controlled electron transfer process. In order to shed light on the fact that the diffusion of lithium on the electrode surface is the rate- limiting step, log-log plots of peak current versus scan rate [139] (Figure 39) were studied.
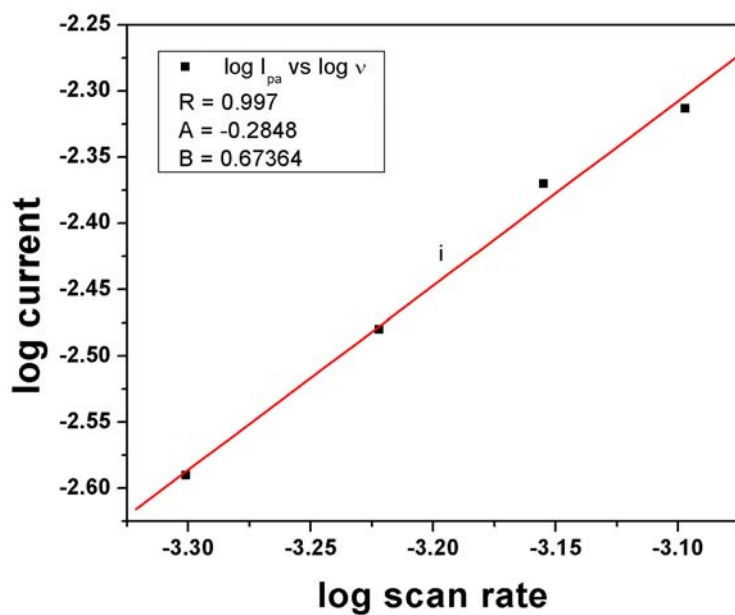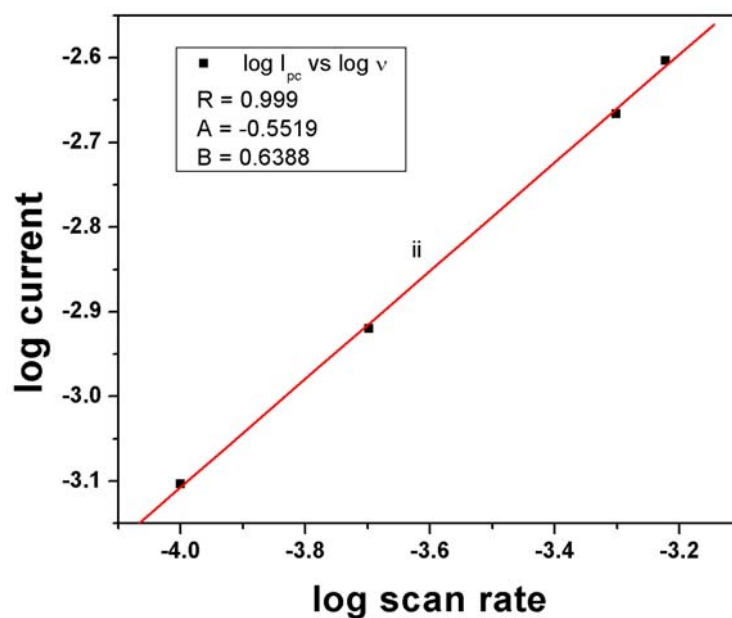
Figure 39: The plots of log of (i) anodic peak current and (ii) cathodic peak current vs. log scan rate for LiFePO$_4$/10% FeCoCNT-PA.

The plots show that peak currents increased linearly with log of scan rate according to the equations: $\log I_{pa} = 0.67364 \times \log v - 0.2848$; $\log I_{pc} = 0.6388 \times \log v - 0.5519$. It is well known that the slope of such log-log plots is 0.5 if diffusion is the rate–limiting process [139]. The slight deviations from this value as observed from the equations is however, as a result of the contributions of adsorption processes at the metal/electrolyte interface due to the presence of the Fe/Co bimetallic nanoparticles that were used to functionalize the nanotubes; and charging of electronically conducting polymers as a result of polyaniline film on the electrode surface [123, 179-180]. Hence, the Fe^{2+}/Fe^{3+} redox process upon deinsertion/insertion of lithium in the composite LiFePO$_4$/10% FeCoCNT-PA cathode was largely due to diffusion. To buttress this point, log-log plots of the pristine LiFePO$_4$ (Figures 40 and 41) gave slopes that were approximately = 0.5, according to the equations: $\log I_{pa} = 0.47122 \times \log v - 1.14908$; $\log I_{pc} = 0.46501 \times \log v - 1.29805$; indicating the absence of adsorption processes emanating from the conductive additives.
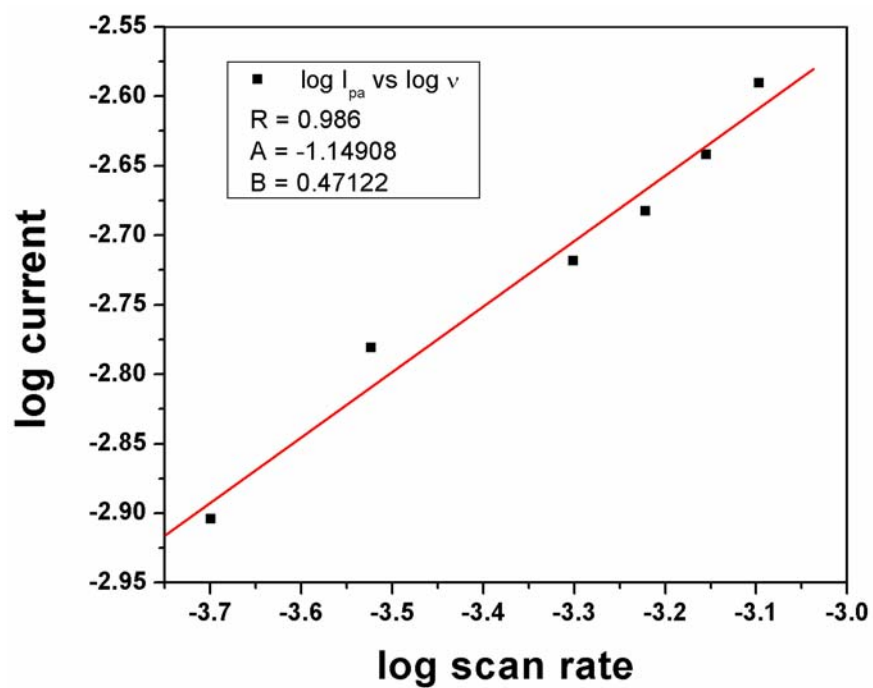
Figure 40: The plot of log of anodic peak current vs. log scan rate for pristine LiFePO$_4$.
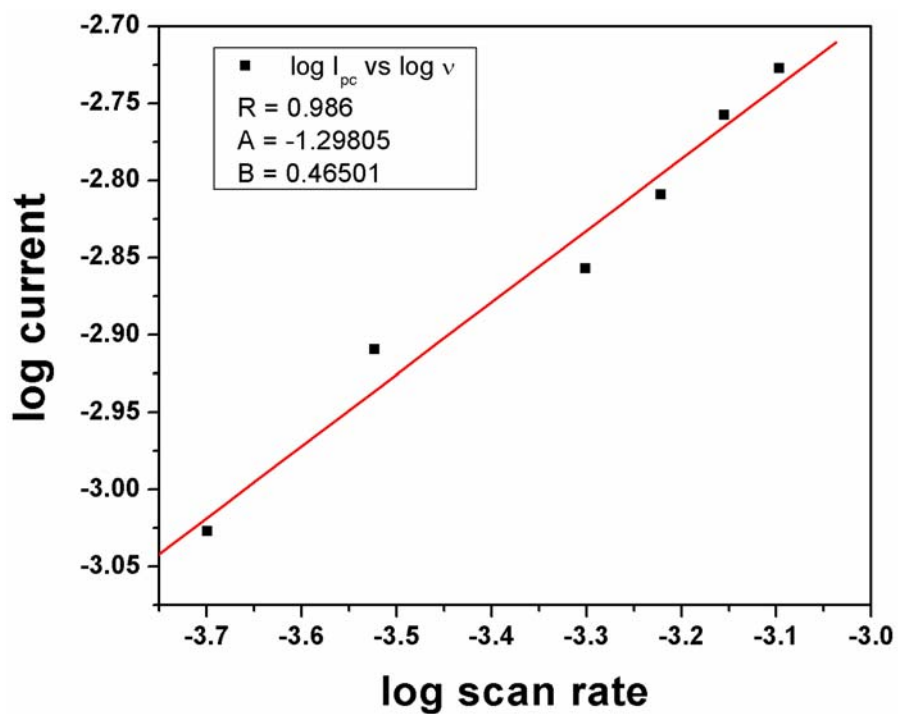
Figure 41: The plot of log of cathodic peak current vs. log scan rate for pristine LiFePO$_4$.

According to the Randles-Sevcik equation [146]:

$$I_p = (2.69 \, x 10^5) \, n^{3/2} \, A \, D^{1/2} \, C \, v^{1/2} \tag{21}$$

The diffusion coefficient, D, calculated from Equation (21) and Figure 38 (i), was found to be 1×10^{-9} cm^2/s and is consistent with those measured by Liu et al [181] for carbon coated composite LiFePO4 but about four orders of magnitude higher than values reported by Franger et al for raw LiFePO$_4$ [161]; and two orders of magnitude higher than the pristine LiFePO$_4$ used in this work (Appendix C (i)) which was calculated to be 4.81×10^{-11} cm^2/s. This difference is ascribed to the synergistic kinetic effects of the conductive additives in the composite cathode as discussed previously. The value is also about four orders of magnitude higher than that obtained from electrochemical impedance spectroscopy in this study. Liu et al equally observed this phenomenon [181-182]. Shaju et al reported similar observations in Li$_{2/3}$(Ni$_{1/3}$Mn$_{2/3}$) O$_2$ cathode systems [167]. The difference in measurements between the two different techniques could be ascribed to the complicated model fittings in EIS together with the various assumptions made in the calculation of D_{app} as discussed earlier on.

3.1.4 Kinetic studies

The redox properties of the pristine and composite electrodes were further interrogated by determining the rate constant of the electron transfer process in the rate-limiting step. The standard rate constant, k_s of an uncomplicated quasi-reversible electrochemical reaction and the scan rate, v, are governed by the Nicholson's equation [183]:

$$\Psi = k_s \left[\pi D n v F / (RT) \right]^{-1/2} \tag{81}$$

Where Ψ is the charge transfer parameter. The other parameters have their usual meanings. Equation (81) is applicable when (ΔE_p x n) values do not exceed 212 mV and under such conditions, the least value of the dimensionless parameter, Ψ that could be obtained is 0.1

[183-184]. Therefore, when the measured ΔE_p values lie outside the range of Ψ values of the Nicholson's treatment, the Klingler and Kochi equation [185] can be used to calculate k_s from CV curves:

$$k_s = 2.18 \left(\frac{D\beta nFv}{RT} \right)^{1/2} \exp\left(-\frac{\beta^2 nF}{RT}(E_{pa} - E_{pc}) \right) \tag{82}$$

Where β is the transfer coefficient (or the symmetry factor) for the electrode process and is equal to α. The transfer coefficient determines what fraction of the electric energy resulting from the displacement of the potential from the equilibrium value affects the rate of electrochemical transformation [11]; $E_{pa} - E_{pc} = \Delta E_p$.

Re-writing Equation (82),

$$k_s = 2.18 \left(\frac{D\alpha nFv}{RT} \right)^{1/2} \exp\left(-\frac{\alpha^2 nF}{RT}(\Delta E_p) \right) \tag{83}$$

Re-writing Equation (83),

$$\Rightarrow \frac{k_s}{2.18 \left(\dfrac{D\alpha nFv}{RT} \right)^{1/2}} = e^{-\left(\frac{\alpha^2 nF}{RT}(\Delta E_p) \right)} \tag{84}$$

Taking natural log of both sides, Equation (84) becomes,

$$\log_e \left(\frac{k_s}{2.18 \left(\dfrac{D\alpha nFv}{RT} \right)^{1/2}} \right) = \log_e e^{-\left(\frac{\alpha^2 nF}{RT}(\Delta E_p) \right)} \tag{85}$$

But $\log_e(x) = \ln(x)$ and $\log_e e = 1$; therefore, Equation (85) becomes:

$$\ln\left(\frac{k_s}{2.18\left(\frac{D\alpha nF\nu}{RT}\right)^{1/2}}\right) = -\frac{\alpha^2 nF}{RT}(\Delta E_p) \tag{86}$$

But $\ln\left(\frac{M}{N}\right) = \ln(M) - \ln(N)$, re-writing Equation 86,

$$\Rightarrow \ln(k_s) - \ln\left(2.18\left(\frac{D\alpha nF\nu}{RT}\right)^{1/2}\right) = -\frac{\alpha^2 nF}{RT}(\Delta E_p) \tag{87}$$

Re-writing Equation (87),

$$\Rightarrow \ln(k_s) - \ln\left(2.18\left(\frac{D\alpha nF}{RT}\right)^{1/2}\right) - \ln(\nu^{1/2}) = -\frac{\alpha^2 nF}{RT}(\Delta E_p) \tag{88}$$

Making $\ln(\nu)^{1/2}$ the subject, Equation (88) becomes:

$$\ln(\nu^{1/2}) = \ln\left(\frac{k_s}{2.18\left(\frac{D\alpha nF}{RT}\right)^{1/2}}\right) + \frac{\alpha^2 nF}{RT}(\Delta E_p) \tag{89}$$

Re-arranging, Equation (89) becomes:

$$\ln(\nu^{1/2}) = \left(\frac{\alpha^2 nF}{RT}\right)(\Delta E_p) + \ln\left(\frac{k_s}{2.18\left(\frac{D\alpha nF}{RT}\right)^{1/2}}\right) \tag{90}$$

Equation (90) is now of the form: $y = mx + c$;

$\Rightarrow$ That a plot of $\ln(\nu^{1/2})$ vs. ΔE_p gives slope $= \left(\frac{\alpha^2 nF}{RT}\right)$ and intercept $= \ln\left(\frac{k_s}{2.18\left(\frac{D\alpha nF}{RT}\right)^{1/2}}\right)$.

108

Thus, k_s can be calculated from the intercept according to the following steps:

$$\text{Intercept} = \log_e \left(\frac{k_s}{2.18 \left(\frac{D\alpha nF}{RT} \right)^{1/2}} \right) \tag{91}$$

Taking exponent of both sides, Equation (91) becomes,

$$e^{\text{Intercept}} = \log_e e^{\left(\frac{k_s}{2.18\left(\frac{D\alpha nF}{RT} \right)^{1/2}} \right)} \tag{92}$$

But $\log_e e = 1$, therefore Equation (92) becomes:

$$e^{\text{Intercept}} = \left(\frac{k_s}{2.18 \left(\frac{D\alpha nF}{RT} \right)^{1/2}} \right) \tag{93}$$

$$\therefore k_s = \left(2.18 \left(\frac{D\alpha nF}{RT} \right)^{1/2} \right) x \left(e^{\text{Intercept}} \right) \tag{94}$$

Plots of $\ln\left(v^{1/2}\right)$ vs. ΔE_p are shown in Figures 42 and 43 for the composite and pristine electrodes:
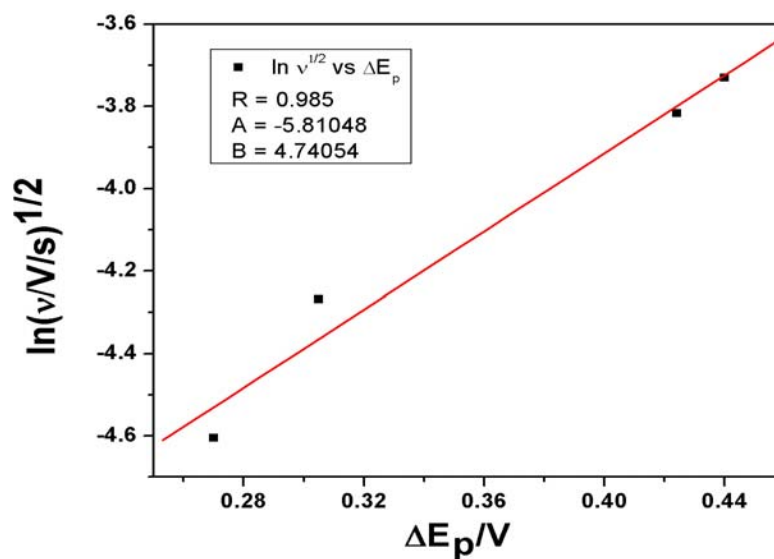
Figure 42: The plot of $\ln\left(v^{1/2}\right)$ vs. ΔE_p for composite LiFePO$_4$/10% FeCoCNT-PA.
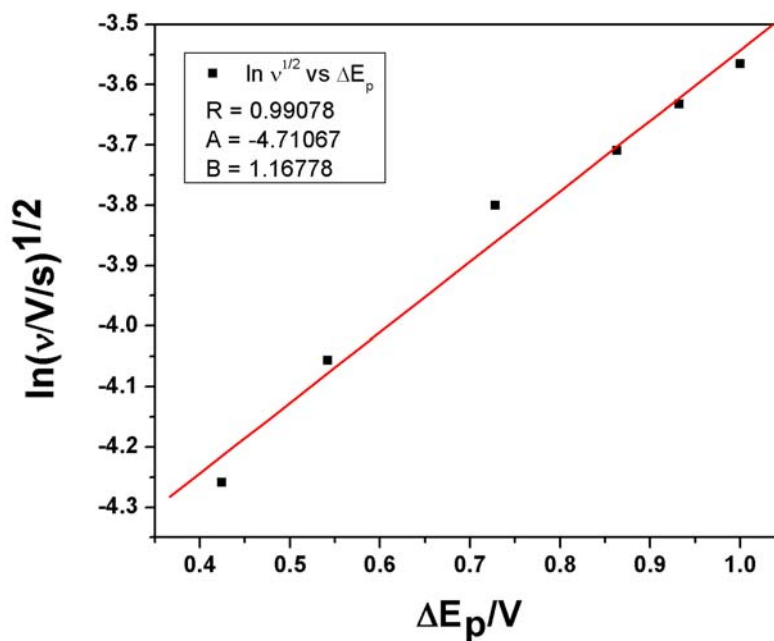
Figure 43: The plot of $\ln\left(v^{1/2}\right)$ vs. ΔE_p for pristine LiFePO$_4$.

Considering Equation (94), α was calculated according to the treatment for the general case of a quasi-reversible one-step, one-electron reaction which follows the equation [145]:

$$I_p = \frac{\alpha F^2 A v \Gamma}{2.718 RT} \tag{95}$$

Where Γ is the surface concentration of electroactive species and calculated according to the equation [145]:

$$Q = nFA\Gamma \tag{96}$$

$$\Rightarrow \Gamma = \frac{Q}{nFA} \tag{97}$$

From Equation (95),

$$I_p = \left(\frac{\alpha F^2 A \Gamma}{2.718 RT} \right)(v) \tag{98}$$

Equation (98) is now of the form, $y = mx$;

$\Rightarrow$ That a plot of I_p vs. v (Figure 37 (i) for the composite electrode and Appendix B (i) for the pristine electrode) gives slope $= \dfrac{I_p}{v} = \dfrac{\alpha F^2 A \Gamma}{2.718 RT}$ $\tag{99}$

$$\Rightarrow \alpha = \frac{2.718 RT}{F^2 A \Gamma} \times slope \tag{100}$$

Thus, using the respective values of D (calculated from CV); Q; Γ and α, the values of k_s from the graphs were found to be 7.05 x 10^{-7} cm/s for the LiFePO$_4$/10% FeCoCNT-PA composite cathode and 2.68 x 10^{-7} cm/s for the pristine LiFePO$_4$. This shows that electrode reactions are kinetically more facile in the modified cathode system than in the unmodified one. The summary of the calculated kinetic parameters are shown in Table 10:

3.1.5 Conductance studies

Conductance may be defined in the context of cyclic voltammetry as a measure of how well an electroactive specie carries an electric current. By applying the classical Ohm's relation to multiple potential scan rate cyclic voltammetry, the conductance pofile of the redox states of the electrodes (pristine and composite) can be determined [186]. From Ohm's law:

$$V = IR \tag{101}$$

$$\Rightarrow R = \frac{V}{I}$$

But conductance, G, is the reciprocal of R

$$\therefore G = \frac{I}{V} = \frac{I_v}{E_v} \tag{102}$$

In a multiple scan rate study,

$$G = \frac{\Delta I_v}{\Delta E_v} \tag{103}$$

Where $\Delta I_v = I_{p(0.5\ mV/s)} - I_{p(0.1\ mV/s)}$

$\Delta E_v = E_{p(0.5\ mV/s)} - E_{p(0.1\ mV/s)}$

From Figures 32 and 34, the conductance values of the two redox states of each cathode (pristine and composite) were determined by taking the average value for the two redox states. The values are shown in Table 10. The composite cathode gave higher conductance values as a result of the conductive additives present. The values agree with reported values from cyclic voltammetry [186].

Table 10: Electrochemical kinetic parameters of LiFePO$_4$/10% FeCoCNT-PA and LiFePO$_4$ obtained from cyclic voltammetry at 298 K.

Cathode	D/cm^2 s^{-1}	Q/C	Γ/molcm^{-2}	α	k_s/cm s^{-1}	Conductance/S
composite	1.0 x 10^{-9}	1.95	1.005 x 10^{-5}	0.3	7.05 x 10^{-7}	1.83 x 10^{-2}
pristine	4.81 x 10^{-11}	1.62	8.361 x 10^{-6}	0.1	2.68 x 10^{-7}	8.21 x 10^{-3}

3.1.6 EIS studies (Part 2)

Further to discussions on EIS (Section 3.1.2), Figures 44 and 45 represent the Nyquist and Bode phase-impedance plots of the pristine and composite electrodes:
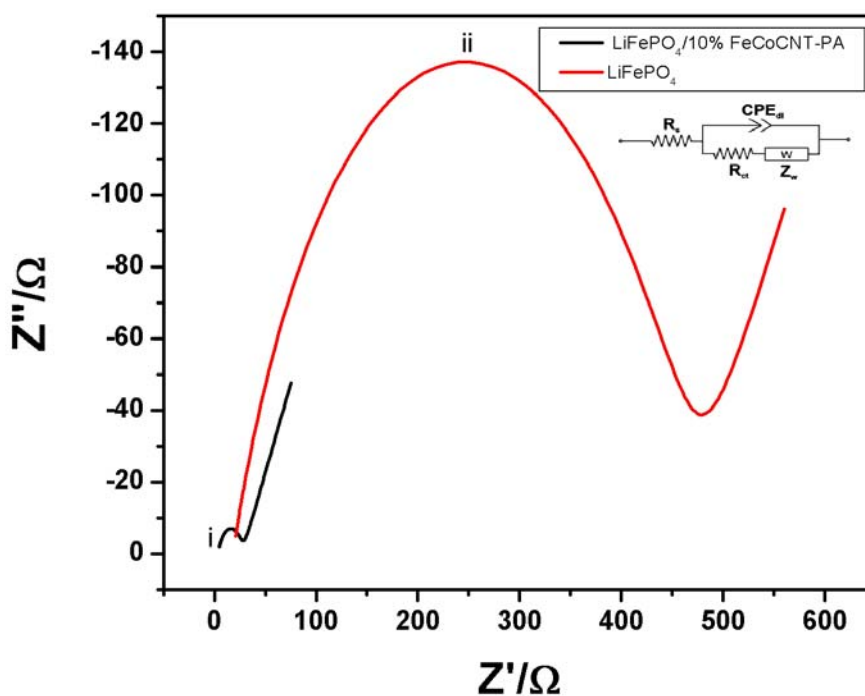
Figure 44: Comparative Nyquist plots of (i) LiFePO$_4$/10% FeCoCNT-PA and (ii) pristine LiFePO$_4$ at formal potential of 3.4 V vs. Li/Li$^+$ and perturbation amplitude of 5 mV.

The discussions follow similar trends as in the comparisons made between the LiFePO$_4$/10% FeCoCNT-PA and LiFePO$_4$/50% FeCoCNT-PA composite cathodes (Section 3.1.2). A marked decrease in semi-circle shows that the composite electrode has better conducting properties with enhanced electron transfer mediation than the pristine electrode. This observation is corroborated by the Bode phase-impedance plots. The plot of Z_{re} vs. $\omega^{-\frac{1}{2}}$ for pristine LiFePO$_4$ is shown in Appendix D.
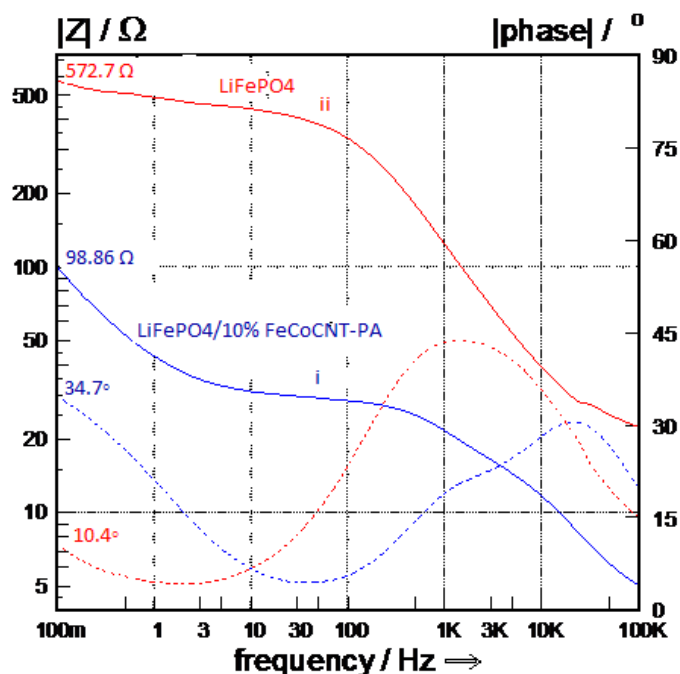
Figure 45: Comparative Bode phase-impedance diagrams of (i) LiFePO$_4$/10% FeCoCNT-PA and (ii) pristine LiFePO$_4$ at 3.4 V vs. Li/Li$^+$ and perturbation amplitude of 5 mV.

The Figure shows higher impedance to electron transfer on the pristine electrode as evidenced by the impedance and phase angle values at low frequency regimes where disturbances to the equilibrium positions of the systems are minimal. This lends credence to the fact that facile electrode kinetics takes place on the composite cathode than on the unmodified LiFePO$_4$. Table 11 gives a summary of the kinetic parameters determined for both electrodes from electrochemical impedance spectroscopy:

Table 11: Kinetic parameters of LiFePO$_4$/10% FeCoCNT-PA and LiFePO$_4$ obtained from electrochemical impedance spectroscopy at 298 K.

Cathode	τ/s rad^{-1}	R_{ct}/Ω	I_o/A	k_{et}/cm s^{-1}	σ/Ω s$^{-1/2}$	D_{app}/cm^2 s^{-1}
composite	6.43 x 10^{-5}	24.57	1.045 x 10^{-3}	2.36 x 10^{-7}	38.41	4.57 x 10^{-14}
pristine	9.76 x 10^{-4}	450.7	5.70 x 10^{-5}	1.20 x 10^{-8}	82.27	9.97 x 10^{-15}

3.1.7 Charge/discharge studies

The rate capability and cyclic stability of the composite and pristine electrodes were investigated for potential applicability in lithium ion batteries with respect to deinsertion/insertion of lithium using the LIR 2032 coin cells. Typical charge/discharge profiles at 0.1 C rates for both electrodes are shown in Figures 46 and 47.
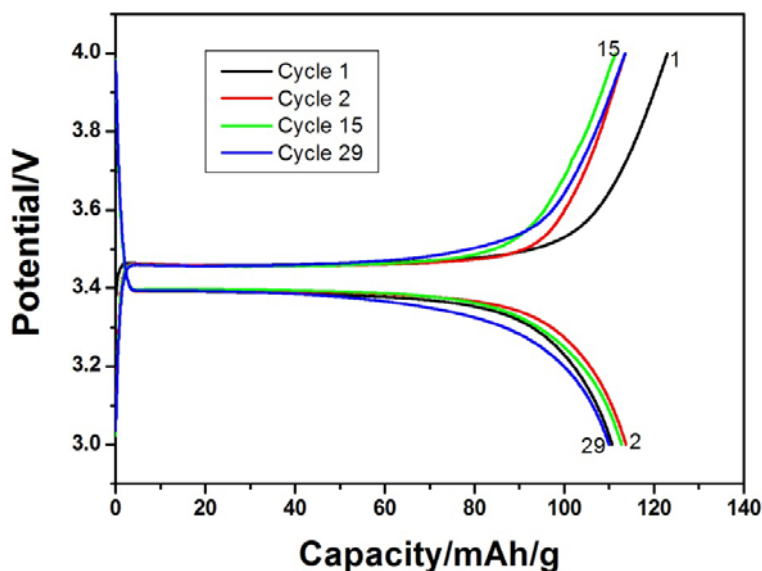
Figure 46: Charge/discharge curves of composite LiFePO$_4$/10% FeCoCNT-PA at 0.1 C rates for the 1st, 2nd 15th and 29th cycles.
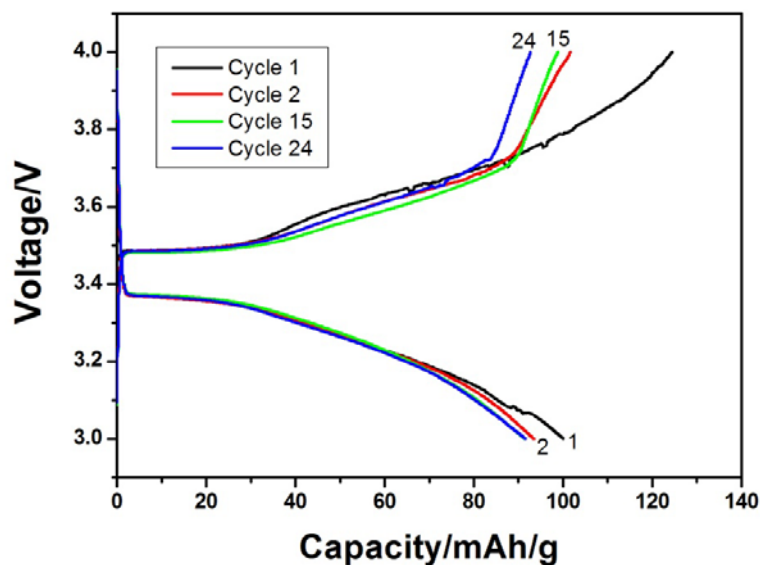
Figure 47: Charge/discharge curves of pristine LiFePO$_4$ at 0.1 C rates for the 1st, 2nd 15th and 24th cycles.

A flat charge/discharge voltage plateau was observed for both the pristine LiFePO$_4$ and composite LiFePO$_4$/10% FeCoCNT-PA systems between 3.4 V - 3.5 V ranges which is consistent with the CV formal potential obtained at around 3.44 V and typical of a well-defined LiFePO$_4$ olivine structure indicating the two-phase nature of lithium deinsertion/insertion between LiFePO$_4$ and FePO$_4$ [112]. The length of the flat voltage-plateau, gives the cell capacity [116]. In other words, a long flat voltage-plateau indicates a high charge/discharge capacity. As shown in Figure 48 for the 15th cycle, the composite cathode exhibits a longer and flatter voltage profile than the pristine electrode thus giving a charge and discharge capacities of 111.41 and 112.78 mAh/g; respectively. The pristine electrode, with a broader and shorter voltage plateau, gave charge and discharge capacities at 98.88 mAh/g and 91.29 mAh/g. The closeness of both capacities for the composite electrode indicates higher reversibility of the electrochemical processes during cycling.
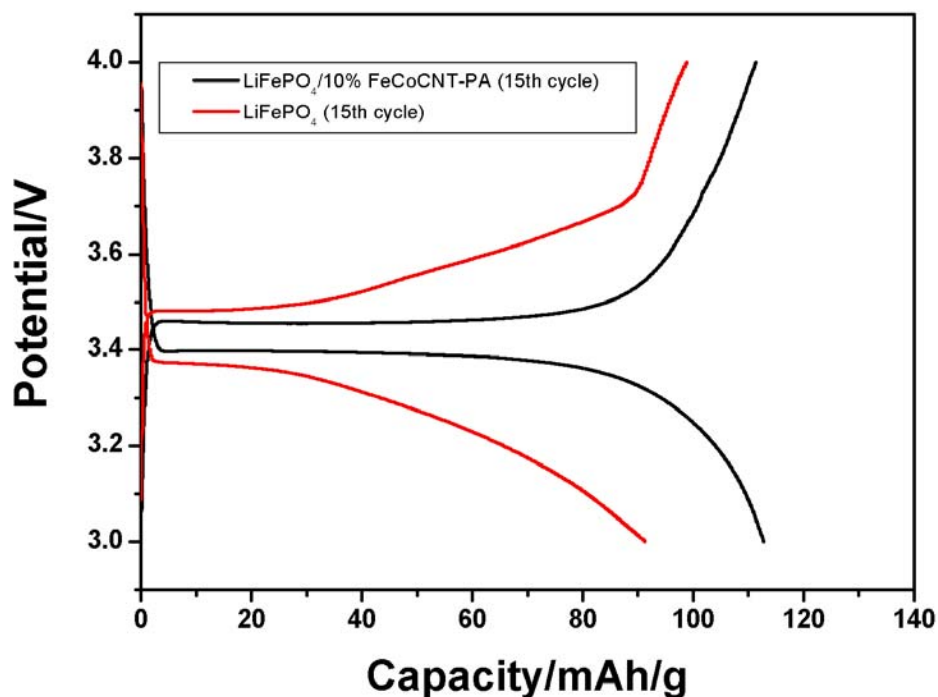
Figure 48: Comparative charge/discharge curves of composite LiFePO$_4$/10% FeCoCNT-PA and pristine LiFePO$_4$ at 0.1 C rates for the 15th cycle.

The charge-discharge capacities of the pristine and composite electrodes for several successive cycles are shown in Figures 49 – 52. The composite cathode exhibited an almost constant charge capacity profile than the pristine electrode. A similar occurrence was observed in the respective discharge profiles. This behaviour culminated in the composite electrode having higher capacity retention which is also related to good cycle reversibility and higher coulombic efficiency. The poor cycle stability of the pristine elctrode obviously affected its rate performance as shown in Table 12.
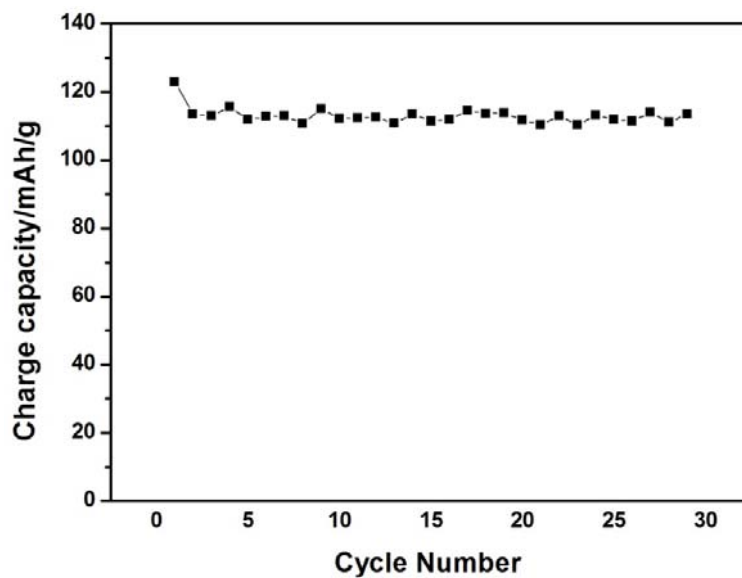
Figure 49: Charge capacity vs cycle number profile for the first 29 cycles of composite LiFePO$_4$/10% FeCoCNT-PA at 0.1 C.
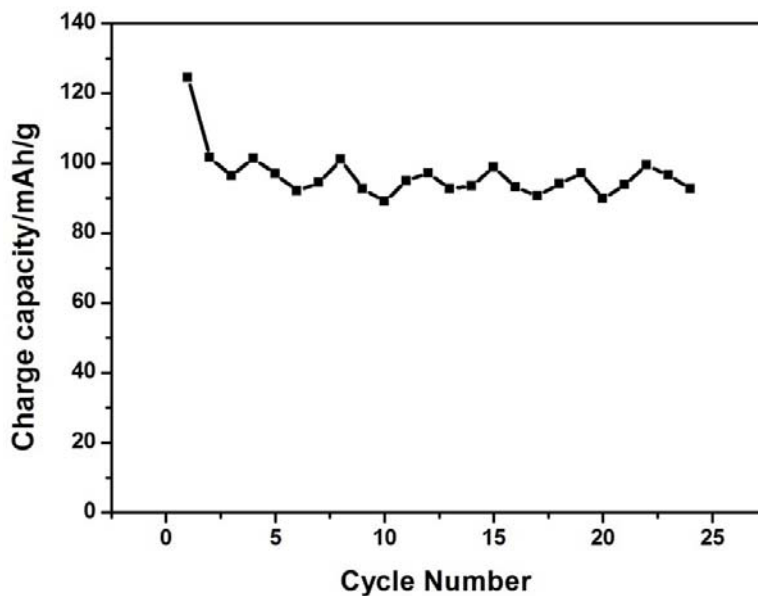
Figure 50: Charge capacity vs cycle number profile for the first 24 cycles of pristine LiFePO$_4$ at 0.1 C.
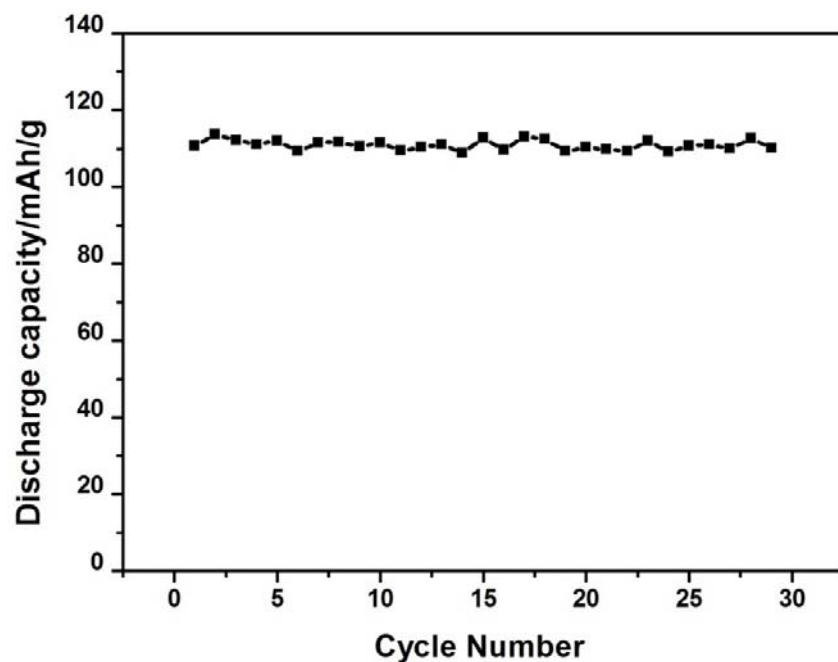
Figure 51: Discharge capacity vs cycle number profile for the first 29 cycles of composite LiFePO$_4$/10% FeCoCNT-PA at 0.1 C.
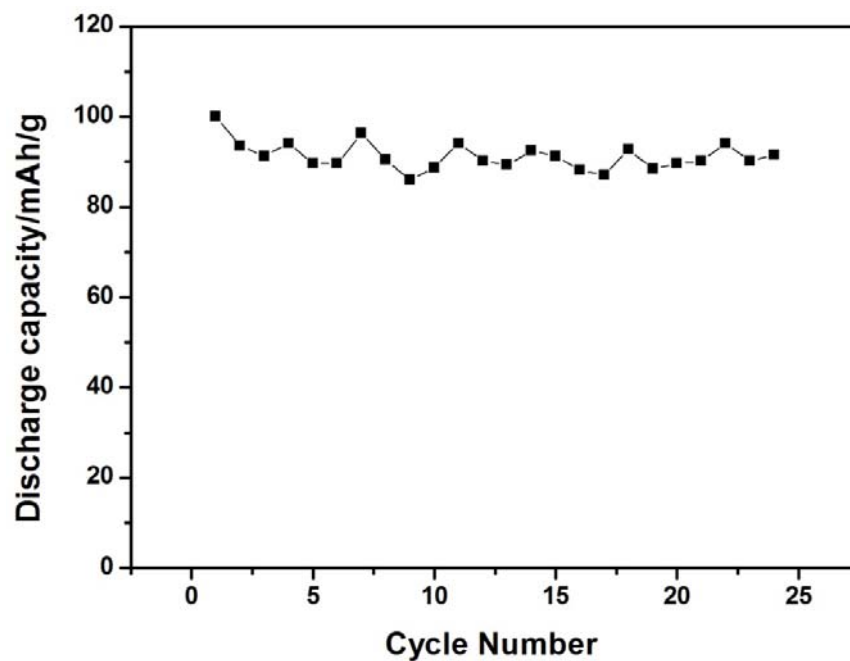
Figure 52: Discharge capacity vs cycle number profile for the first 24 cycles of pristine LiFePO$_4$ at 0.1 C.

Table 12: Charge-discharge data for composite $LiFePO_4$/10% FeCoCNT-PA and $LiFePO_4$ cathode materials at 0.1 C rates between 3.0 and 4.0 V at 298K.

Cathode	1st cycle Q_{charge}/mAh/g	1st cycle $Q_{discharge}$/mAh/g	Loss /%	Last cycle $Q_{discharge}$/mAh/g	Capacity retention/%	Coulombic efficiency/%
composite	122.95	110.66	10	110.35	99.72	90.00
pristine	124.44	100.00	19.64	89.61	89.61	80.36

Loss = (1st cycle Q_{charge} − 1st cycle $Q_{discharge}$)/ (1st cycle Q_{charge}) x 100% [168].

Capacity retention = (last cycle $Q_{discharge}$/1st cycle $Q_{discharge}$) x 100% [168].

Coulombic efficiency = (ratio of discharge capacity to charge capacity) x 100% [187].

Figures 49-52 show that the total number of cycles for the composite cathode is 39, while that for the pristine electrode is 24. Hence, for ease of comparison, the 20th cycle was chosen as the last cycle in Table 12. Comparing capacity results obtained from CV with that from charge/discharge experiments, it was observed that higher capacities were achieved from the former technique than the latter as demonstrated in Tables 13 and 14:

Table 13: Comparative analysis between capacity data obtained from CV and charge/discharge experiments for composite $LiFePO_4$/10% FeCoCNT-PA at 298 K.

Technique	Q_{charge}/mAh/g	$Q_{discharge}$/mAh/g
CV at 0.1 mV/s	148	134
Charge/discharge at 0.1 C rates (1st cycle)	123	111

Table 14: Comparative analysis between capacity data obtained from CV and charge/discharge experiments for pristine LiFePO$_4$ at 298 K.

Technique	Q_{charge}/mAh/g	$Q_{discharge}$/mAh/g
CV at 0.1 mV/s	127	117
Charge/discharge at 0.1 C rates (1st cycle)	124	100

This discrepancy could be as a result of inefficiencies in current during battery charge/discharge cycling. It was observed that the 10 h discharge time expected for a charge/discharge experiment at the 0.1 C rates took about 7 h to run meaning that the whole time-range was not fully exploited. In contrast, a run time of almost 10 h was observed during CV experiments. This might be connected to the lower capacity performance when compared with results reported by other researchers which were obtained from charge/discharge experiments [188-191]. However, the capacities were observed to be higher than those obtained by some other researchers [192-193].

3.1.8 Capacitance studies

As stated earlier in this thesis (Section 1.1), electrical energy can be stored in two fundamental different ways: (a) in batteries (indirectly) as potentially available chemical energy requiring Faradaic oxidation and reduction of the electrochemically active reagents to release charge that can perform electrical work when they flow between two electrodes having different electrode potentials [142] and (b) in supercapacitors (directly) in an electrostatic way as negative and positive electric charges on the plates of a capacitor, a

process known as non-Faradaic electrical energy storage [142]. The energy stored by supercapacitors is measured in Farad, which is the international system of units (SI unit) for capacitance. Supercapacitors are characterised by high capacitance values in Farad ranges [194]. Thus, in terms of capacitance, the high performance composite cathode system, $LiFePO_4$/10% FeCoCNT-PA, can also serve as a supercapacitor material as demonstrated below. Since the capacitance (C) of an electrode is given by the formula:

$$C = \frac{Q}{m \times \Delta E}$$

(104)

The Q (of discharge) calculated for $LiFePO_4$/10% FeCoCNT-PA composite (Section 3.1.1) is 1.77 C; and since 1 Coulomb = 1 As (ampere x second) = 1 FV (Farad x volt), it implies that 1.77 C = 1.77 FV; m = electrode mass = 3.672 mg = 3.672 x 10^{-3} g; voltage range of CV = 2.3 to 4.0 V, which implies that ΔE = 4.0 − 2.3 V = 1.7 V. Substituting all the values, Equation (104) becomes,

$$C = \frac{1.77\,(FV)}{3.672 \times 10^{-3}\,(g) \times 1.7\,(V)}$$

(105)

$$\Rightarrow C = 283.7\,F/g$$

The above value is the specific capacitance of the high performance composite cathode obtained from CV data. From Table 12, the discharge capacity from the first cycle obtained for the high performance composite cathode is 110.66 mAh/g. This can be converted to capacitance according to the following steps:

110.66 mAh/g = 110.66 x 10^{-3} Ah/g

But 1 Ah = 3600 As

$$\therefore 110.66 \text{ x } 10^{-3} \text{ Ah/g} = \frac{110.66 \text{ x } 10^{-3} \text{ (Ah/g)}}{1 \text{(Ah)}} \text{ x } 3600 \text{ (As)} = 398.38 \text{ As/g}$$

(106)

But 1 As = 1 FV

$\therefore$ 398.38 As/g = 398.38 FV/g

But the voltage range of the charge/discharge experiment = 3.0 to 4.0 V. This implies that ΔE = 4.0 – 3.0 V = 1.0 V. Therefore, applying Equation (104), the specific capacitance becomes:

$$C = \frac{398.38 \text{ (FV/g)}}{1 \text{ (V)}} = 398.38 \text{ F/g}$$

(107)

This high value of 398.38 F/g was orchestrated by the presence of the conductive FeCo-derivatised CNTs and polyaniline nanomaterials and is consistent with capacitance values reported for supercapacitor materials of high specific capacitance [195-200].

3.2 Electron microscopy studies

HRTEM micrographs of synthesized FeCo bimetallic nanoparticles (Figure 53) showed spherical nanoparticles of 35-50 nm in diameter connected in chains of beads due to magnetic and electronic interactions between the metal particles [201].
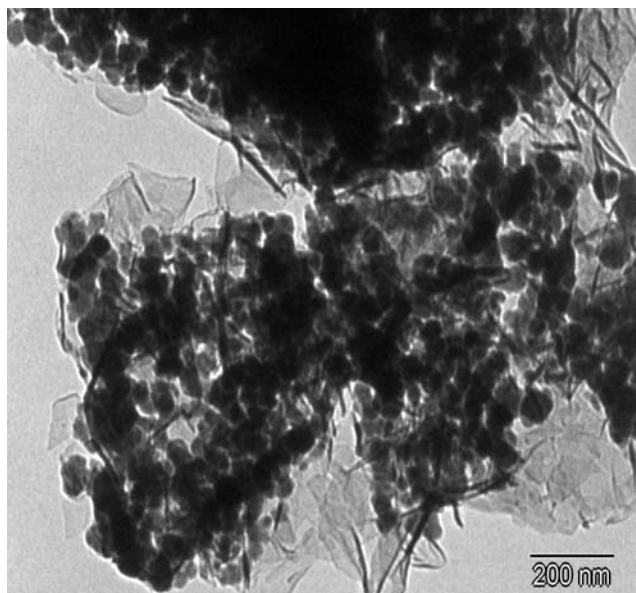
Figure 53: HRTEM micrograph of FeCo nanoparticles.

Similar HRTEM images have been reported for FeCo nanoparticles [202-203]. The elemental analysis from EDX (Table 15) showed that the nanoparticles contain 56.84% Fe and 43.15 % Co. This distribution is close to the original ratio (3:2) of the metal precursors in the reaction mixture. The oxygen peak in the EDX profile (Figure 54) could be as a result of surface oxidation of FeCo nanoparticles during sample preparation and characterization; the peaks from carbon and copper were from the carbon-coated copper grid used during analysis.

Table 15: EDX Analysis of FeCo Nanoparticles.

Element	Weight %	Atomic %	Uncertainty %	Detector Correction	k-Factor
Fe(K)	56.84	58.16	0.19	0.99	1.403
Co(K)	43.15	41.83	0.16	0.99	1.495
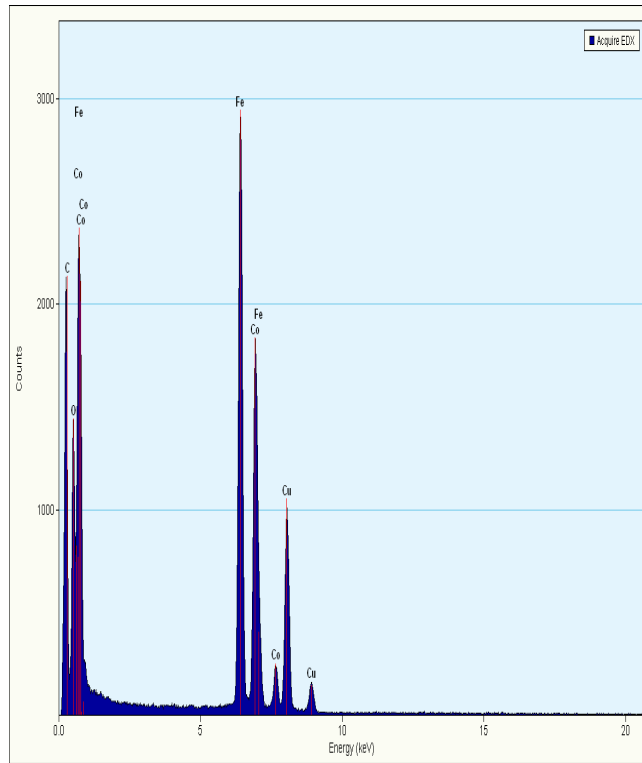
Figure 54: EDX profile of FeCo nanoparticles.

The morphology of the nanoparticles as obtained from SEM (Figure 55) revealed porous nanoclusters which facilitate movement of electrons during extraction and insertion of lithium within the 3D framework between the nanotubes and adjacent $LiFePO_4$ particles [178] as explained earlier on (Section 3.1.3).
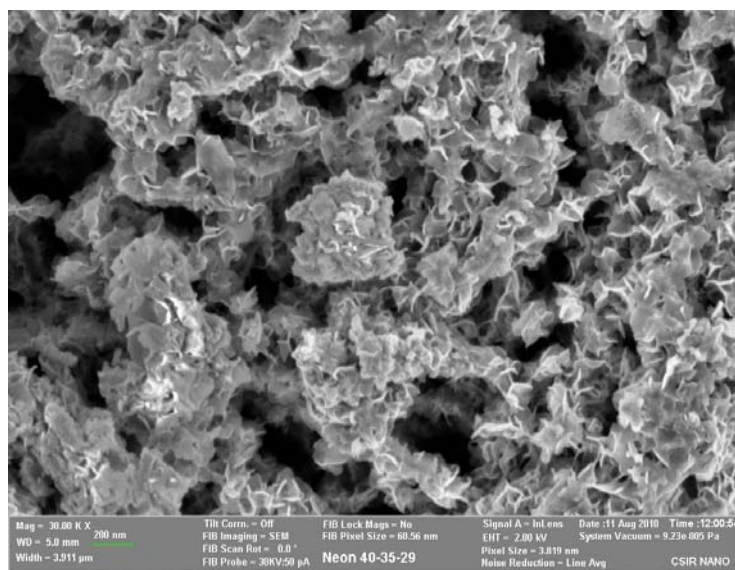
Figure 55: SEM micrograph of FeCo nanoparticles.

The porous nanoclusters thus provide wider electrode surface area that helps to minimize energy loss due to both activation and concentration polarisations at the electrode surface and increase the electrode efficiency or utilisation [11].

The synthesised FeCo nanoparticles were subsequently attached to the ends and walls of the nanotubes. Prior to this, the raw nanotubes were purified by acid-treatment to render them soluble for further characterisation and application. Figures 56 and 57 show the HRTEM images of raw and purified CNTs.
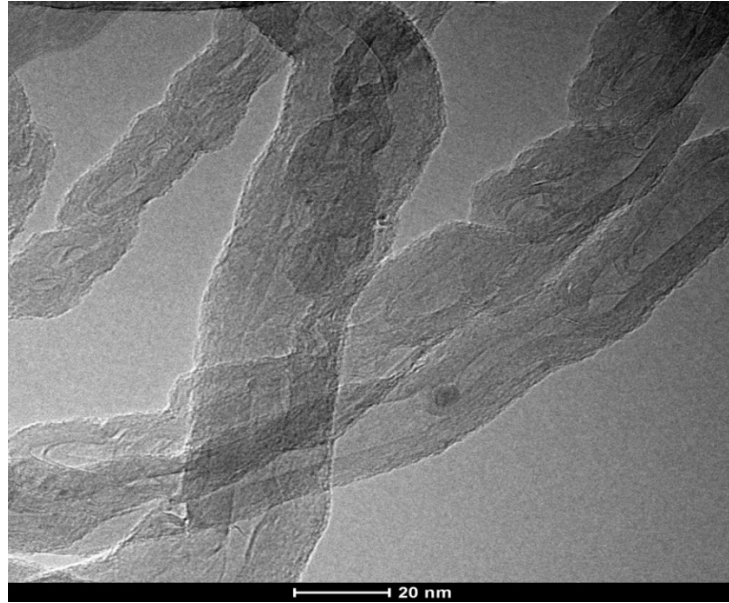
Figure 56: HRTEM micrograph of raw CNTs.

The image revealed several layers of graphitic carbon and hollow cores [204].

Figure 57: HRTEM micrograph of acid-purified CNTs.

The image shows a decrease in the outer diameter of the tubes with increased surface roughness when compared with the raw CNT. This observation supports the oxidative-

functionalisation of CNTs in 3: 1 H_2SO_4/HNO_3 acid mixture for 8 h ultrasonication. FeCo nanoparticles were then successfully attached to the CNTs as shown in Figure 58:
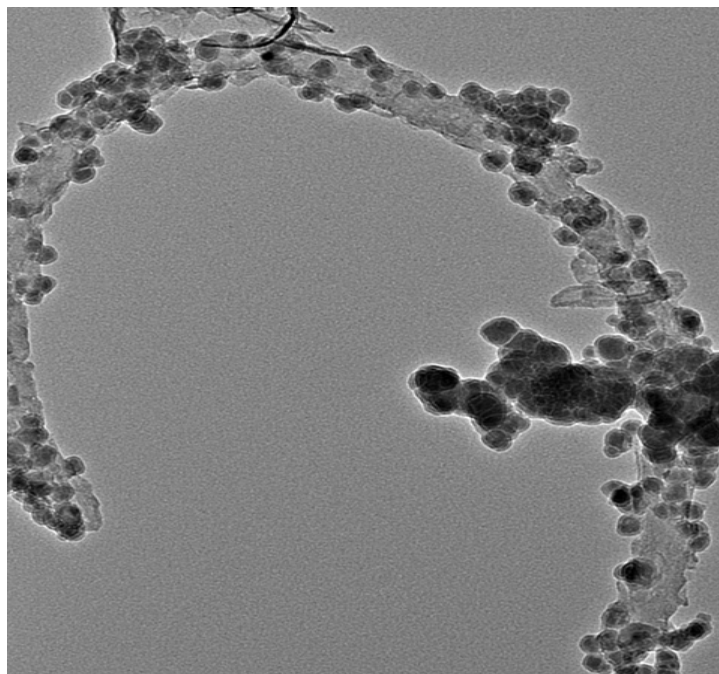
Figure 58: HRTEM micrograph of FeCo Functionalised CNTs

FeCo bimetallic nanoparticles were attached to the CNTs according to the following scheme (Scheme1):
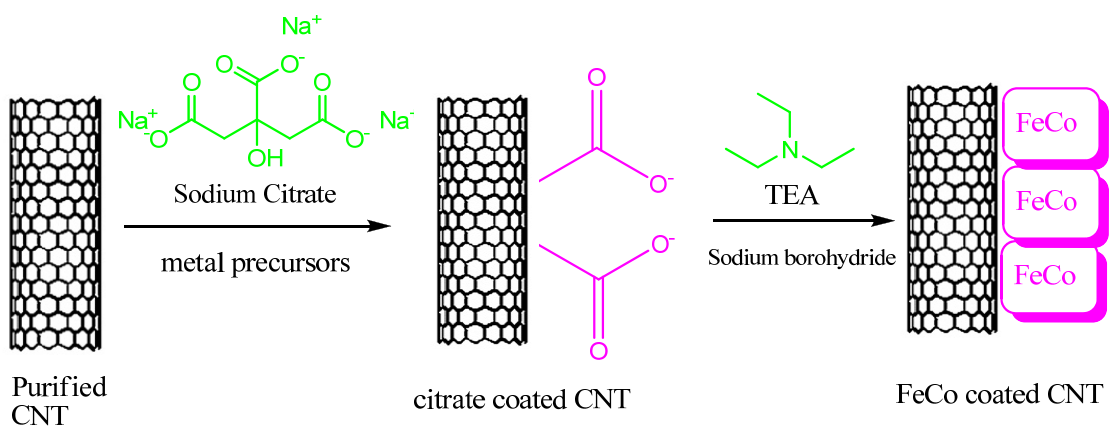
Scheme 1: Simulative view of the process for attaching FeCo nanoparticles to CNTs.

The successful fabrication of the FeCo-CNT composite through the above scheme is a prelude to the formation of the strong 3D nano-network of CNT and adjacent LiFePO$_4$ particles which through a kinetic synergy with polyaniline nanomaterials, enhances the electrochemical performance of LiFePO$_4$ as illustrated in the earlier sections of this thesis.

Chapter 4

Conclusion

Novel, high performance lithium ion battery cathode based on LiFePO$_4$/FeCoCNT-PA composites has been developed. The voltammetric, impedimetric and charge/discharge properties of this new electrode, LiFePO$_4$/10% FeCoCNT-PA were interrogated using LIR coin cells of the 2032 configuration. Scan rate studies revealed quasi-reversible behaviour of the electrode which is in agreement with findings by most researchers for composite and pristine LiFePO$_4$ electrodes. The rate constant of electron transfer calculated from both CV and EIS revealed complementary results from both techniques and showed the composite cathode having values of about an order of magnitude higher than the pristine LiFePO$_4$ electrode. This was made possible by the kinetic synergistic effects of the conductive FeCo-derivatised CNTs and polyaniline nanomaterials that were present in the composite cathode system. Due to this same synergy, values of diffusion coefficients calculated from CV showed the performance of the composite electrode to be about two orders of magnitude higher than the pristine cathode and consistent with reported values. The charge capacity of the composite electrode calculated from CV data also revealed the superiority of the modified electrode over the unmodified and was found to be about 87% of the theoretical capacity of LiFePO$_4$. The charge and discharge capacities of the composite cathode at 0.1 mV/s scan rate combined to give a reversible capacity of 91% which is consistent with the Coulombic efficiency of 90% calculated for the high performance electrode from charge/discharge experiments for the first cycle at 0.1 C rates. The discharge capacity of the high performance cathode was found to be higher than some reported values. The novel electrode exhibited excellent cyclability after 20 cycles with a capacity retention of 99.72%, a desirable property in a lithium ion cell.

The results obtained from the various electrochemical studies conducted in this thesis suggest that the novel $LiFePO_4$/10% FeCoCNT-PA composite cathode presents good properties for applications in lithium ion batteries as well as in supercapacitors as seen in the high capacitance values calculated. The overall performance of this novel cathode was orchestrated by the presence of the conductive FeCo-derivatised CNTs and polyaniline nanomaterials.

For future work, there is need for further optimization as it is necessary to study the rate capabilities of various cathode systems at different compositions and different C-rates.

References

1. http://www.un-documents.net/ocf-02.htm, *Our Common Future, Chapter 2: Towards Sustainable Development*. 1987.

2. Streimikiene, D., R. Ciegis, and D. Grundey, *Energy Indicators for Sustainable Development in Baltic States.* Renewable and Sustainable Energy Reviews, 2007. **11**(5): p. 877-893.

3. http://www.sc.doe.gov/bes/reports/files/EES_rpt.pdf, *Basic Research Needs for Electrical Energy Storage*, in *Report of the Basic Energy Sciences Workshop on Electrical Energy Storage*. 2007. p. 1-186.

4. Wakihara, M., *Recent Developments in Lithium Ion Batteries.* Materials Science and Engineering: R: Reports, 2001. **33**(4): p. 109-134.

5. Zaghib, K., et al., *LiFePO$_4$ Safe Li-Ion Polymer Batteries for Clean Environment.* Journal of Power Sources, 2005. **146**(1-2): p. 380-385.

6. Aifantis, K.E., S.A. Hackney, and R.V. Kumar, *High Energy Density Lithium Batteries*. 2010, Weinheim: Wiley-VCH

7. Dincer, I. and C. Zamfirescu, *Sustainable Energy Systems and Applications*. 2011, New York: Springer. 816.

8. Kiehne, H.A., ed. *Battery Technology Handbook*. 2nd ed. 2003, Marcel Dekker, Inc.: New York.

9. Béguin, F. and E. Frackowiak, *Carbons for Electrochemical Energy Storage and Conversion Systems*. Advanced Materials and Technologies Series, ed. Y. Gogotsi. 2010: CRC Press, Taylor and Francis Group.

10. Huggins, R.A., *Energy Storage*. 2010: Springer.

11. Linden, D. and T.B. Reddy, eds. *Handbook of Batteries*. 3rd ed. 2002, McGraw-Hill.

12.   Winter, M. and R.J. Brodd, *What Are Batteries, Fuel Cells, and Supercapacitors?* Chemical Reviews, 2004. **104**(10): p. 4245-4270.

13.   Tarascon, J.M. and M. Armand, *Issues and Challenges Facing Rechargeable Lithium Batteries.* Nature, 2001. **414**(6861): p. 359-367.

14.   http://www.freedoniagroup.com/World-Batteries.html, *World Batteries to 2014 - Demand and Sales Forecasts, Market Share, Market Size, Market Leaders (Study #2703)* 2010, Freedonia Group.

15.   Armand, M. and J.M. Tarascon, *Building Better Batteries.* Nature, 2008. **451**(7179): p. 652-657.

16.   Fergus, J.W., *Recent Developments in Cathode Materials for Lithium Ion Batteries.* Journal of Power Sources, 2010. **195**(4): p. 939-954.

17.   Arico, A.S., et al., *Nanostructured Materials for Advanced Energy Conversion and Storage Devices.* Nature Materials, 2005. **4**: p. 366-377.

18.   Scrosati, B. and J. Garche, *Lithium Batteries: Status, Prospects and Future.* Journal of Power Sources, 2010. **195**(9): p. 2419-2430.

19.   Shukla, A.K. and T.P. Kumar, *Materials for Next-Generation Lithium Batteries.* Current science, 2008. **94**(3): p. 314-331.

20.   Xu, K., *Nonaqueous Liquid Electrolytes for Lithium-Based Rechargeable Batteries.* Chemical Reviews 2004. **104**: p. 4303-4417.

21.   Nazri, G.-A. and G. Pistoia, eds. *Lithium Batteries Science and Technology*. 2003, Springer.

22.   Wakihara, M. and O. Yamamoto, eds. *Lithium Ion Batteries: Fundamentals and Performance*. 1998, Kodansha Ltd., Tokyo (Japan),Wiley-VCH Verlag GmbH, Weinheim (Federal Republic of Germany). 247.

23.   Besenhard, J., ed. *Handbook of Battery Materials*. 1999, Wiley-VCH.

24. Hassoun, J., P. Reale, and B. Scrosati, *Recent Advances in Liquid and Polymer Lithium-Ion Batteries.* Journal of Materials Chemistry, 2007. **17**(35): p. 3668-3677.

25. Winter, M., et al., *Insertion Electrode Materials for Rechargeable Lithium Batteries.* Advanced Materials, 1998. **10**(10): p. 725-763.

26. Treptow, R.S., *Lithium Batteries: a Practical Application of Chemical Principles.* Journal of Chemical Education, 2003. **80**(9): p. 1015.

27. Dey, A.N., *Electrochemical Alloying of Lithium in Organic Electrolytes.* Journal of The Electrochemical Society, 1971. **118**(10): p. 1547-1549.

28. Winter, M. and J.O. Besenhard, *Electrochemical Lithiation of Tin and Tin-Based Intermetallics and Composites.* Electrochimica Acta, 1999. **45**(1-2): p. 31-50.

29. Huggins, R.A., *Lithium Alloy Anodes*, in *Handbook of Battery Materials*, J.O. Besenhard, Editor. 1999, Wiley VCH: Weinheim.

30. Wang, Y. and G. Cao, *Developments in Nanostructured Cathode Materials for High-Performance Lithium-Ion Batteries* Advanced Materials, 2008. **20**: p. 2251-2269.

31. Whittingham, M.S., *Lithium Batteries and Cathode Materials.* Chemical Reviews, 2004. **104**(10): p. 4271-4302.

32. Daniel, C., *Materials and Processing for Lithium-Ion Batteries.* Journal of Materials and Coatings, 2008. **60**(9): p. 43-48.

33. Yamaki, J.-i., *Liquid Electrolytes*, in *Advances in Lithium-Ion Batteries*, W.v. Schalkwijk and B. Scrosati, Editors. 2002, Kluwer Academic/Plenum Publishers.

34. Guyomard, D. and J.M. Tarascon, *Rechargeable $Li_{1+x}Mn_2O_4$/Carbon Cells with a New Electrolyte Composition.* Journal of The Electrochemical Society, 1993. **140**(11): p. 3071-3081.

35.   Tarascon, J.M. and D. Guyomard, *New Electrolyte Compositions Stable over the 0 to 5 V Voltage Range and Compatible with the $Li_{1+x}Mn_2O_4$/Carbon Li-Ion Cells.* Solid State Ionics, 1994. **69**(3-4): p. 293-305.

36.   Fong, R., U. von Sacken, and J.R. Dahn, *Studies of Lithium Intercalation into Carbons Using Nonaqueous Electrochemical Cells.* Journal of The Electrochemical Society, 1990. **137**(7): p. 2009-2013.

37.   Aurbach, D., et al., *The Study of Electrolyte Solutions Based on Ethylene and Diethyl Carbonates for Rechargeable Li Batteries.* Journal of The Electrochemical Society, 1995. **142**(9): p. 2873-2882.

38.   Peled, E., et al., *An Advanced Tool for the Selection of Electrolyte Components for Rechargeable Lithium Batteries.* Journal of The Electrochemical Society, 1998. **145**(10): p. 3482-3486.

39.   Ein-Eli, Y., et al., *Ethylmethylcarbonate, a Promising Solvent for Li-Ion Rechargeable Batteries.* Journal of The Electrochemical Society, 1996. **143**(12): p. L273-L277.

40.   Jang, D.H. and S.M. Oh, *Electrolyte Effects on Spinel Dissolution and Cathodic Capacity Losses in 4 V $Li/Li_xMn_2O_4$ Rechargeable Cells.* Journal of The Electrochemical Society, 1997. **144**(10): p. 3342-3348.

41.   Takata, K.-i., et al., *Cycling Characteristics of Secondary Li Electrode in $LiBF_4$/Mixed Ether Electrolytes.* Journal of The Electrochemical Society, 1985. **132**(1): p. 126-128.

42.   Ue, M. and S. Mori, *Mobility and Ionic Association of Lithium Salts in a Propylene Carbonate-Ethyl Methyl Carbonate Mixed Solvent.* Journal of The Electrochemical Society, 1995. **142**(8): p. 2577-2581.

43. Zhang, S.S., K. Xu, and T.R. Jow, *Study of LiBF$_4$ as an Electrolyte Salt for a Li-Ion Battery.* Journal of The Electrochemical Society, 2002. **149**(5): p. A586-A590.

44. Zhang, S.S., K. Xu, and T.R. Jow, *A New Approach Toward Improved Low Temperature Performance of Li-Ion Battery.* Electrochemistry Communications, 2002. **4**(11): p. 928-932.

45. Blomgren, G.E., *Liquid Electrolytes for Lithium and Lithium-Ion Batteries.* Journal of Power Sources, 2003. **119-121**: p. 326-329.

46. Ozawa, K., *Lithium-Ion Rechargeable Batteries with LiCoO$_2$ and Carbon Electrodes: the LiCoO$_2$/C System.* Solid State Ionics, 1994. **69**(3-4): p. 212-221.

47. Rauh, R.D., T.F. Reise, and S.B. Brummer, *Efficiencies of Cycling Lithium on a Lithium Substrate in Propylene Carbonate.* Journal of The Electrochemical Society, 1978. **125**(2): p. 186-190.

48. Jasinski, R. and S. Carroll, *Thermal Stability of a Propylene Carbonate Electrolyte.* Journal of The Electrochemical Society, 1970. **117**(2): p. 218-219.

49. Newman, G.H., et al., *Hazard Investigations of LiClO$_4$/Dioxolane Electrolyte.* Journal of The Electrochemical Society, 1980. **127**(9): p. 2025-2027.

50. Marom, R., et al., *Revisiting LiClO$_4$ as an Electrolyte for Rechargeable Lithium-Ion Batteries.* Journal of The Electrochemical Society, 2010. **157**(8): p. A972-A983.

51. Song, J.Y., Y.Y. Wang, and C.C. Wan, *Review of Gel-Type Polymer Electrolytes for Lithium-Ion Batteries.* Journal of Power Sources, 1999. **77**(2): p. 183-197.

52. Scrosati, B., *Lithium Polymer Electrolytes*, in *Advances in Lithium-Ion Batteries*, W.v. Schalkwijk and B. Scrosati, Editors. 2002, Kluwer Academic/Plenum.

53. Nishi, Y., *Lithium-Ion Secondary Batteries with Gelled Polymer Electrolytes*, in *Advances in Lithium-Ion Batteries*, W.v. Schalkwijk and B. ScrosatiPublishers, Editors. 2002, Kluwer Academic/Plenum

54.   Tarascon, J.M., et al., *Performance of Bellcore's Plastic Rechargeable Li-Ion Batteries.* Solid State Ionics, 1996. **86-88**(Part 1): p. 49-54.

55.   Han, K.N., et al., *Development of a Plastic Li-Ion Battery Cell for EV Applications.* Journal of Power Sources, 2001. **101**(2): p. 196-200.

56.   Whittingham, M.S., *Electrical Energy Storage and Intercalation Chemistry.* Science, 1976. **192**(4244): p. 1126-1127.

57.   Yoshio, M., R.J. Brodd, and A. Kozawa, *Lithium Ion Batteries*. 2009, New York: Springer.

58.   Manthiram, A., *Materials Aspect: an Overview*, in *Lithium Batteries Science and Technology*, G.-A. Nazri and G. Pistoia, Editors. 2003, Springer.

59.   Manthiram, A. and J. Kim, *Low Temperature Synthesis of Insertion Oxides for Lithium Batteries.* Chemistry of Materials, 1998. **10**(10): p. 2895-2909.

60.   Needham, S.A., et al., *Synthesis and Electrochemical Performance of Doped $LiCoO_2$ Materials.* Journal of Power Sources, 2007. **174**(2): p. 828-831.

61.   Whittingham, M.S., *Inorganic Nanomaterials for Batteries.* Dalton Transactions, 2008(40): p. 5424-5431.

62.   Shu, Z.X., R.S. McMillan, and J.J. Murray, *Electrochemical Intercalation of Lithium into Graphite.* Journal of The Electrochemical Society, 1993. **140**(4): p. 922-927.

63.   Dahn, J.R., et al., *Dependence of the Electrochemical Intercalation of Lithium in Carbons on the Crystal Structure of the Carbon.* Electrochimica Acta, 1993. **38**(9): p. 1179-1191.

64.   Ogumi, Z. and M. Inaba, *Carbon Anodes*, in *Advances in Lithium-Ion Batteries*, W.v. Schalkwijk and B. Scrosati, Editors. 2002, Kluwer Academic/Plenum.

65.   Peled, E., *The Electrochemical Behavior of Alkali and Alkaline Earth Metals in Nonaqueous Battery Systems---the Solid Electrolyte Interphase Model.* Journal of The Electrochemical Society, 1979. **126**(12): p. 2047-2051.

66.   Sato, K., et al., *A Mechanism of Lithium Storage in Disordered Carbons.* Science, 1994. **264**(5158): p. 556-558.

67.   Beaulieu, L.Y., et al., *Colossal Reversible Volume Changes in Lithium Alloys.* Electrochemical and Solid-State Letters, 2001. **4**(9): p. A137-A140.

68.   Dahlin, G.R. and K.E. Strom, *Lithium Batteries: Research, Technology and Applications*. 2010, New York: Nova Science Publishers, Inc.

69.   Aurbach, D., et al., *Review on Electrode-Electrolyte Solution Interactions, Related to Cathode Materials for Li-Ion Batteries.* Journal of Power Sources, 2007. **165**(2): p. 491-499.

70.   Broussely, M., P. Biensan, and B. Simon, *Lithium Insertion into Host Materials: the Key to Success for Li Ion Batteries.* Electrochimica Acta, 1999. **45**(1-2): p. 3-22.

71.   Mizushima, K., et al., *Li_xCoO_2 (0<x<-1): a New Cathode Material for Batteries of High Energy Density.* Materials Research Bulletin, 1980. **15**(6): p. 783-789.

72.   Boyle, T.J., et al., *Rechargeable Lithium Battery Cathodes. Nonaqueous Synthesis, Characterization, and Electrochemical Properties of $LiCoO_2$.* Chemistry of Materials, 1998. **10**(8): p. 2270-2276.

73.   Thackeray, M., *Lithium-Ion Batteries: an Unexpected Conductor.* Nature Materials, 2002. **1**(2): p. 81-82.

74.   Goodenough, J.B. and K. Mizuchima, *Electrochemical Cell with New Fast Ion Conductors* 1981: U.S. Patent.

75. Amatucci, G.G., J.M. Tarascon, and L.C. Klein, *CoO₂, The End Member of the Li_xCoO₂ Solid Solution.* Journal of The Electrochemical Society, 1996. **143**(3): p. 1114-1123.

76. Gabrisch, H., R. Yazami, and B. Fultz, *Hexagonal to Cubic Spinel Transformation in Lithiated Cobalt Oxide.* Journal of The Electrochemical Society, 2004. **151**(6): p. A891-A897.

77. Belov, D. and M.-H. Yang, *Failure Mechanism of Li-Ion Battery at Overcharge Conditions.* Journal of Solid State Electrochemistry, 2008. **12**(7): p. 885-894.

78. Doh, C.-H., et al., *Thermal and Electrochemical Behaviour of C/Li_xCoO₂ Cell During Safety Test.* Journal of Power Sources, 2008. **175**(2): p. 881-885.

79. Goodenough, J.B., *Oxide Cathodes*, in *Advances in Lithium Ion Batteries*, W.A.v. Schalkwijk and B. Scrosati, Editors. 2002, Kluwer Academic Publishers: New York.

80. Wang, Z., et al., *Electrochemical Evaluation and Structural Characterization of Commercial LiCoO₂ Surfaces Modified with MgO for Lithium-Ion Batteries.* Journal of The Electrochemical Society, 2002. **149**(4): p. A466-A471.

81. Cho, J., Y.J. Kim, and B. Park, *LiCoO₂ Cathode Material That Does Not Show a Phase Transition from Hexagonal to Monoclinic Phase.* Journal of The Electrochemical Society, 2001. **148**(10): p. A1110-A1115.

82. Ohzuku, T., et al., *Comparative Study of LiCoO₂, LiNiCoO₂ and LiNiO₂ for 4 Volt Secondary Lithium Cells.* Electrochimica Acta, 1993. **38**(9): p. 1159-1167.

83. Lu, C.-H. and L. Wei-Cheng, *Reaction Mechanism and Kinetics Analysis of Lithium Nickel Oxide During Solid-State Reaction.* Journal of Materials Chemistry, 2000. **10**(6): p. 1403-1407.

84. Amriou, T., et al., *Ab Initio Investigation of the Jahn-Teller Distortion Effect on the Stabilizing Lithium Intercalated Compounds.* Materials Chemistry and Physics, 2005. **92**(2-3): p. 499-504.

85. Ohzuku, T., A. Ueda, and M. Nagayama, *Electrochemistry and Structural Chemistry of LiNiO$_2$ (R3m) for 4 Volt Secondary Lithium Cells.* Journal of The Electrochemical Society, 1993. **140**(7): p. 1862-1870.

86. Delmas, C., et al., *An Overview of the Li(Ni,M)O$_2$ Systems: Syntheses, Structures and Properties.* Electrochimica Acta, 1999. **45**(1-2): p. 243-253.

87. Rougier, A., P. Gravereau, and C. Delmas, *Optimization of the Composition of the Li$_{1-z}$Ni$_{1 + z}$O$_2$ Electrode Materials: Structural, Magnetic, and Electrochemical Studies.* Journal of The Electrochemical Society, 1996. **143**(4): p. 1168-1175.

88. Zhecheva, E. and R. Stoyanova, *Stabilization of the Layered Crystal Structure of LiNiO$_2$ by Co-Substitution.* Solid State Ionics, 1993. **66**(1-2): p. 143-149.

89. Delmas, C., I. Saadoune, and A. Rougier, *The Cycling Properties of the Li$_x$Ni$_{1-y}$Co$_y$O$_2$ Electrode.* Journal of Power Sources, 1993. **44**(1-3): p. 595-602.

90. Nakai, I. and T. Nakagome, *In Situ Transmission X-Ray Absorption Fine Structure Analysis of the Li Deintercalation Process in LiNi$_{0.5}$Co$_{0.5}$O$_2$.* Electrochemical and Solid-State Letters, 1998. **1**(6): p. 259-261.

91. Saadoune, I., M. Menetrier, and C. Delmas, *Redox Processes in Li$_x$Ni$_{1-y}$Co$_y$O$_2$ Cobalt-Rich Phases.* Journal of Materials Chemistry, 1997. **7**(12): p. 2505-2511.

92. Liu, H., et al., *The Effects of Sintering Temperature and Time on the Structure and Electrochemical Performance of LiNi$_{0.8}$Co$_{0.2}$O$_2$ Cathode Materials Derived from Sol-Gel Method.* Journal of Solid State Electrochemistry, 2003. **7**(8): p. 456-462.

93.   Pouillerie, C., L. Croguennec, and C. Delmas, *The $Li_xNi_{1-y}Mg_yO_2$ (y=0.05, 0.10) System: Structural Modifications Observed Upon Cycling.* Solid State Ionics, 2000. **132**(1-2): p. 15-29.

94.   Ohzuku, T., A. Ueda, and M. Kouguchi, *Synthesis and Characterization of $LiAl_{1/4}Ni_{3/4}O_2(R3m)$ for Lithium-Ion (Shuttlecock) Batteries.* Journal of The Electrochemical Society, 1995. **142**(12): p. 4033-4039.

95.   Liu, H., et al., *Structural, Electrochemical and Thermal Properties of $LiNi_{0.8-y}Ti_yCo_{0.2}O_2$ as Cathode Materials for Lithium Ion Battery.* Electrochimica Acta, 2004. **49**(7): p. 1151-1159.

96.   Dahn, J.R., et al., *Thermal Stability of Li_xCoO_2, Li_xNiO_2 and λ-MnO_2 and Consequences for the Safety of Li-ion Cells.* Solid State Ionics, 1994. **69**(3-4): p. 265-270.

97.   Guilmard, M., et al., *Thermal Stability of Lithium Nickel Oxide Derivatives. Part I: $Li_xNi_{1.02}O_2$ and $Li_xNi_{0.89}Al_{0.16}O_2$ (x = 0.50 and 0.30).* Chemistry of Materials, 2003. **15**(23): p. 4476-4483.

98.   Guilmard, M., L. Croguennec, and C. Delmas, *Thermal Stability of Lithium Nickel Oxide Derivatives. Part II: $LixNi_{0.70}Co_{0.15}Al_{0.15}O_2$ and $Li_xNi_{0.90}Mn_{0.10}O_2$ (x = 0.50 and 0.30). Comparison with $Li_xNi_{1.02}O_2$ and $Li_xNi_{0.89}Al_{0.16}O_2$.* Chemistry of Materials, 2003. **15**(23): p. 4484-4493.

99.   Armstrong, A.R. and P.G. Bruce, *Synthesis of Layered $LiMnO_2$ as an Electrode for Rechargeable Lithium Batteries.* Nature, 1996. **381**(6582): p. 499-500.

100.   Chen, R. and M.S. Whittingham, *Cathodic Behavior of Alkali Manganese Oxides from Permanganate.* Journal of The Electrochemical Society, 1997. **144**(4): p. L64-L67.

101. Armstrong, A.R., et al., *The Layered Intercalation Compounds $Li(Mn_{1-y}Co_y)O_2$: Positive Electrode Materials for Lithium-Ion Batteries.* Journal of Solid State Chemistry, 1999. **145**(2): p. 549-556.

102. Capitaine, F., P. Gravereau, and C. Delmas, *A New Variety of $LiMnO_2$ with a Layered Structure.* Solid State Ionics, 1996. **89**(3-4): p. 197-202.

103. Thackeray, M.M., *Manganese Oxides for Lithium Batteries.* Progress in Solid State Chemistry, 1997. **25**(1-2): p. 1-71.

104. Thackeray, M.M., et al., *Lithium Insertion into Manganese Spinels.* Materials Research Bulletin, 1983. **18**(4): p. 461-472.

105. Sun, Y.-K., et al., *Degradation Mechanism of Spinel $LiAl_{0.2}Mn_{1.8}O_4$ Cathode Materials on High Temperature Cycling.* Journal of Materials Chemistry, 2001. **11**: p. 2519-2522.

106. Shin, Y. and A. Manthiram, *Microstrain and Capacity Fade in Spinel Manganese Oxides.* Electrochemical and Solid-State Letters, 2002. **5**(3): p. A55-A58.

107. Yunjian, L., et al., *Electrochemical Performance and Capacity Fading Reason of $LiMn_2O_4$/Graphite Batteries Stored at Room Temperature.* Journal of Power Sources, 2009. **189**(1): p. 721-725.

108. Doi, T., et al., *Electrochemical AFM Study of $LiMn_2O_4$ Thin Film Electrodes Exposed to Elevated Temperatures.* Journal of Power Sources, 2008. **180**(1): p. 539-545.

109. Manthiram, A. and J.B. Goodenough, *Lithium Insertion into $Fe_2(MO_4)_3$ Frameworks: Comparison of $M = W$ with $M = Mo$.* Journal of Solid State Chemistry, 1987. **71**(2): p. 349-360.

110. Manthiram, A. and J.B. Goodenough, *Lithium Insertion into $Fe_2(SO_4)_3$ Frameworks.* Journal of Power Sources, 1989. **26**(3-4): p. 403-408.

111.   Manthiram, A., et al., *Nanostructured Electrode Materials for Electrochemical Energy Storage and Conversion.* Energy & Environmental Science, 2008. **1**(6): p. 621-638.

112.   Padhi, A.K., K.S. Nanjundaswamy, and J.B. Goodenough, *Phospho-Olivines as Positive-Electrode Materials for Rechargeable Lithium Batteries* Journal of The Electrochemical Society, 1997. **144**(4): p. 1188-1194.

113.   Whittingham, M.S., et al., *Some Transition Metal (Oxy) Phosphates and Vanadium Oxides for Lithium Batteries.* Journal of Materials Chemistry, 2005. **15**: p. 3362-3379.

114.   Chung, S.-Y., J.T. Bloking, and Y.-M. Chiang, *Electronically Conductive Phospho-Olivines as Lithium Storage Electrodes.* Nature Materials, 2002. **1**: p. 123-128.

115.   Padhi, A.K., et al., *Effect of Structure on the Fe^{3+}/Fe^{2+} Redox Couple in Iron Phosphates.* Journal of The Electrochemical Society, 1997. **144**(5): p. 1609-1613.

116.   Takahashi, M., et al., *Reaction Behaviour of $LiFePO_4$ as a Cathode Material for Rechargeable Lithium Batteries.* Solid State Ionics, 2002. **148**(3-4): p. 283-289.

117.   Andersson, A.S., et al., *Thermal Stability of $LiFePO_4$ Based Cathodes.* Electrochemical and Solid-State Letters, 2000. **3**(2): p. 66-68.

118.   Martha, S.K., et al., *$LiMnPO_4$ as an Advanced Cathode Material for Rechargeable Lithium Batteries.* Journal of The Electrochemical Society, 2009. **156**(7): p. A541-A552.

119.   Yamada, A. and S.-C. Chung, *Crystal Chemistry of the Olivine-Type $LiMn_yFe_{1-y}PO_4$ and $Mn_yFe_{1-y}PO_4$ as Possible 4 V Cathode Materials for Lithium Batteries.* Journal of The Electrochemical Society, 2001. **148**(8): p. A960-A967.

120.   Yang, S., et al., *Reactivity, Stability and Electrochemical Behaviour of Lithium Iron Phosphates.* Electrochemistry Communications, 2002. **4**(3): p. 239-244.

121. Molenda, J., A. Stoklosa, and T. Bak, *Modification in the Electronic Structure of Cobalt Bronze Li$_x$CoO$_2$ and the Resulting Electrochemical Properties.* Solid State Ionics, 1989. **36**(1-2): p. 53-58.

122. Shimakawa, Y., T. Numata, and J. Tabuchi, *Verwey-Type Transition and Magnetic Properties of the LiMn$_2$O$_4$ Spinels.* Journal of Solid State Chemistry, 1997. **131**(1): p. 138-143.

123. Prosini, P.P., et al., *Determination of the Chemical Diffusion Coefficient of Lithium in LiFePO$_4$.* Solid State Ionics, 2002. **148**(1-2): p. 45-51.

124. Liu, H., H. Yang, and J. Li, *A Novel Method for Preparing LiFePO$_4$ Nanorods as a Cathode Material for Lithium-Ion Power Batteries.* Electrochimica Acta, 2010. **55**(5): p. 1626-1629.

125. Huang, Y.-H. and J.B. Goodenough, *High-Rate LiFePO$_4$ Lithium Rechargeable Battery Promoted by Electrochemically Active Polymers.* Chemistry of Materials, 2008. **20**(23): p. 7237-7241.

126. Gogotsi, Y., ed. *Nanomaterials Handbook.* 2006, Taylor & Francis.

127. Rao, C.N.R., A. Mu¨ller, and A.K. Cheetham, *Nanomaterials Chemistry.* 2007, Weinheim: WILEY-VCH.

128. Liz-Marzán, L.M. and P.V. Kamat, *Nanoscale Materials.* 2004, New York: Kluwer.

129. Hirscher, M., *Nanoscale Materials for Energy Storage.* Materials Science and Engineering B, 2004. **108**(1-2): p. 1-1.

130. Nazar, L.F., et al., *Nanostructured Materials for Energy Storage.* International Journal of Inorganic Materials, 2001. **3**(3): p. 191-200.

131. Fahlman, B.D., *Materials Chemistry.* 2nd ed. 2011, New York: Springer.

132. Jiang, C., E. Hosono, and H. Zhou, *Nanomaterials for Lithium Ion Batteries.* Nano Today, 2006. **1**(4): p. 28-33.

133. Eder, D., *Carbon Nanotube-Inorganic Hybrids.* Chemical Reviews 2010. **110**: p. 1348-1385.

134. Lin, Y., et al., *Advances Toward Bioapplications of Carbon Nanotubes.* Journal of Materials Chemistry, 2004. **14**: p. 527-541.

135. Iijima, S. and T. Ichihashi, *Single-Shell Carbon Nanotubes of 1-nm Diameter.* Nature, 1993. **363**(6430): p. 603-605.

136. Iijima, S., *Helical Microtubules of Graphitic Carbon.* Nature, 1991. **354**(6348): p. 56-58.

137. Dillon, A.C., *Carbon Nanotubes for Photoconversion and Electrical Energy Storage.* Chemical Reviews, 2010. **110**(11): p. 6856-6872.

138. http://www.basinc.com/mans/EC_epsilon/Techniques/CycVolt/cv_analysis.html, *Cyclic Voltammetry - Data Analysis*.

139. Gosser, D.K., *Cyclic Voltammetry: Simulation and Analysis of Reaction Mechanisms*. 1993, 220 East 23rd Street New York NY 10010: VCH Publishers, Inc.

140. Wang, J., *Analytical Electrochemistry*. Second ed. 2001, New York: Wiley VCH.

141. Zanello, P., *Inorganic Electrochemistry-Theory, Practice and Application*. 2003: The Royal Society of Chemistry. 615.

142. Conway, B.E., *Electrochemical Supercapacitors: Scientific Fundamentals and Technical Applications*. 1999: Kluwer Academic/Plenum Publishers.

143. Barsoukov, E. and J.R. Macdonald, *Impedance Spectroscopy: Theory, Experiment and Applications*. Second ed. 2005, Hoboken, New Jersey: John Wiley & Sons, Inc. . 595.

144. Girault, H.H., *Analytical and Physical Electrochemistry*. First Edition ed. 2004: EPFL Press.

145. Bard, A.J. and L.R. Faulkner, *Electrochemical Methods_Fundamentals and Applications*. Second ed. 2001: John Wiley & Sons, Inc.

146. Monk, P.M.S., *Fundamentals of Electroanalytical Chemistry*. Analytical Techniques in the Sciences (AnTS), ed. C.D.J. Ando. 2001, Southern Gate, Chichester, West Sussex PO19 SSQ, England: John Wiley & Sons Ltd.

147. Jin, E.M., et al., *A Study on the Electrochemical Characteristics of LiFePO$_4$ Cathode for Lithium Polymer Batteries by Hydrothermal Method.* Journal of Power Sources, 2008. **178**(2): p. 801-806.

148. Liu, H., et al., *Doping Effects of Zinc on LiFePO$_4$ Cathode Material for Lithium Ion Batteries.* Electrochemistry Communications, 2006. **8**(10): p. 1553-1557.

149. Liu, Z., X. Zhang, and L. Hong, *Preparation and Electrochemical Properties of Spherical LiFePO$_4$ and LiFe$_{0.9}$Mg$_{0.1}$PO$_4$ Cathode Materials for Lithium Rechargeable Batteries.* Journal of Applied Electrochemistry, 2009. **39**(12): p. 2433-2438.

150. Wang, G.X., et al., *A Study on LiFePO$_4$ and its Doped Derivatives as Cathode Materials for Lithium-Ion Batteries.* Journal of Power Sources, 2006. **159**(1): p. 282-286.

151. Yamada, A., S.C. Chung, and K. Hinokuma, *Optimized LiFePO$_4$ for Lithium Battery Cathodes.* Journal of The Electrochemical Society, 2001. **148**(3): p. A224-A229.

152. Li, X., et al., *A Novel Network Composite Cathode of LiFePO$_4$/Multiwalled Carbon Nanotubes with High Rate Capability for Lithium Ion Batteries.* Electrochemistry Communications, 2007. **9**(4): p. 663-666.

153. Chen, J. and M.S. Whittingham, *Hydrothermal Synthesis of Lithium Iron Phosphate.* Electrochemistry Communications, 2006. **8**(5): p. 855-858.

154. Sakamoto, J.S. and B. Dunn, *Vanadium Oxide-Carbon Nanotube Composite Electrodes for Use in Secondary Lithium Batteries.* Journal of The Electrochemical Society, 2002. **149**(1): p. A26-A30.

155. Ndungu, P., et al., *Carbon Nanomaterials Synthesized Using Liquid Petroleum Gas: Analysis toward Applications in Hydrogen Storage and Production.* International Journal of Hydrogen Energy, 2008. **33**(12): p. 3102-3106.

156. Bokare, A.D., et al., *Effect of Surface Chemistry of Fe−Ni Nanoparticles on Mechanistic Pathways of Azo Dye Degradation.* Environmental Science & Technology, 2007. **41**(21): p. 7437-7443.

157. Liu, J., et al., *Fullerene Pipes.* Science, 1998. **280**(5367): p. 1253-1256.

158. Park, M.-S., et al., *Nanostructured SnSb/Carbon Nanotube Composites Synthesized by Reductive Precipitation for Lithium-Ion Batteries.* Chemistry of Materials, 2007. **19**(10): p. 2406-2410.

159. Dong, B., et al., *Preparation and Electrochemical Characterization of Polyaniline/Multi-Walled Carbon Nanotubes Composites for Supercapacitor.* Materials Science and Engineering: B, 2007. **143**(1-3): p. 7-13.

160. Kavan, L., et al., *Multi-Walled Carbon Nanotubes Functionalised by Carboxylic Groups: Activation of TiO_2 (Anatase) and Phosphate Olivines ($LiMnPO_4$; $LiFePO_4$) for Electrochemical Li-Storage.* Journal of Power Sources, 2010. **195**(16): p. 5360-5369.

161. Franger, S., et al., *$LiFePO_4$ Synthesis Routes for Enhanced Electrochemical Performance.* Electrochemical and Solid-State Letters, 2002. **5**(10): p. A231-A233.

162. Allen, J.L., T.R. Jow, and J. Wolfenstine, *Kinetic Study of the Electrochemical $FePO_4$ to $LiFePO_4$ Phase Transition.* Chemistry of Materials, 2007. **19**(8): p. 2108-2111.

163.   Sauvage, F., et al., *Effect of Texture on the Electrochemical Properties of LiFePO₄ Thin Films.* Solid State Ionics, 2005. **176**(23-24): p. 1869-1876.

164.   Feng, Y., *The Preparation and Electrochemical Performances of LiFePO₄-Multiwalled Nanotubes Composite Cathode Materials for Lithium Ion Batteries.* Materials Chemistry and Physics, 2010. **121**(1-2): p. 302-307.

165.   Mi, C.H., X.G. Zhang, and H.L. Li, *Electrochemical Behaviours of Solid LiFePO₄ and Li₀.₉₉Nb₀.₀₁FePO₄ in Li₂SO₄ Aqueous Electrolyte.* Journal of Electroanalytical Chemistry, 2007. **602**(2): p. 245-254.

166.   Yu, D.Y.W., et al., *Study of LiFePO₄ by Cyclic Voltammetry.* Journal of The Electrochemical Society, 2007. **154**(4): p. A253-A257.

167.   Shaju, K.M., G.V.S. Rao, and B.V.R. Chowdari, *Electrochemical Kinetic Studies of Li-Ion in O₂-Structured Li₂/₃(Ni₁/₃Mn₂/₃)O₂ and Li[₍₂/₃₎₊ₓ](Ni₁/₃M₂/₃)O₂ by EIS and GITT.* Journal of The Electrochemical Society, 2003. **150**(1): p. A1-A13.

168.   Zhang, B., et al., *Structural and Electrochemical Properties of LiNi₀.₅Mn₀.₅₋ₓAlₓO₂ (x = 0, 0.02, 0.05, 0.08, and 0.1) Cathode Materials for Lithium-Ion Batteries.* Solid State Ionics, 2009. **180**(4-5): p. 398-404.

169.   Zhu, Y. and C. Wang, *Novel CV for Phase Transformation Electrodes.* The Journal of Physical Chemistry C, 2010. **115**(3): p. 823-832.

170.   Liu, Y., et al., *Effect of Carbon Nanotube on the Electrochemical Performance of C-LiFePO₄/Graphite Battery.* Journal of Power Sources, 2008. **184**(2): p. 522-526.

171.   Park, S.-M. and J.-S. Yoo, *Electrochemical Impedance Spectroscopy: for Better Electrochemical Measurements* Analytical Chemistry, 2003. **75**(21): p. 455A-461A.

172.   Greef, R., et al., *Instrumental methods in Electrochemistry - Southampton Electrochemistry Group.* 1990: Ellis Horwood.

173. Lide, D.R., ed. *CRC Handbook of Chemistry and Physics*. 90 (Internet Version) ed. 2010, CRC Press/Taylor and Francis: Boca Raton, FL.

174. He, P., et al., *Lithium-Ion Intercalation Behavior of LiFePO₄ in Aqueous and Nonaqueous Electrolyte Solutions*. Journal of The Electrochemical Society, 2008. **155**(2): p. A144-A150.

175. Sauvage, F., et al., *Pulsed Laser Deposition and Electrochemical Properties of LiFePO₄ Thin Films*. Electrochemical and Solid-State Letters, 2004. **7**(1): p. A15-A18.

176. Croce, F., et al., *A Novel Concept for the Synthesis of an Improved LiFePO₄ Lithium Battery Cathode*. Electrochemical and Solid-State Letters, 2002. **5**(3): p. A47-A50.

177. Franger, S., C. Bourbon, and F. Le Cras, *Optimized Lithium Iron Phosphate for High-Rate Electrochemical Applications*. Journal of The Electrochemical Society, 2004. **151**(7): p. A1024-A1027.

178. Murugan, A.V., et al., *Dimensionally Modulated, Single-Crystalline LiMPO₄ (M= Mn, Fe, Co, and Ni) with Nano-Thumblike Shapes for High-Power Energy Storage*. Inorganic Chemistry, 2009. **48**(3): p. 946-952.

179. Vorotyntsev, M.A. and J.P. Badiali, *Short-Range Electron-Ion Interaction Effects in Charging the Electroactive Polymer Films*. Electrochimica Acta, 1994. **39**(2): p. 289-306.

180. Conway, B.E., *Two Dimensional and Quasi Two Dimensional Isotherms for Li Intercalation and UPD Processes at Surfaces*. Electrochimica Acta, 1993. **38**(9): p. 1249.

181. Liu, H., et al., *Effects of Carbon Coatings on Nanocomposite Electrodes for Lithium Ion Batteries* Electrochemical and Solid-State Letters, 2006. **9**(12): p. A529-A533.

182.	Liu, H., et al., *Kinetic Study on LiFePO$_4$/C Nanocomposites Synthesized by Solid State Technique.* Journal of Power Sources, 2006. **159**(1): p. 717-720.

183.	Nicholson, R.S., *Theory and Application of Cyclic Voltammetry for Measurement of Electrode Reaction Kinetics.* Analytical Chemistry, 1965. **37**(11): p. 1351-1355.

184.	Lavagnini, I., R. Antiochia, and F. Magno, *An Extended Method for the Practical Evaluation of the Standard Rate Constant from Cyclic Voltammetric Data.* Electroanalysis, 2004. **16**(6): p. 505-506.

185.	Klingler, R.J. and J.K. Kochi, *Electron-Transfer Kinetics from Cyclic Voltammetry. Quantitative Description of Electrochemical Reversibility.* The Journal of Physical Chemistry, 1981. **85**(12): p. 1731-1741.

186.	Iwuoha, E.I., et al., *Electrochemical and Spectroscopic Properties of Fly Ash-Polyaniline Matrix Nanorod Composites.* Microchimica Acta, 2006. **155**(3-4): p. 453-458.

187.	Canobre, S.C., et al., *Development of composites based on lithium manganese nickel oxide and electroactive polymers.* Materials Chemistry and Physics, 2009. **114**(1): p. 350-355.

188.	Zhou, Y., et al., *A Porous LiFePO$_4$ and Carbon Nanotube Composite.* Chemical Communications, 2010. **46**(38): p. 7151-7153.

189.	Liu, H. and D. Tang, *The Low Cost Synthesis of Nanoparticles LiFePO$_4$/C Composite for Lithium Rechargeable Batteries.* Solid State Ionics, 2008. **179**(33-34): p. 1897-1901.

190.	Chang, Z.-R., et al., *Synthesis and Characterization of High-Density LiFePO$_4$/C Composites as Cathode Materials for Lithium-Ion Batteries.* Electrochimica Acta, 2009. **54**(20): p. 4595-4599.

191. Choi, D. and P.N. Kumta, *Surfactant Based Sol-Gel Approach to Nanostructured LiFePO₄ for High Rate Li-Ion Batteries.* Journal of Power Sources, 2007. **163**(2): p. 1064-1069.

192. Xie, J., et al., *Li-Ion Diffusion Kinetics in LiFePO₄ Thin Film Prepared by Radio Frequency Magnetron Sputtering.* Electrochimica Acta, 2009. **54**(20): p. 4631-4637.

193. Zhang, H., et al., *High-Rate Lithium-Ion Battery Cathodes Using Nanostructured Polyaniline/Carbon Nanotube Array Composites* Electrochemical and Solid-State Letters, 2008. **11**(12): p. A223-A225.

194. Mastragostino, M., C. Arbizzani, and F. Soavi, *Polymer-Based Supercapacitors.* Journal of Power Sources, 2001. **97-98**: p. 812-815.

195. Kim, J.H., et al., *Fabrication and Electrochemical Properties of Carbon Nanotube Film Electrodes.* Carbon, 2006. **44**(10): p. 1963-1968.

196. Tripathi, S.K., A. Kumar, and S.A. Hashmi, *Electrochemical Redox Supercapacitors Using PVdF-HFP Based Gel Electrolytes and Polypyrrole as Conducting Polymer Electrode.* Solid State Ionics, 2006. **177**(33-34): p. 2979-2985.

197. Jurewicz, K., et al., *Supercapacitors from Nanotubes/Polypyrrole Composites.* Chemical Physics Letters, 2001. **347**(1-3): p. 36-40.

198. Gupta, V. and N. Miura, *Polyaniline/Single-Wall Carbon Nanotube (PANI/SWCNT) Composites for High Performance Supercapacitors.* Electrochimica Acta, 2006. **52**(4): p. 1721-1726.

199. Chen, Q.-L., et al., *Fabrication and Electrochemical Properties of Carbon Nanotube Array Electrode for Supercapacitors.* Electrochimica Acta, 2004. **49**(24): p. 4157-4161.

200. Zhang, J., et al., *In-Situ Electrochemical Polymerization of Multi-Walled Carbon Nanotube/Polyaniline Composite Films for Electrochemical Supercapacitors.* Synthetic Metals, 2009. **159**(3-4): p. 260-266.

201. Hesani, M., et al., *The Effect of Particle Size on the Characteristics of FeCo Nanoparticles.* Solid State Communications, 2010. **150**(13-14): p. 594-597.

202. Pal, S.K. and D. Bahadur, *Shape Controlled Synthesis of Iron-Cobalt Alloy Magnetic Nanoparticles Using Soft Template Method.* Materials Letters, 2010. **64**(10): p. 1127-1129.

203. Shin, S.J., et al., *Preparation of Magnetic FeCo Nanoparticles by Coprecipitation route.* Current Applied Physics, 2007. **7**(4): p. 404-408.

204. Zeng, Q., Z. Li, and Y. Zhou, *Synthesis and Application of Carbon Nanotubes.* Journal of Natural Gas Chemistry, 2006. **15**(3): p. 235-246.
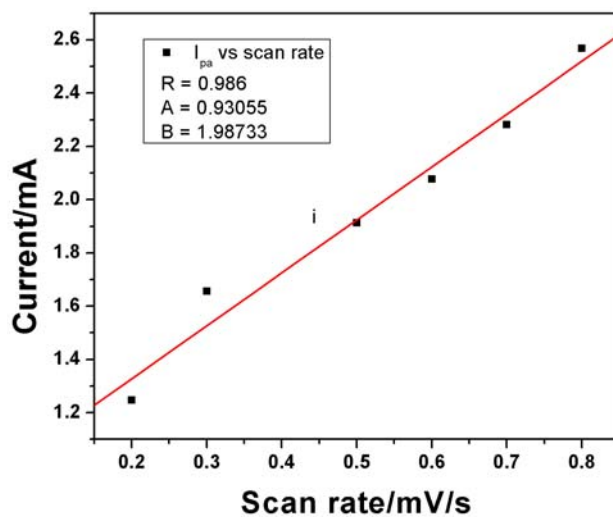
Appendix A
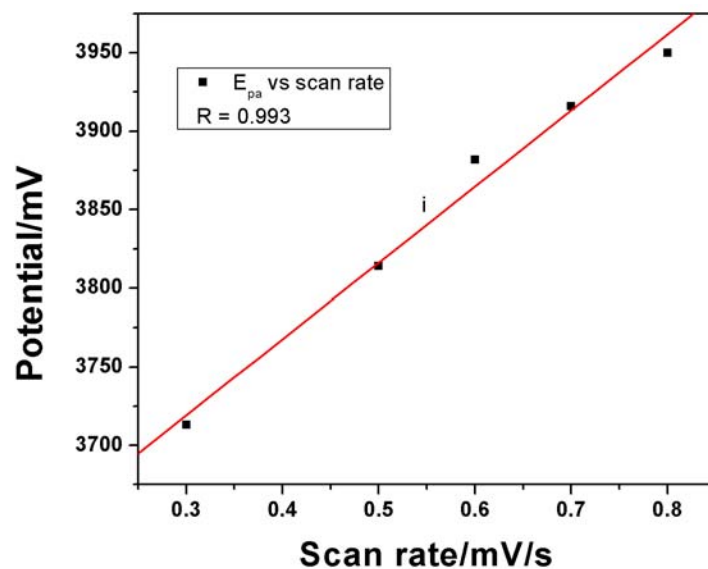
Figure A (i): The plot of the of the anodic peak potential as a function of potential scan rate for pristine LiFePO$_4$.
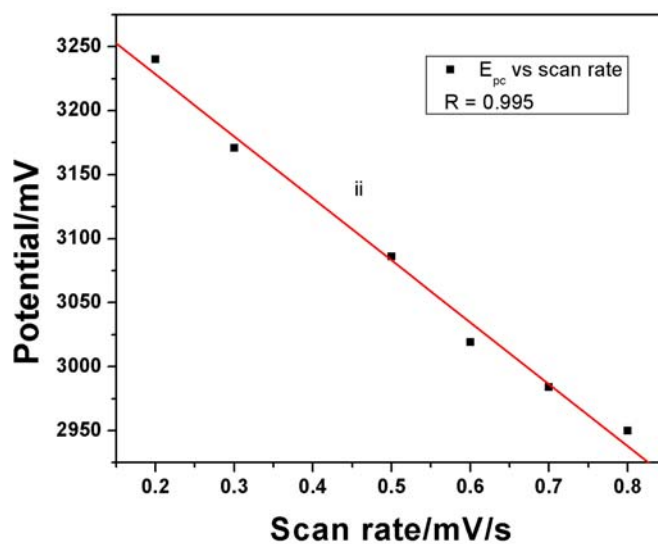
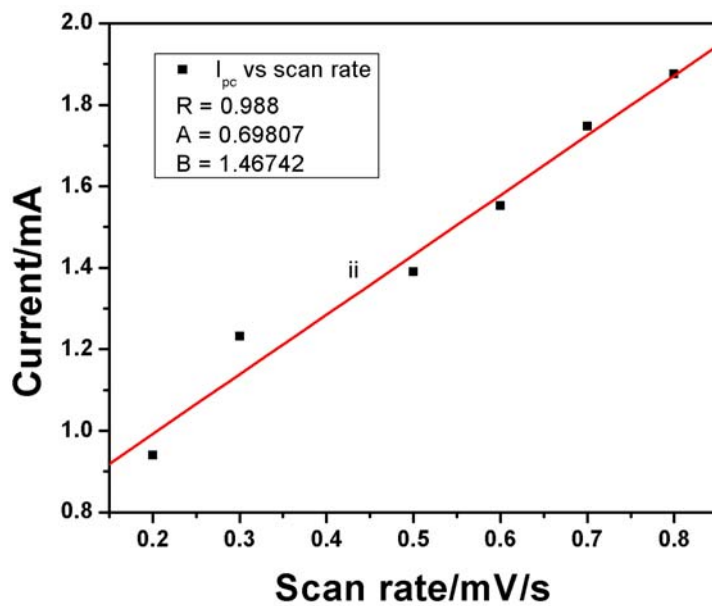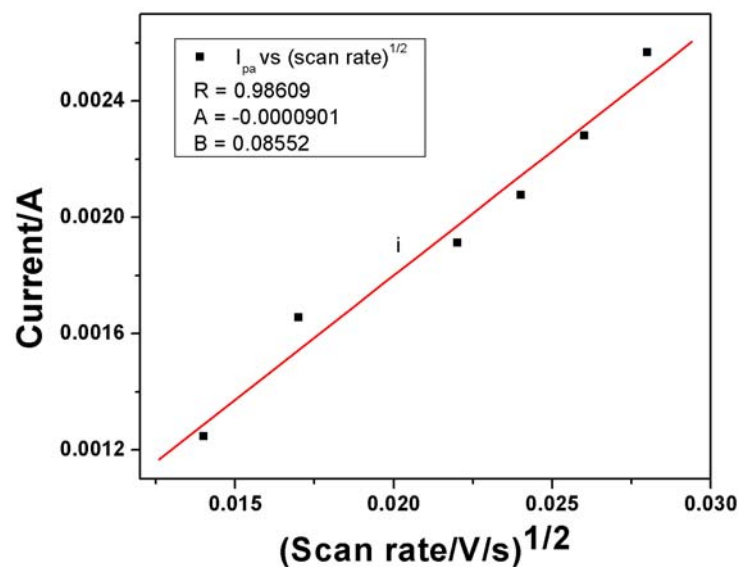**Figure A (ii):** The plot of the cathodic peak potential as a function of potential scan rate for pristine LiFePO$_4$.

Figure B (i): The plot of the anodic peak current as a function of potential scan rate for pristine $LiFePO_4$.
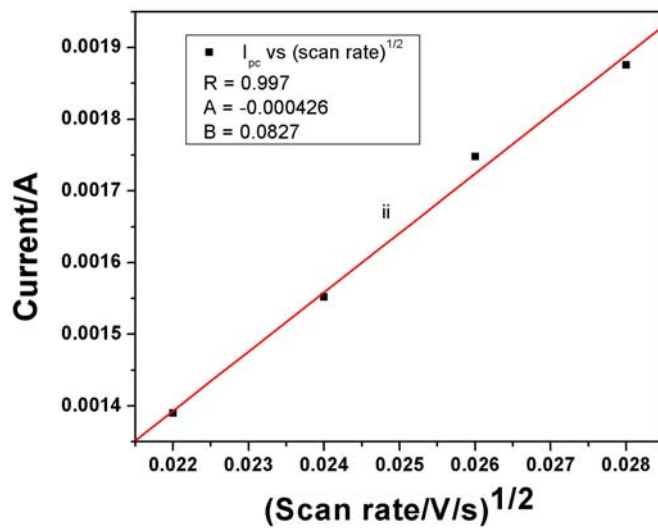

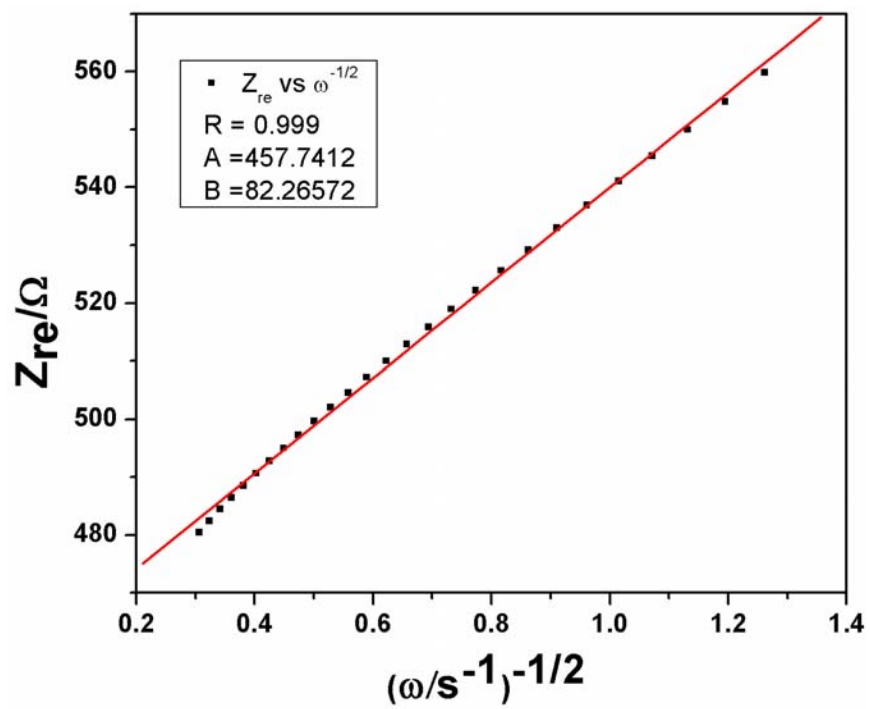**Figure B (ii):** The plot of the catodic peak current as a function of potential scan rate for pristine $LiFePO_4$.

Figure C (i): The plot of the dependence of the anodic peak current on the square root of potential scan rate for pristine $LiFePO_4$.

Figure C (ii): The plot of the dependence of the anodic peak current on the square root of potential scan rate for pristine $LiFePO_4$.

Figure D: The plot of Z_{re} vs. $\omega^{-\frac{1}{2}}$ for pristine LiFePO$_4$